Doubly-Salient Permanent Magnet Flux-Reversal-Free-Stator Switched Reluctance Machines

Nimal Savio Lobo

Dissertation submitted to the Faculty of the
Virginia Polytechnic Institue and State University
in partial fulfillment of the requirements for the degree of

Doctor of Philosophy
in
Electrical Engineering

Dr. Krishnan Ramu, Chair
Dr. Douglas Lindner
Dr. Daniel Stilwell
Dr. Tamal Bose
Dr. Carl Prather

January 21, 2011
Blacksburg, VA

Keywords: Switched reluctance motor, Doubly salient permanent magnet motor

Doubly Salient Permanent Magnet Switched Reluctance Machines

Nimal Savio Lobo

ABSTRACT

A new hybrid machine having variable reluctance and permanent magnets (PMs) is presented. The machine makes use of the features of a PM machine and variable reluctance machine. The resulting machine is doubly salient and has a structure free of flux reversals. Unlike conventional doubly salient permanent magnet machines (DSPMs), the one proposed in this report is driven by unipolar currents and uses an asymmetric converter which is used to drive switched reluctance machines. The reason to have a new hybrid machine without the drawbacks of conventional flux-reversal-free-stator SRMs and conventional DSPMs is also described.

Conventional doubly salient permanent magnet machines which are driven by alternating currents, do not use reluctance torque and have flux reversals in the stator iron. Homopolar flux at the peak flux density lowers hysteresis and eddy-current loss, since the machine‘s core operates in only one magnetizing quadrant. Due to unbalanced forces in conventional stator-flux-reversal-free machines, their deployment in industrial and end-user applications has been hindered. The presented hybrid machine has balanced radial forces. Therefore, it maintains the advantages of conventional stator-flux-reversal-free machines while shedding its disadvantages. The proposed machine has significantly increased power density and is more electromechanically efficient than its predecessor. A experimental prototype motor has been designed and built. Its static torque characteristics correlated well with predicted data. Experimental operation of the drive under open loop speed control shows the efficiency to be 90.8% under non-ideal driving conditions. In the current energy conscious environment and market, this motor because of its high efficiency has a significant role in reducing the energy consumption in household, industrial and automotive applications requiring electric motors.

Acknowledgements

First and foremost I would like to thank my supervisor and mentor, Prof. Krishnan Ramu for giving me the opportunity to pursue this career path. It was with his constant guidance and support that I was able to complete this dissertation and learn numerous motor drive technologies beyond the scope of this dissertation. He took on a chance on me for reasons I have yet to come to terms with.

I would also like to thank my committee Prof. Lindner, Prof. Stilwell, Prof. Bose and Prof. Prather for taking time to serve as members on my committee, their advice and support.

A great amount of thanks goes out to my colleagues for guiding me when I thought I was lost or losing focus. Hong Sun Lim, my dear friend and colleague, taught me how to do research in an organized fashion, and a fraction of his hard work and diligence rubbed on me. Amanda Martin Staley a senior colleague of mine also deserves a lot of thanks for teaching me the basics of switched reluctance motors and their analysis when I joined this research team. Over the years I have had the great pleasure of working on numerous research topics that did not find its way into my dissertation but I gained a great deal of knowledge in the process. Christopher Hudson, Jaehyuck Kim, Cheewoo Lee and Ethan Swint engaged me on various topics on life and graduate school. It was nice to keep those two parts of my life separate. I should also thank David Merrifield who got stuck testing my non-linear modeling for this master‘s thesis and verifying the conventional model was not applicable. He saved me a month of more of testing by doing simulations.

A lot of gratitude also go out to Dan Huff and John Lewis. They helped me with mechanical issues for the construction of the motor prototype. Their assistance saved me a month or so of trail and error in assembling the DSPM prototype. They always had last minute quick fixes for every issue I ran into. A few vendors also worked with my this-is-not-a-rush-job-i-can-pic-it-up-this-afternoon schedule. Lynn Girard of Polaris Laser Laminations for giving me lead times that were half the industry standard. Cecil Parks of Parks Electric Motor Repair deserves special thanks for winding the machine for me at no cost in a few hours instead of the standard 72 hours. I would also like to acknowledge Ansoft/Ansys Corporation for their finite element software donation which facilitated this work. Quest Technologies deserves a special thanks for donating the outrageously

expensive sound level meter which helped me and my colleagues work on various acoustic noise mitigation issues which would not have been possible hadn‘t it been for their donation.

Most of all I would like to thank my parents for giving me the initial kicks to stay in school instead of joining the so-called real world. I would also like to thank them for giving up on asking me when I will be done with school after they realized that asking me to pursue these degrees would take so long. Their endless love and very important financial support was a key factor in my success as a graduate student. With hindsight, I don‘t think they would recommend this career choice again.

Intellectual Property Disclaimer

The intellectual property in this Preliminary exam report is wholly owned by or licensed to Ramu, Inc. Machines presented in Chapter 2 of this report are licensed to Ramu, Inc. and is property of Virginia Tech Intellectual Properties (VTIP). The inventions and related work presented in Chapters 3 and 4 are wholly owned by Ramu, Inc. Work presented in Chapters 3 and 4, are protected by provisional US patent US61/318,506.

Contents

List of Tables

List of Figures

Chapter 1

Introduction

In recent years, focus on energy efficiency and production costs have driven electric machine and power converter research. Until 100% electromechanical conversion efficiency and zero-cost can be achieved, the work presented in this report will be one small step toward reaching that giant leap. Electric motors in appliances account for a majority of household energy use. Table 1.1 show percent electricity consumption for home appliance application for five different years. Appliances account for, approximately, 64% of all household energy use.

Table 1.1: Percent of Electricity Consumption by End Use [1]

Survey Year					
End Use	1987	1990	1993	1997	2001
Air-Conditioning	15.8	15.9	13.9	11.8	16
Space Heating	10.3	10.0	12.4	11.4	10.1
Water Heating	11.4	11.2	10.3	11.0	9.1
Total Appliances	62.5	63	63.4	65.9	64.7

Research into electric motors began with Michael Faraday‘s experiment in 1821, demonstrating a current carrying wire generating a circular magnetic field, The current carrying wire rotated continually around a stationary permanent magnet (PM). Ten years later Joseph Henry demonstrated the first switched reluctance motor (SRM) using a battery with a primitive commutator connected

to a wound core and stationary PMs. A year later William Sturgeon invented the commutator and with that the first shunt wound brushed dc motor. The first electric motor based on modern SRM theory was invented in 1835 and patented in 1839 by William Taylor [93]. This SRM design was used in the first electric locomotive in 1837. The electric locomotive powered by the SRM was soon forgotten due to the electric arcs created during commutation.

It wasn‘t until 1969, that the SRM was resurrected [72]. Introduction of power electronic switching devices made it possible to recover energy from the field of the motor windings during commutation. Around the 1980‘s when cost of switching devices decreased considerably and made it more feasible to explore SRMs for motor applications.

The popular dc machine which needs a dc field winding on the stator, was excited by batteries and a wound rotor armature. Armature excitation was made possible by a brush commutator connected to the same or another dc voltage source. Interaction of the field and armature, known as armature reaction generated motion. As the rotor would rotate, brushes would excite different sections of the rotor winding to generate continuous motion. The dc motor could be driven with one dc source for both armature and field, known as the series connected dc motor or separate dc sources, known as the separately excited dc motor. This simple control made dc motors extremely popular. On the other hand, induction machines‘ (IMs‘) armatures were stationary, driven by an ac voltage source and did not need a rotor with a brush to field excitation. Through the principle of induction, a time varying armature field induced a varying rotor-field. Both dc machines and IMs had the same principle of operation, albeit, one with a dc-field armature reaction and the other with ac armature reaction. With the application of the Park transformation in 1929 [73], the IM machine model could be transformed in to a dc motor model, resulting in a unified control theory for both motors.

With transistors becoming cost effective, dc motors with just one transistor and diode, achieved variable speed operation, further increasing its popularity. An IM required four times as many devices in a single phase machine to vary armature frequency. When safety, maintenance and life-span of machines became more critical in lowering operating costs of machines, IMs with an inverter started replacing dc motors which needed regular brush replacement and had safety concerns from arc discharges during commutation. As large scale manufacturing of PMs became worthwhile, the field winding of a dc motor was aided by a PM or replaced by it. Replacing field windings led to a

constant field without the need for separate voltage excitation sources for the armature and field. The stator i.e. field source, with a PM and windings connected to a chopper delivered variable speed operation with high efficiency.

Similarly, field windings of IMs were replaced by PMs embedded on or in the rotor, which when rotated, created a rotating magnetic field. This new ac motor was felicitously named, the PM brush-less dc motor (PMBDCM). The name heightened its popularity, by likening it to a brushed dc motor, without needing brushes to generate an armature like field, even though the PMBDCM was not a dc motor without brushes, instead was an ac brush-less motor. As PM field strength and robustness increased, power density and popularity of PM ac machines increased. PMBDCM and PM ac machines require a power converter for operation.

With a recent push for higher efficiency standards in all applications, variable speed machines are gaining increased traction in the market place, after being studied for decades. Universal motors are installed in most low cost home appliances and hand tools. The universal motor is a type series connected dc motor which is capable of being driven by a dc or ac voltage source.

Recent research on power converters for ac machines has focused on increasing the power density and operating range of variable speed machines. To decrease total system cost, increasing power density of the brush-less ac machines is significant. Elimination of position sensors also allowed for increased system reliability, since position feedback signals are corruptible by EMI or hazardous operating conditions like extreme heat and vibration[92, 29, 22, 83, 14, 26] . Yet, all ac machines are tethered to their ubiquitous power converter, the H-bridge inverter. Power converter cost and expensive PMs in ac machines still makes the universal motor a winning choice for low cost applications.

On the other hand, SRMs were largely overlooked earlier, due to lower power density and large acoustic noise [8]. Recent advances in machine design for SRMs led to power densities and efficiencies which equaled conventional ac machines, reigniting interest in this machine topology [37, 67, 54, 95, 17, 46, 41, 42, 86, 53, 52]. SRMs are comprised of a steel core for both stator and rotor, with copper windings present only on the stator. Lack of windings and/or PMs on the rotor make it the lowest cost motor in terms of manufacturing. The magnetic structure of the SRM is very different from conventional ac and brushed motors. AC machines have stators composed of steel with either sinusoidally wound copper windings for sinusoidal back-emf PM synchronous

machines or concentrated wound machines with non-sinusoidal back-emf, classified as PM brushless dc machines. AC machines have very small or negligible saliency as compared to SRMs which have very high saliency due to its doubly salient structure. Structural saliency in the air gap leads to spatial variation in the permeance of the machine.

Phases in a SRM are largely magnetically isolated from each other and phases in an ac machines are magnetically coupled to each other. Magnetically isolated phases leads to higher fault tolerance for the SRM when compared to ac machines. Without the need for a special power converter, a failure in one machine phase would isolate itself naturally. In an ac machine a fault in one phase winding would affect healthy phases. Albeit the faulty phase can be disabled, proper control of the remaining healthy phases is not possible without employing more expensive power converters [97].

With the aforementioned SRM advantages, adoption of SRMs in commercial applications has still been slow. SRMs have been proposed and successfully implemented in a variety of applications ranging from household appliances, lower power levels, to industrial or high power applications [85, 9, 10, 16, 15, 64, 80, 100, 35, 13]. Furthermore, a plethora of power converters have been developed for SRMs depending on the degree of control required [5, 70, 77, 43, 44, 36, 18, 32, 31, 33], including a power converter with the smallest number of switching devices capable of four quadrant operation [45]. The four quadrants of machine operation are motoring and generating while rotating in both circumferential directions. Power converters can be matched to demands of the application. For high performance systems, a converter which offers more degrees of freedom could be used. In low cost systems where the SRM is not operating continuously for long periods of time and efficiency is not critical, like home appliances, a low cost converter with fewer degrees of freedom and smaller number of transistors could be employed. This gives SRMs a bigger advantage over ac machines which require the inverter.

Electromagnetic torque is SRM machines is a consequence of varying reluctance in the magnetic path of flux w.r.t to rotor position. PM machines are designed to minimize cogging torque, which is caused by reluctance variation. In classical ac machines, the torque production is due to the interaction of the rotating field of the rotor, with that of the armature and this torque production mechanism is called armature reaction. Cogging torque is reduced by choosing a non-integer stator slot to rotor pole ratio, having an odd number of slots to decrease cogging torque frequency, varying the stator slot‘s physical geometry, to mention a few [39]. When the ratio between slots and poles is

an integer, cogging torque is magnified. A common method used to reduce reluctance variation and cogging, is skewing, where the rotor is not symmetric axially. For skewing, a 'twist' is introduced while stacking rotor laminations depending on the stator slot configuration.

1.1 Doubly Salient PM Machines (DSPMs)

1.1.1 DSPMS categorized as ac machines

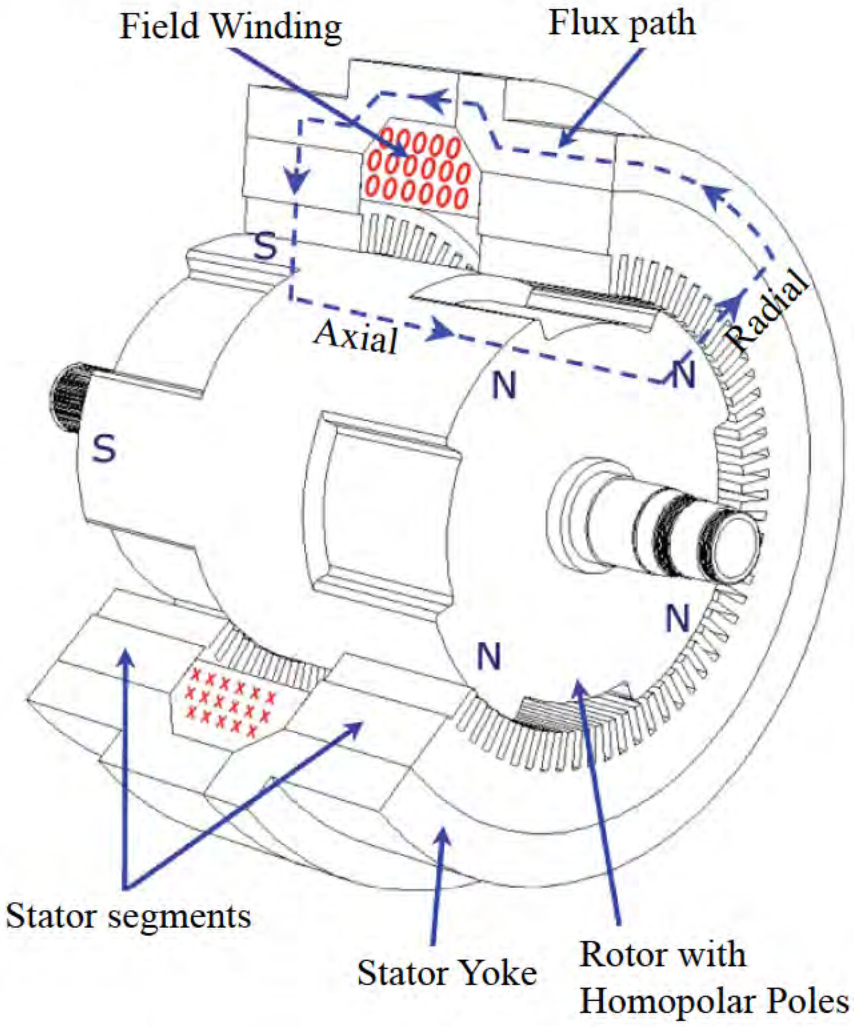

Figure 1.1: Homopolar inductor machine. Stator windings not shown for clarity. (Original figure [20])

The homopolar inductor alternator (HIA) is a type of synchronous motor where field and ar-

mature windings are located on the stator [96]. Fig. 1.1 shows the structure of a HIA motor. The rotor is made of iron and has no windings or PMs. A field coil is circumferentially wound through the stator back-iron. The rotor of a HIA is not symmetric axially. Instead, the salient rotor poles are offset by half a rotor pole pitch, half way through the stack [20]. The field winding flux loop flows axially through the stator yoke and radially inward through rotor poles on one side of the HIA stack, axially through the rotor yoke to the second half of the stack and radially back into the stator through the rotor poles. Rotor poles on each axial half of the rotor have the same polarity i.e. flux entering or leavening them. Almost all machines, popular in research either, are either radial flux machines or axial flux machines. The HIA is a combination of both. The largely forgotten HIA, which laid the ground work for all modern doubly salient doubly excited machines, were popular in automotive applications where they are still popular as alternators. Due to their complex 3D magnetic structure, analyzing these machines was not easy and led to its demise until recent years where they have been proposed in very high power megawatt level, naval [20] and generator applications [87].

One of the earliest attempts in using PMs in a variable reluctance machine is the flux switch machine [82]. Two magnets embedded in the stator are used to generate varying flux as the rotor rotates, inducing varying flux linkage in the stator windings.

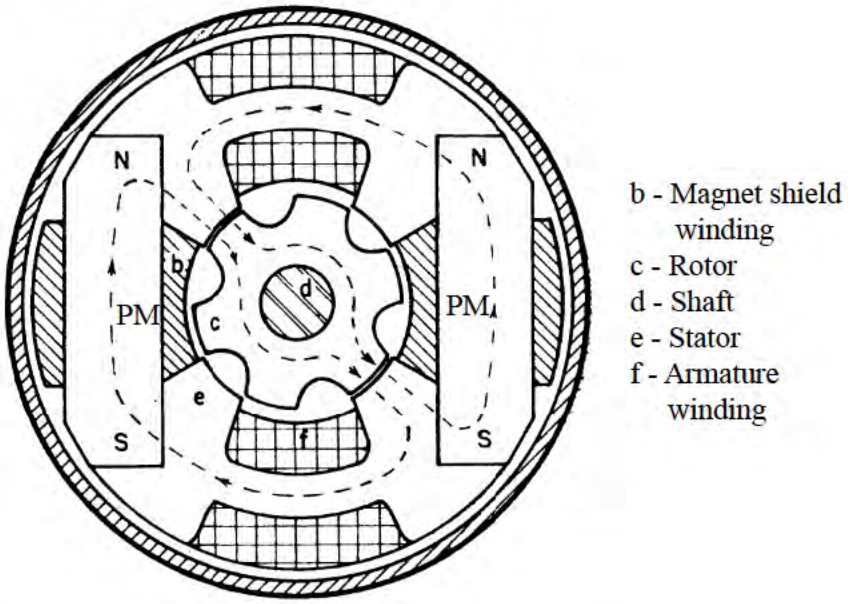

Figure 1.2: Flux-switch motor with four stator poles and six rotor poles [82].

The PMs required shorted windings around their magnetization axis in order to prevent demagnetization caused by the flux generated by winding excitation. Fig. 1.2 shows the cross section view of a flux switch motor. As the rotor rotates, the flux paths switch to the stator poles having the least reluctance in the air gap. The rotor of this machine has salient poles like poles RM rotors. The flux switching principle caused the rate of flux linkage to double as compared to the homopolar inductor alternator [82]. The flux switching machine was claimed to have a higher power density than the HIA which was less efficient.

A new motor based on the flux switch principle and replaced the PM with a field winding was also developed [76]. Fig. 1.3 shows the layout of a two phase flux switching motor without PMS. The armature winding of this motor is full pitched.

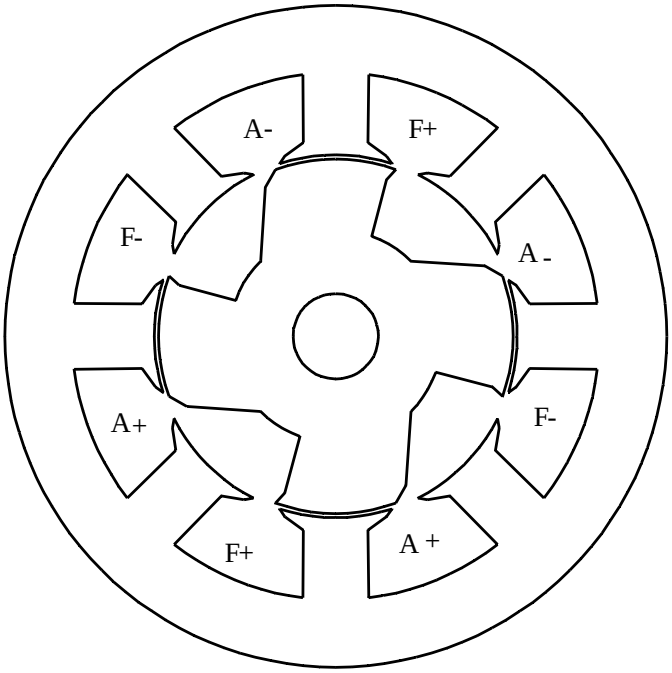

Figure 1.3: Two-phase flux switching motor without PMs. F - Field winding. A - Armature winding.

This flux switching motor is operated like a series connected dc motor. The full pitched armature winding is comprised of a bifilar winding, so the motor could be driven with a unipolar converter. Each of the armature windings in the bifilar pack are excited separately with a chopper like converter to achieve bipolar-flux switching. During commutation of one armature winding in the bifilar pack, energy is transferred to its counterpart. This flux switching configuration was proposed for low

cost home appliances and tools [78], an automotive applications [75], but hasn't gained popularity. Full pitch windings, instead of PMs for field excitation, raise the cost of the machine and increased copper loss compared to short pitch windings.

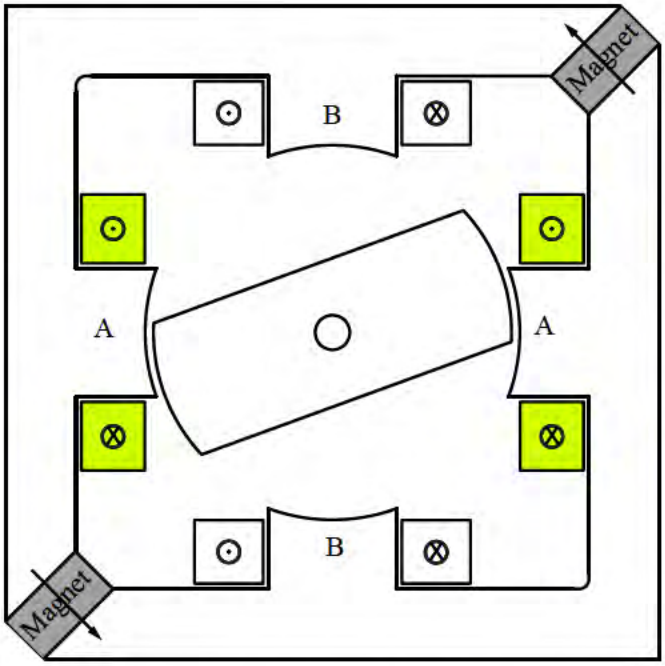

Figure 1.4: Two-phase DSPM with PMs in the back-iron.

An improved flux switching motor with PMs embedded in the stator back-iron provided the same benefits as the original flux switch machine with even higher power density and efficiency [55]. This doubly salient PM machine (DSPM) did not require any shorted windings to prevent demagnetization of the PMs. A two phase DSPM with PMs in the stator yoke is shown in Fig. 1.4. A unipolar current converter or bipolar converter can be used to drive this DSPM, but most applications of this type of DSPM use a bipolar current converter. This type of DSPM was theorized to have between $\sqrt{2}$ to $2\sqrt{2}$ times the power density of an SRM, depending on whether it was driven with unipolar or bipolar current converter, respectively. A high reluctance path in the rotor back-iron caused by the PM, forces flux generated by the phase windings to take a leakage path through adjacent stator poles where reluctance is minimum. The leakage path reduces the flux generated by the phase windings and may cause cancellation of winding MMF if the phases are excited simultaneously, depending on the polarity of windings around the stator poles. Achieving a power density increase of $2\sqrt{2}$ is highly unlikely, with a bipolar current converter since the net

reluctance torque in one ac cycle is zero. Reluctance torque being proportional to the square of the winding current means the reluctance torque contribution would make the machine behave as a motor while the current is positive and act as a generator while the current was reversed. Hence torque in the positive current cycle and negative current cycle would not be identical.

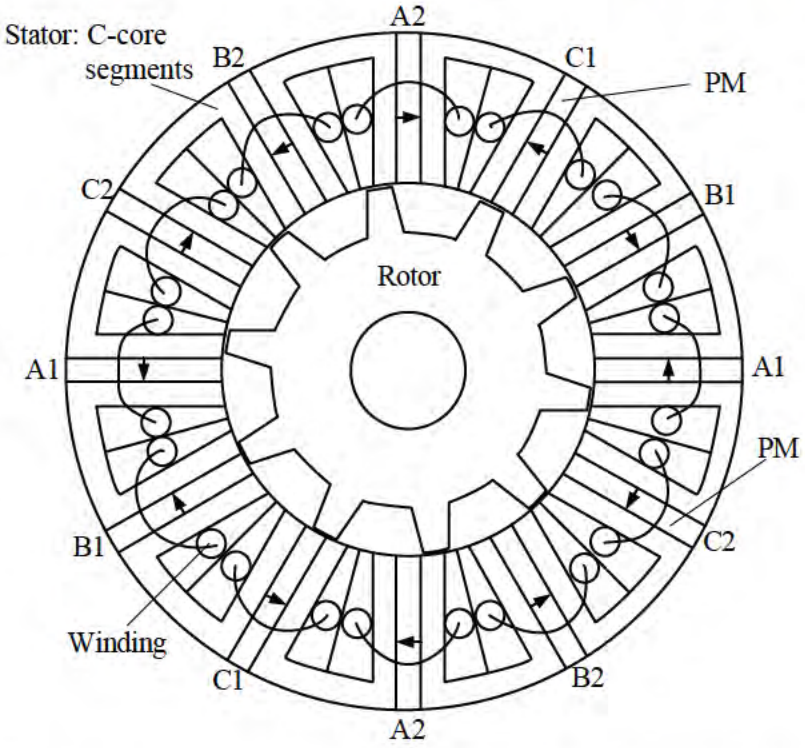

Figure 1.5: Three-phase flux switching machine with circumferentially charged flux-focusing PMs.

DSPMs based on bipolar PM flux have also been developed [21, 23]. The stator poles of a SRM are split and PMs which were excited circumferentially are inserted in the middle of the stator poles. Concentrated winding around salient stator poles are also present in this class of flux switching DSPMs. The circumferentially magnetized permanent magnets focus flux in the air gap and stator poles which results in higher flux density in the air gap and higher torque density [101]. The PMs could also be inserted by splitting an entire SRM stator radially along the center of the stator poles to insert a full magnet which spans from the inner diameter of the stator poles to the outer diameter of the stator body. In this case, the stator would be composed of segmental C-core units. Fig. 1.5 shows a three-phase C-core-with-PMs type flux switching motor. Due to complex construction of segmental DSPMs, this type motor has been limited to the spectrum of research

and applications without strict cost constraints. Comparisons between DSPMs with magnets in the stator yoke and flux switching machines, showed a significant power density advantage of the latter machine due to flux focusing PMs. [23]

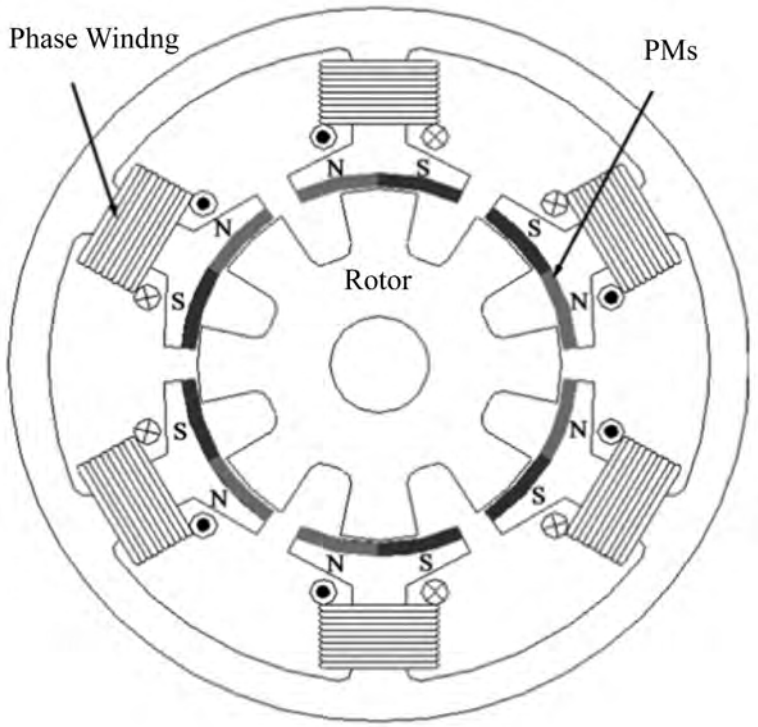

Figure 1.6: Three phase flux reversal motor.

Another class of DSPMs which incorporated PMs on the stator pole surface of an SRM is known as the flux reversal SRM citefrm.1,frm.2,frm.3. The flux reversal machine has the structure of a SRM with two PMs attached to each stator pole. A three-phase flux reversal machine is shown in Fig. 1.6. The two PMs per stator pole pole have opposite polarity. The polarity of PMs on diametrically opposite stator poles is the same which means PM polarities are anti-symmetric diametrically. Depending on rotor position only one of the two PMs on the stator pole contributes to torque production. No torque is generated when a rotor pole faces the joint between the two magnets or is equidistant between magnets of adjacent stator poles. Since the PMs are on stator pole faces, machine manufacturing is easier due to a monolithic iron core for the stator.

Doubly salient PM machines need varying reluctance to generate a varying flux linkage. Due to symmetry of the stator and rotor, placement of PMs can introduce cogging torque in these

machines. For variable reluctance machines with phases less than three and symmetric rotor pole faces, there exists a dead-zone where no torque can be produced by any phase since the derivative of reluctance at these rotor positions are essentially zero. These positions are called fully aligned potion, where a rotor is fully aligned to a set of stator poles and fully unaligned position, where poles are equidistant from a set of stator poles. To facilitate self-staring in a variable reluctance machine with less than three phases, it is normal to incorporate asymmetry on the rotor pole face. Asymmetry of the rotor pole means the external rotor pole surface is not symmetric on either side of the rotor pole center line. By introducing asymmetry to the rotor pole face, derivative of reluctance at every rotor is non-zero. In variable reluctance machines with greater than three phases, phase shift in the magnetic characteristics is less than 180^o and torque can be generated any rotor position with introducing asymmetry to the rotor pole face.

1.1.2 DSPMs of the reluctance type

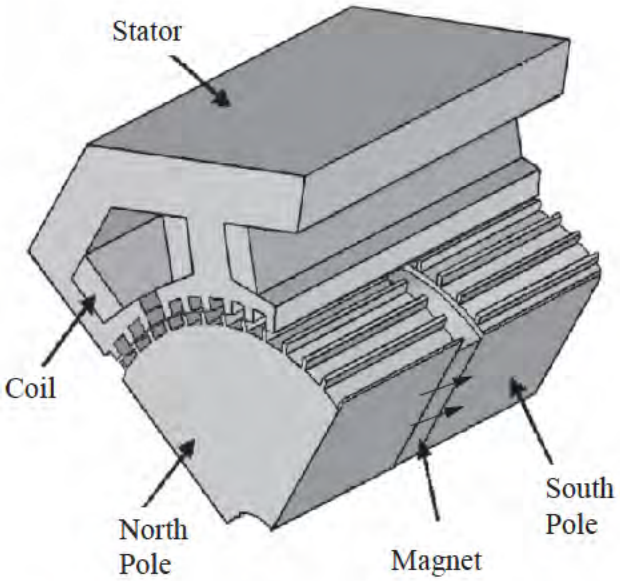

Figure 1.7: Hybrid stepper motor. (Original figure [28])

Thus far the doubly salient doubly excited permanent magnet machines that have been described are mainly operated with bipolar currents, and zero net reluctance torque. Majority of torque contribution is from armature reaction, and DSPMs are largely categorized as ac machines in research publications. Probably the first attempt at creating a DSPM where reluctance torque was

capitalized on, was the hybrid stepping motor (HSM) [88]. Fig. 1.7 shows the cross-section of a HSM. The HSM is designed for low speed applications that required very high torque density. The stator of an HSM is a like a stepper motor stator and the rotor is similar to a HIA rotor. One set of rotor poles on a half of the stack are north and rotor poles on the second half of the rotor stack are south. Field excitation is provided by a PM sandwiched in the middle of the rotor stack. The PM is magnetized in the axial direction and 'boosts' stator MMF making it a reluctance torque motor. Due to narrow stator and rotor pole widths, poles experience extremely high saturation [28]. The flux loop shape in HSMs is the same as HIAs. Creating an accurate magnetic circuit for this machine proved to be hard historically like the HIA and efficient design of HSMs became cumbersome. This motor was largely forgotten like HIAs until finite element analysis applications and computing power were powerful enough to perform 3D analysis.

Vernier reluctance magnet machines and Vernier hybrid machines are also DSPM machines which have rotor poles and stator poles like as stepper motor [89, 71]. They are different in design than the stepper motor in the way their poles are shared to create the vernier effect [51, 27, 84]. Fig. 1.8 shows one Vernier hybrid machine where the rotor poles are replaced by PMs of alternating polarity.

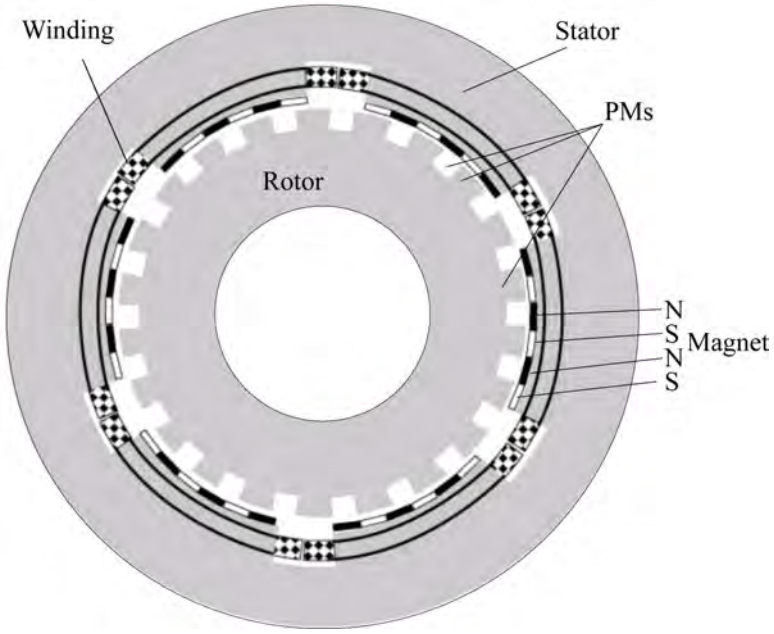

Figure 1.8: Three-phase Vernier hybrid machines. (Original figure [27])

The gearing effect of having a large number of rotor and stator poles, give DSPM of the reluctance

type very high torque density.

1.2 Evolution of variable reluctance machine topologies

So far the review has covered doubly salient doubly excited machines where both excitation sources could be from windings or one of the two is a PM. The machine proposed in this report, is one that is a DSPM of the reluctance type. So accordingly, it is appropriate to review variable reluctance machines. There are three types of reluctance machines, switched and synchronous and stepping/vernier. Stepper motors are ideal for low speed/high torque applications like servos and are not in the scope of this dissertation.

1.2.1 Synchronous reluctance machines

Synchronous reluctance machines (SyRM) did not receive much attention until the 1980's. Lack of understanding the effect of saliency and maximizing it to generate reluctance torque was a large reason. Some early work on SyRMs showed promising results for this type machine [34, 47, 12]. Modeling and control of SyRMs is similar to PM brush-less machines [6, 99], making this an ac machine. SyRMs have stators that are identical to an IM or PM brush-less machine. The review of synchronous reluctance machines in this section is a recapitulation of the discussion in [90]. Rotors of SyRMs have three main geometric configurations.

One configuration has salient poles. The saliency ratio, ratio of maximum inductance to minimum inductance as the rotor rotates, is low with this type of rotor. Another rotor design in the same category is one that is similar to a salient pole wound rotor synchronous machine, with the windings removed. Fig. 1.9(a) shows this type of salient pole rotor.

The second class of SyRM rotors are the single flux barrier design. The non-salient-pole rotor slots are known as flux barriers, which direct flux flow through the rotor. The first rotor is essentially the rotor of an interior PM machine with the PMs removed. The second rotor combines the slots of a caged induction motor's rotor without cage and the interior PM rotor slots. The slots in the rotor can extend to the rotor surface to increase saliency, in which case the rotor becomes segmental and assembly raises cost.

The third class of rotors have multiple flux barriers or guides [47]. As the number of flux

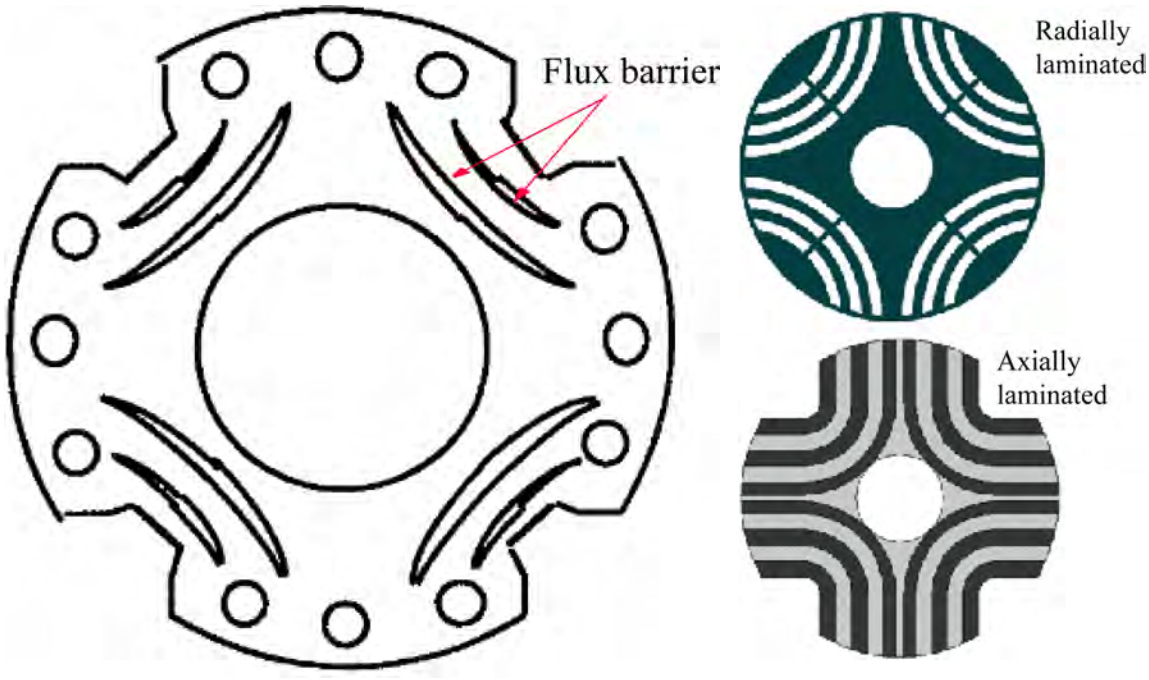

(a) (b)

Figure 1.9: Synchronous reluctance motor rotors. (a) Salient pole cage-less rotor with flux barrier/guide slots (b) Non-salient pole multiple flux barrier rotor. .

barriers increase, the saliency ratio of the machine increases, up to a certain point. The rotor can be constructed in two ways, transverse lamination stacks or axial stacks. Fig. 1.9(b) shows the two type of rotor constructions. For transverse stacks laminations are punched out with flux barrier slots and then stacked. In axial stacks, axially aligned rotor laminations are bent strategically to form the flux guide. Axially laminated flux guides produce the highest saliency ratio of all synchronous reluctance rotors. The number of flux barriers in the rotor is usually around 10 to obtain the highest saliency ratio. The author would like to point out, that, stacking transverse laminations is standard and straightforward, since the majority of motors of all types are stacked axially. Bending laminations axially and stacking them in a radial fashion increases the cost of production for this type of rotor and isn‘t suitable for large volume low cost applications.

Only multiple flux barrier/guide rotors are researched due to high saliency,. The other two rotor configurations do not a have a high enough power density to be make SyRMs a viable replacement for existing IMs. PMs can also be inserted into the center of a flux barrier slot to increase the power density of the machine. SyRMs with small PMs inserted into the flux barriers are known as

PM assisted SyRMs [7].

1.2.2 Switched reluctance machines

Once the SRM resurfaced, in the 1970s, it entered a research field dominated by ac machines and dc motors. It wasn‘t until 1970, when a seminal paper [48], established fundamental design and control theory of SRMs. The switched type variable reluctance machine gained popularity fast due to its very low cost and robust structure of all machines. This singly excited machine requires a power converter to function. Simplicity of control gives it an advantage over ac machines. SRMs are highly nonlinear in their magnetic characteristics when compared to ac machines where saliency does not vary until the stator iron is saturated. As design procedures for SRMs were refined through many years of research, so did their power density [40, 69, 81, 68]. As strategies to control or mitigate acoustics noise in SRMs were proposed, their popular grew even more, since acoustic noise was one of the main factors that forestalled its development [11, 2, 3, 98]. In addition, many new motor structures were proposed to increase the power density and performance of the SRM [74, 86, 53, 52, 94, 38]. A class of SRMs, known as flux-reversal-free-stator (FRFS) SRMs relevant to this dissertation are reviewed.

The first FRFS developed was the 6/3 SRM with six stator poles and three rotor poles. The SRM operated with unipolar flux throughout its stator at all times. Unipolar flux, leads to lower core-loss in the iron and high MMF. Also, in SRMs with more than one phase, where multiple phase windings are excited simultaneously to maximize torque generation, some portions of the SRM core will have opposing MMF in their magnetic circuits. With only unipolar flux, exciting multiple phases at the same time always causes additive flux and higher flux density in the air gap - more torque. The drawback of the original FRFS SRM is unbalanced radial forces whose discovery is presented in Chapter 2. SRMs usually have balanced radial forces due to symmetry of the stator and rotor poles.

A new segmented two-phase FRFS SRM with E-core stators having balanced radial forces was developed to replace the unattractive 6/3 SRM [53]. Fig. 1.10 shows the stator of the E-core SRM with half of the rotor. The rotor and stator are comprised of ten and three salient poles, respectively. One stator poles is shared by both phases, hence ‘common pole‘ in the machine‘s name. The shared pole has no copper windings around it. The air gap surrounding the shared pole

does not exhibit variable reluctance and serves as a return path for flux from a phase.

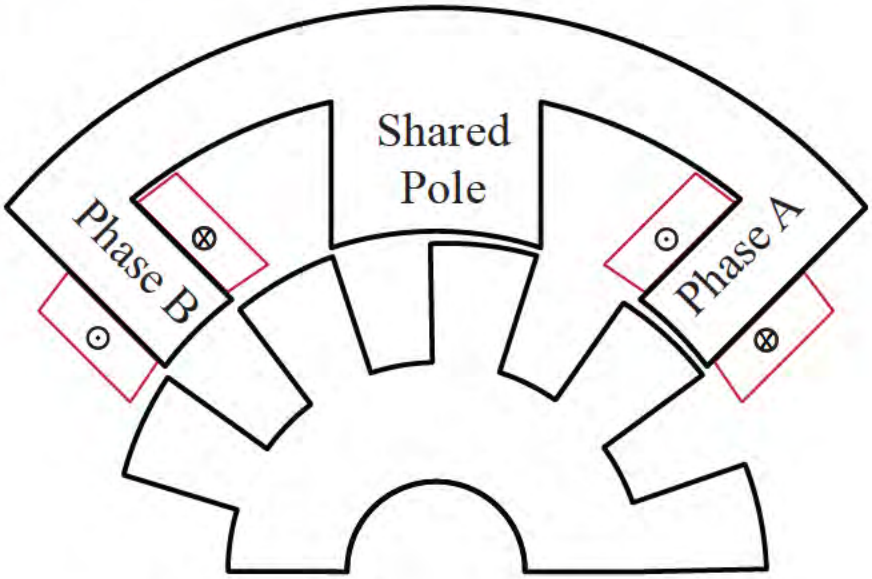

Figure 1.10: E-core SRM with shared pole (half machine).

The e-core srm requires at least one stator segment block to function. More stator segments can be placed strategically around the rotor to increase output torque. The only drawback of having one stator segment is unbalanced radial forces on the rotor which would result in this SRM suffering from the same unbalanced normal forces acting on the stator/rotor of conventional FRFS SRMs. Therefore, at least two equidistant stator segments are required for balanced normal forces. Concurrently, the 6/3 SRM was modified by doubling the number of rotor poles and stator poles, 12/6 SRM, effectively creating a machine composed of two FRFS SRMs which are diametrically opposite to cancel unbalanced forces [91]. The 12/6 SRM is also a FRFS SRM.

The e-core SRM with segmental stator is not ideal for real world deployment due to low tolerance assembly of stator segments. Air gaps in fractional and low horsepower SRMs are normally less than 1 mm [37]. Misalignments of any one stator core would create unbalanced normal and circumferential forces. Therefore, the 4ecore SRM which is a monolithic structure comprised of four e-cores was developed for increased manufacturability and higher power density [52]. Its principle of operation is the same as the original E-core SRM.

The concept of FRFS SRMs was limited to two phases until a new method to develop an SRM any number of phases having FRFS was discovered [62]. The new class of multiphase FRFS

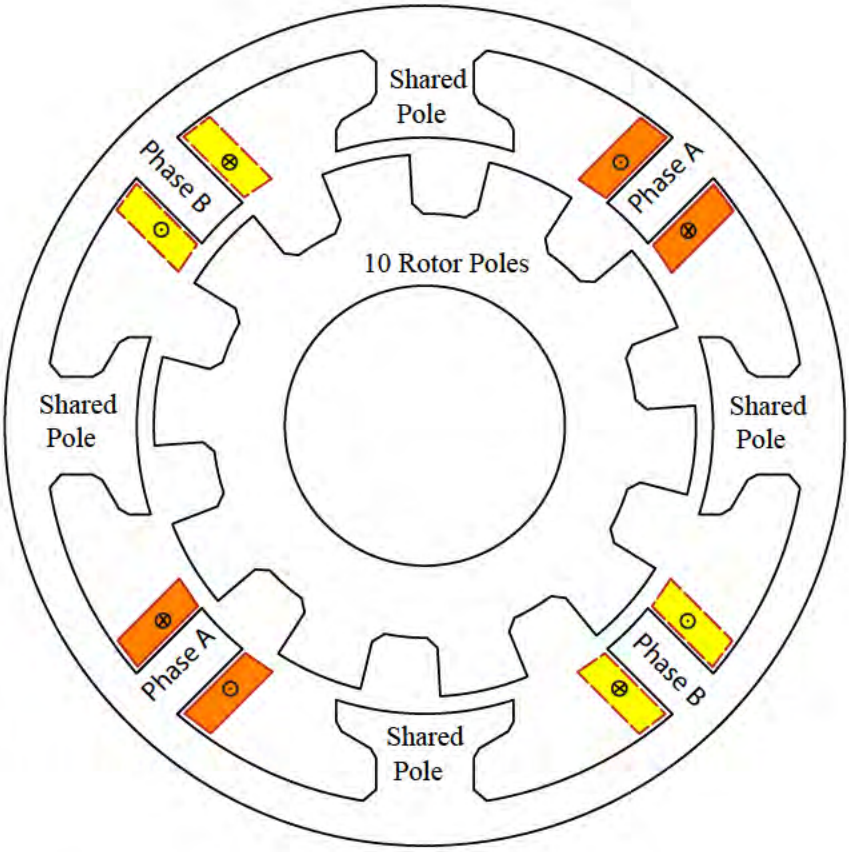

Figure 1.11: Monolithic 4-ecore SRM with shared pole.

SRMS could further be modified for any number of phases and stator segment combination. These multiphase SRMs also presented an excitation strategy to remove flux reversals from the rotor back iron leaving only the rotor poles to experience flux reversals during operation.

1.3 Contributions in this dissertation

PM brushless ac and dc machines have gained considerable interest in variable speed high volume applications over the last 10 years. High volume production of PM machines for cost prohibitive applications like home appliances and automotive applications have become feasible only in the last decade. SRMs have only received a fraction of the limelight. In the last two years, due to geographical and political reasons, the prices of rare-earth PMs have increased fourfold and are continuing to rise. Rare-earth neodymium PMs have high energy density, and facilitate an

efficiency and power density gain that lower energy density magnets like ceramic or samarium do not offer. The worlds largest rare-earth PM material supplier, China, is set to cut global output by more than 35% ([4]) as demand is set to increase [30]. This trend has shed new light on SRMs which do not require permanent magnets.

In this dissertation two novel classes of two phase flux-reversal-free-stator SRMs are presented. Their design, modeling and analysis are conducted with analytical equations, finite element simulations and physical experiments. The motivation to have flux-reversal-free iron segments in any electric machine is to reduce core-losses and as a result increase efficiency. This study and its contributions are focused on the following,

1. The first class of novel two phase flux reversal free SRMs has stator six stator poles and three, nine, fifteen or higher number of appropriately selected rotor poles.

   This novel class of machines, through a intelligent combination of stator poles, winding configuration and rotor poles, prevents any flux from reversing polarity in the stator iron. Conventional SRMs have bipolar flux in the stator and rotor iron. The eddy and hysteresis losses are reduced when flux in the stator core is unipolar. Flux reversals in the rotor are still present.

   a. Two configurations of this novel SRM are presented and analyzed in detail.

   b. Detailed machine design and analysis are derived for this class of SRMs. Design equations aid in the rapid initial design and sizing of the SRM for any power level and operating speed.

   c. Since uncomfortable acoustic noise is one of the factors that has drawn attention away from SRMs, radial forces in the machine are analyzed analytically and through dynamic finite element simulations. The existence of unbalanced net radial force during operation is discovered in this class of machines.

   d. The reduction in core-losses due to the absence of flux reversals are also calculated analytically through Steimetz equations for core-loss and through finite element simulations.

   e. The design of one of the two novel machines analyzed is verified through physical experiments. Inductance is measured for various positions and three phase currents to validate the novel machines predictions.

2. The second novel class of flux-reversal-free-stator SRMs is a PM assisted SRM. This novel SRM is derived from the existing 4ecore SRM. The novelty of the shared pole in the 4ecore SRM presents an opportunity to increase power density of the SRM by incorporating PMs into the machine. A new type of doubly salient PM SRM is derived from the 4ecore SRM. The novel machine does not have two permanent magnets on every stator pole, isn't segmented to insert magnets in the stator yoke and has no permanent magnets attached to the rotor pole face.

    a. A small PM is attached to the shared poles by increasing the diameter of the shared pole or shaving off material to allow for a magnet to be installed, while maintaining the air gap between the stator and rotor. The size of the magnet is chosen to be small in order to generate continuous positive torque as the 4ecore SRM. The magnet provides additional flux to magnetize the air gap under the torque generating poles without needing additional excitation from the drive electronics. Thus the RMS current needed to drive the motor and the winding size can be reduced.

    b. Analytical modeling of the novel machine is derived from fundamental equations and is presented in Chapter 3. The novel modeling technique incorporates cogging torque which has been neglected in literature. This is the first PM brushless machine with homopolar flux.

    c. A design procedure for rapid design of the SRM is derived in Chapter 3. The design procedure provides physical sizing dimensions, winding design and magnet selection for an SRM with a desired power level and sizing restrictions.

    d. From simulations performed, the new PMSRM has 37% higher power density than the 4ecore SRM and 6% higher efficiency. The additional costs of the magnets are offset by the power density and efficiency gains. The size of the magnets installed in the novel machine is a third of the size of magnets which are conventionally installed in PM ac or dc machines.

    e. A prototype of the designed novel PMSRM is tested extensively to verify the high power density and efficiency. Reluctance torque and magnet torque are measured and correlated with predicted torque. Back-emf was also measured and has an acceptable range of error given the manufacturing tolerances for the magnets. The prototype was operated as a

torque drive and efficiency was measured at various operating points. The converter used to run the prototype was not able to operate both phases symmetrically and under non-ideal operating conditions showed a peak motor efficiency or 90.8%.

Chapter 2

Conventional Flux-Reversal-Free-Stator Switched Reluctance Machine

In this chapter, two configurations of a two-phase FRFS SRM are contrasted. The presence of unbalanced radial forces in the conventional flux-reversal-free stator SRMs and core losses are estimated. The chosen configurations are two from a variety of possible configurations of two-phase flux-reversal-free-stator SRMs having six stator poles and rotor poles in odd multiples of three. The two configurations presented in this chapter will have three and nine rotor poles. One phase of the SRM is comprised of three stator poles separated spatially by 120^o. One pole in a phase carries the entire flux in the magnetic circuit while the remaining two poles carry half the amount of flux and serve as its return path. Therefore, only two-thirds of the stator yoke carries flux when a phase is excited and consequently, core losses are reduced. No flux reversal occurs in the stator even when both phases are simultaneously excited. Due to the unique structure of FRFS SRM, forces in the air gap are distributed across three stator poles. This unique feature along with no flux-reversal in the stator mitigates radial forces and acoustic noise in the SRM due to distribution of normal forces across a greater number of phase shifted stator poles [86].

Part of the work in this chapter was presented at the 32nd Annual IEEE Conference on Industrial Electronics, 2006.

2.1 Conventional and Flux-Reversal-Free-Stator SRMs

2.1.1 Conventional two-phase SRM

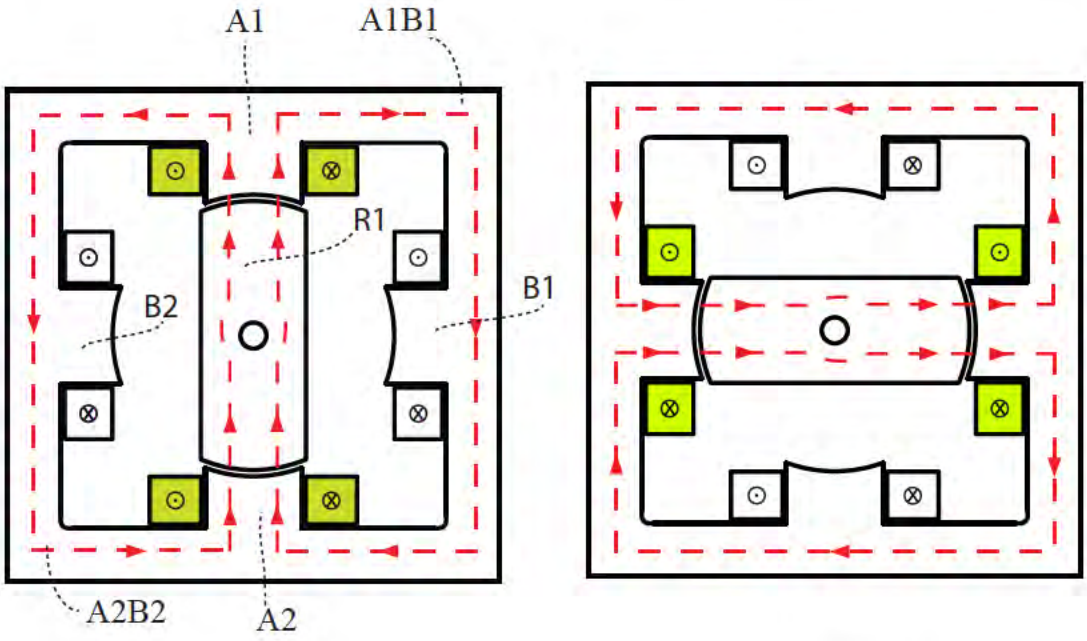

(a) Phase A (b) Phase B

Figure 2.1: Flux paths of a 4/2 SRM

In a conventional two phase SRM with four stator poles and two rotor poles (4/2), radial forces in the air gap are distributed around two stator poles that are diametrically opposite. In two-phase SRMs which differ in the number of stator and rotor poles, radial forces are distributed around pole pairs that are diametrically separated. Furthermore, flux-reversals occurs in sections of the stator yoke during operation. Fig. 2.1 shows the flux-paths of a conventional 4/2 SRM when the two phases are excited independently. The stator yoke section A1B1 and A2B2 experience flux-reversal during commutation.

2.1.2 6/3 Flux-Reversal-Free-Stator SRM (Fig. 2.2)

The 6/3 SRM is comprised of six stator poles and three rotor poles. Fig. 2.2 shows the flux paths when each phase of the 6/3 SRM is excited independently.

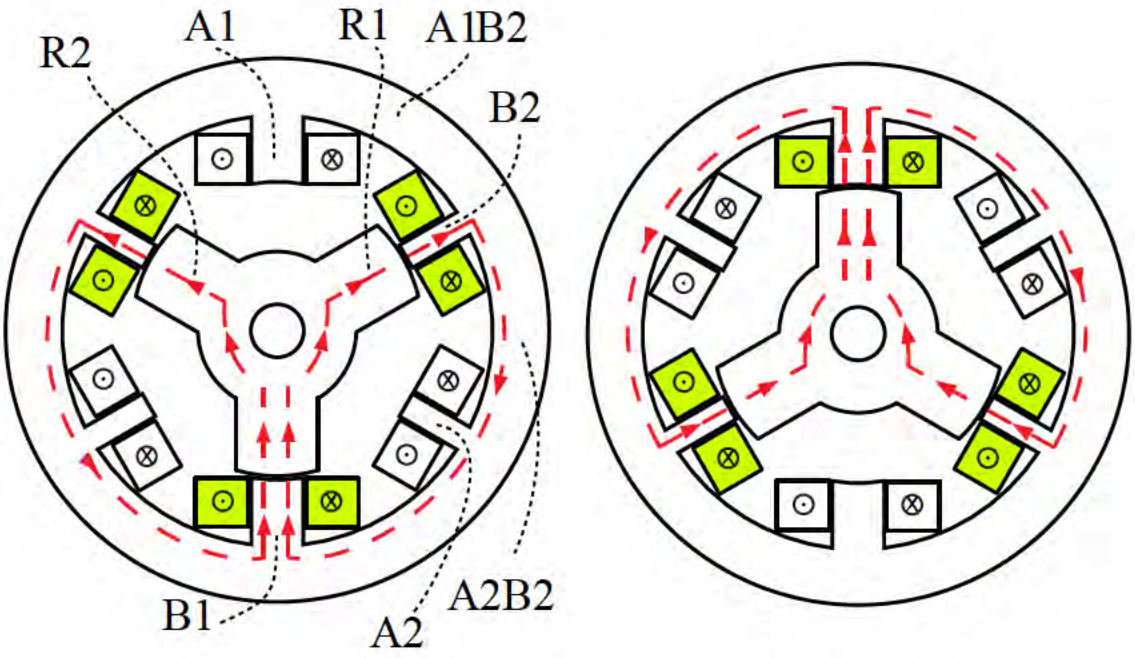

(a) Phase A (b) Phase B

Figure 2.2: Flux paths of a 6/3 SRM

The flux direction in the stator poles and yoke sections are in the same direction regardless of which phase is excited. Furthermore, if both phases are excited simultaneously, due to the unidirectional flux path in the 6/3 SRM, the radial forces are distributed across all six stator poles.

The flux distribution for a 6/3 SRM in different iron sections of the stator and rotor is shown in Fig. 2.4. The zero position in Fig. 2.4 corresponds to the rotor position shown in Fig. 2.2(a). The rotor is rotated counter-clockwise. The stroke angle of a conventional 6/3 SRM is 60^o. The stroke period or angle is defined as the period or angle through which an SRM will generate positive torque in one phase. The flux distribution for the second phase can be derived by shifting the flux distribution waveforms by one stroke period (60^o). A rotor pole and rotor yoke section experiences a flux reversal every 180^o.

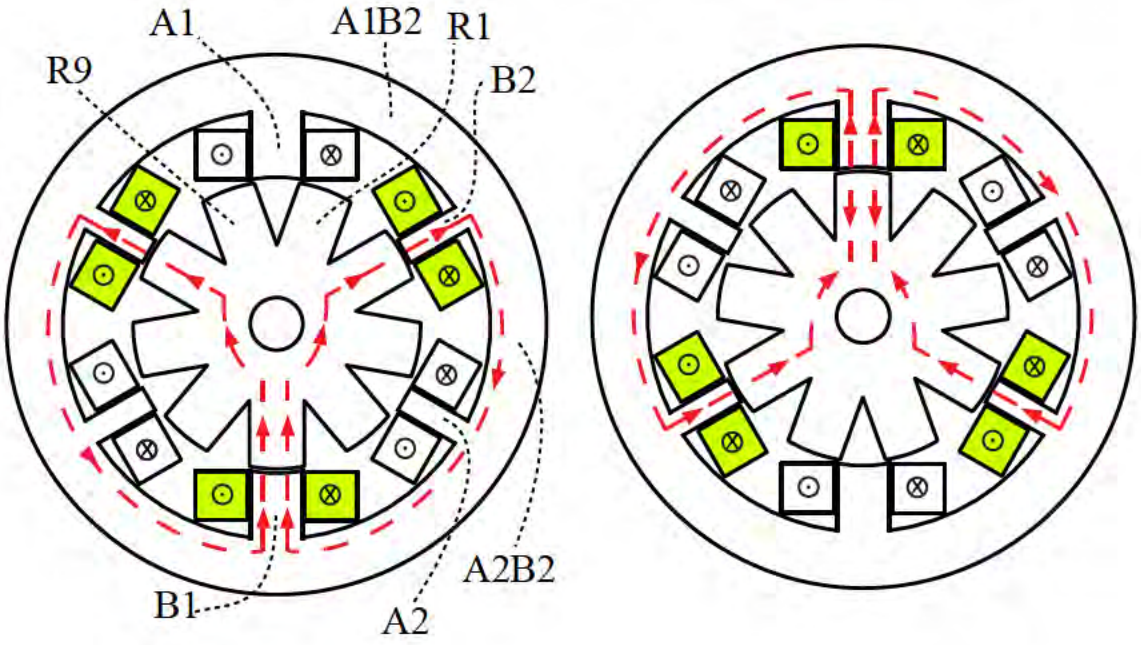

(a) Phase A

(b) Phase B

Figure 2.3: Flux paths of a 6/9 SRM

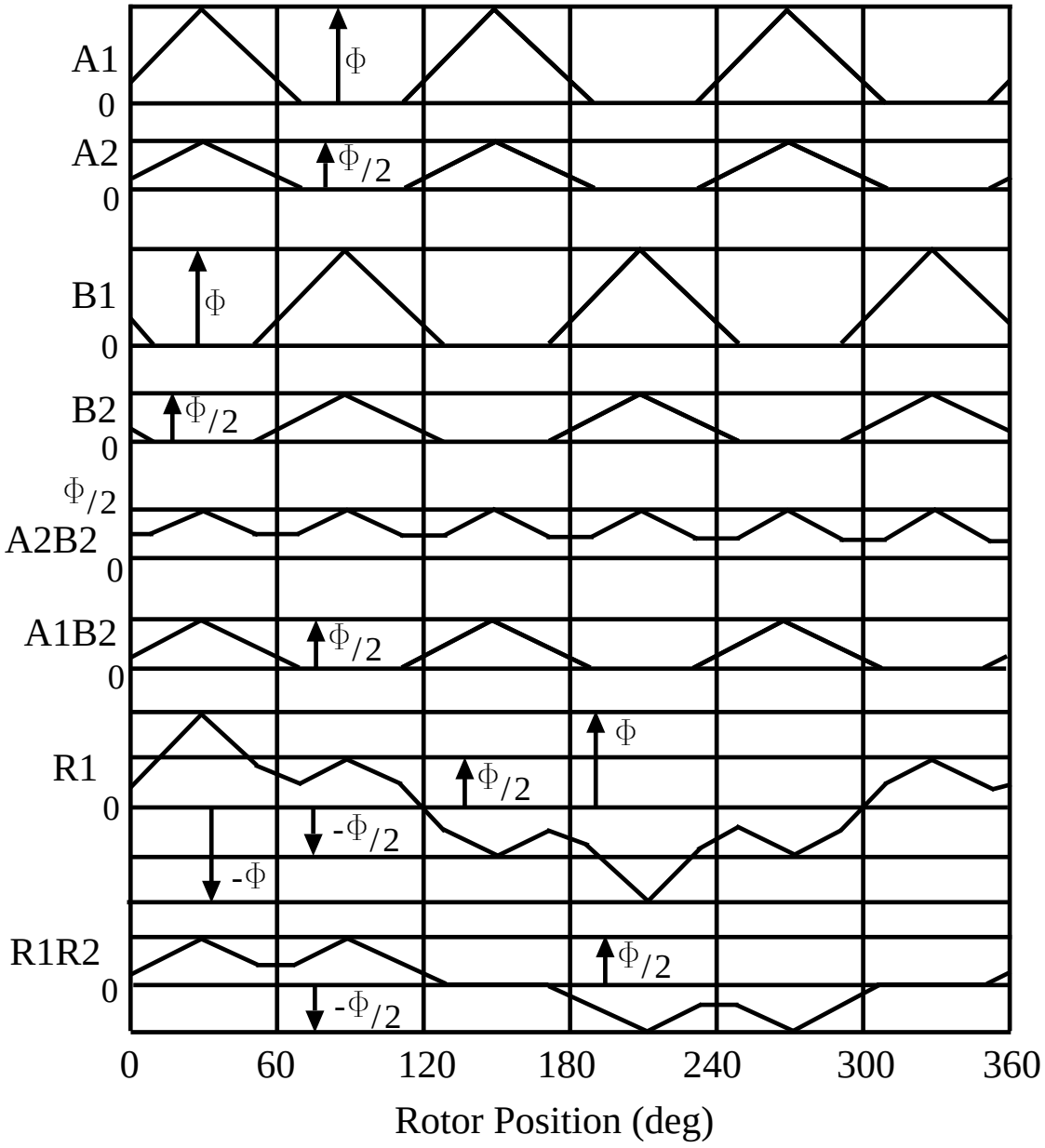

Figure 2.4: Flux distribution for the 6/3 SRM iron sections

2.1.3 6/9 Flux-Reversal-Free-Stator SRM (Fig. 2.3)

The 6/9 two-phase SRM configuration is composed of six stator poles and nine rotor poles. The stroke angle of a conventional 6/9 SRM is 20^o. The flux distribution of the SRM is shown in Fig. 2.5. Rotor poles and the rotor yoke experience a flux reversal every 180^o.

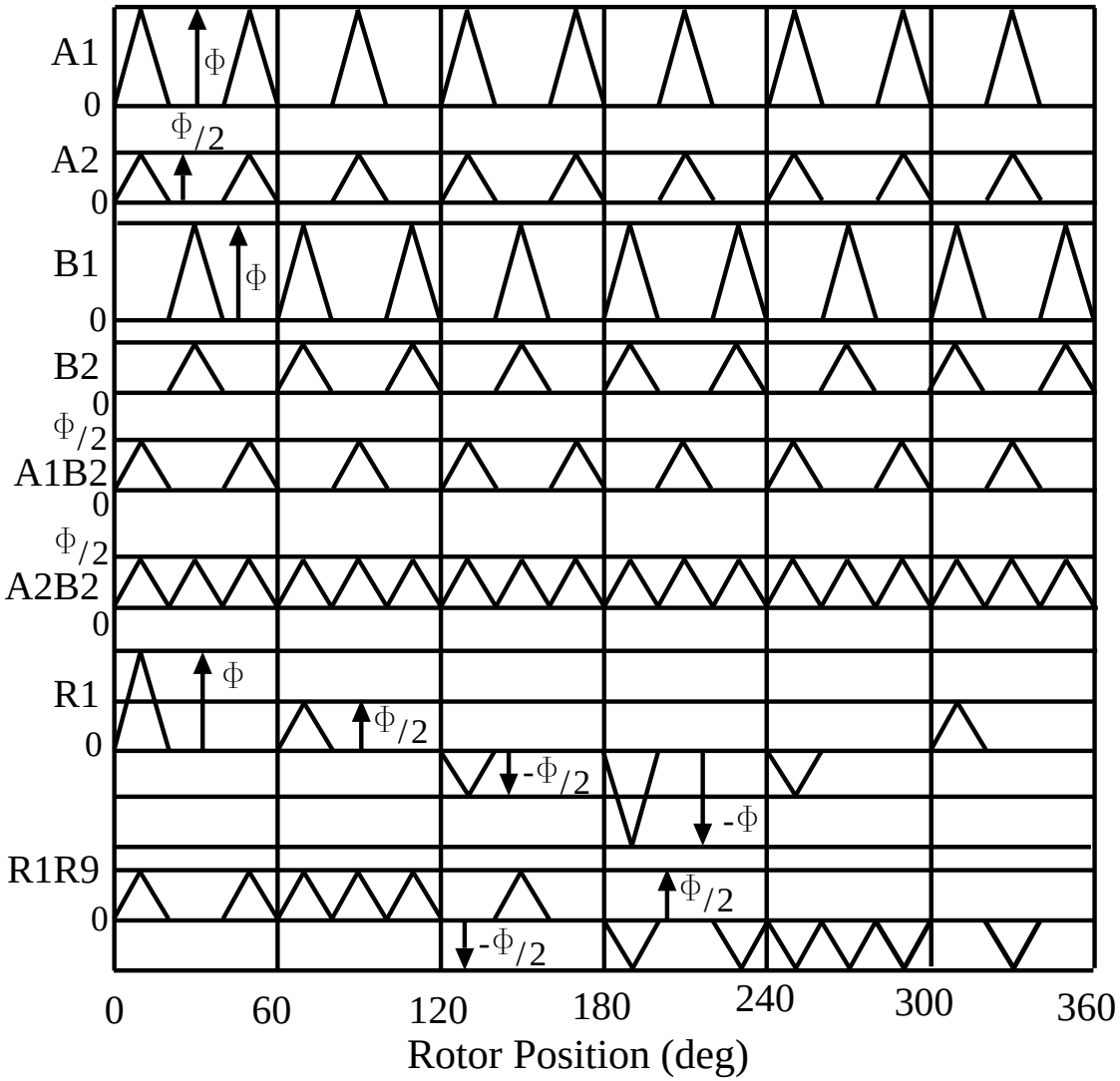

Figure 2.5: Flux distribution for the 6/9 SRM iron sections

2.2 Reduction in core loss in FRF Cores

In this section, the reduction of core-loss in machines with mitigated flux-reversal will be discussed. Reduction in eddy and hysteresis losses will be presented separately.

Assume, the variation of flux in the machine core is sinusoidal. Flux in the conventional iron core with flux reversals will be bipolar and flux in cores not experiencing core-loss can be represented by a rectified sinusoidal waveform. During steady state operation, flux variation in an iron section can be expressed as a function of peak flux density,

$$\Phi_c(t) = B\sin(t) \tag{2.1}$$

where, 't' is time. Similarly, in a FRF free SRM, the unipolar flux variation is,

$$\Phi_n(t) = B|\sin(t)| \tag{2.2}$$

The derivative or rate of change of flux in conventional and FRF SRMs is,

$$\Phi_c'(t) = B\cos(t) \tag{2.3}$$

$$\Phi_n'(t) = B\cos(t)\frac{\sin(t)}{|\sin(t)|} = B\cos(t)\frac{|\sin(t)|}{\sin(t)} \tag{2.4}$$

Core-loss in SRMs can be be expressed by the Steinmetz equation [19],

$$P_{fe} = C_h \cdot f \cdot B_m^{a+b\,B_m} + C_e \cdot f^2 \cdot B_m^2 \tag{2.5}$$

Average eddy loss over one cycle, can be expressed as the square of the rate of change of flux density over one electrical cycle. Therefore, (2.5) can be rewritten as,

$$P_{fe} = C_h \cdot f \cdot B_m^{a+b\,B_m} + C_{e1} \cdot \left(\frac{dB}{dt}\right)^2 \tag{2.6}$$

C_h, f, B_m and C_e are the hysteresis constant, flux frequency, peak flux density and eddy-current loss constant for a given material and operation point. The first term in (2.6) is the contribution of hysteresis loss and the second term is the contribution of eddy-current loss. From (2.3) and (2.4) the eddy-current loss for the conventional and FRFS iron cores are equivalent and the $\frac{dB}{dt}^2$ loss mechanism for both cases in shown in Fig. 2.6. The result also holds under non-sinusoidal excitation.

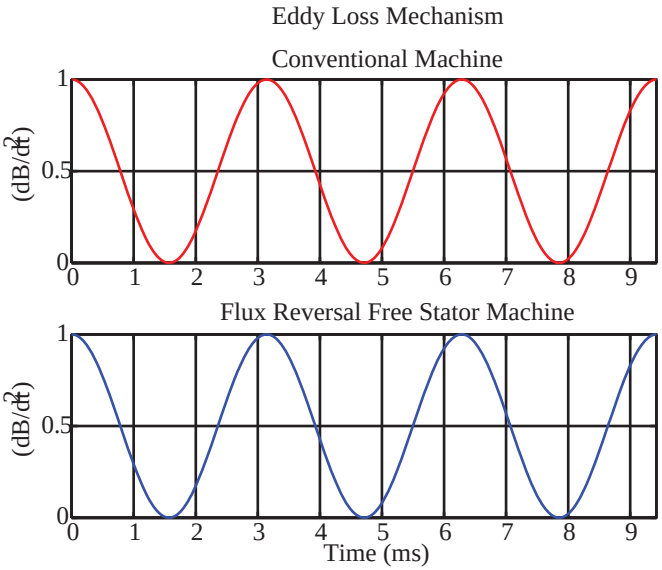

Figure 2.6: $\frac{dB}{dt}^2$ eddy-current loss mechanism in unipolar flux and bi-polar flux iron cores.

In the case of a FRFS SRM, due to the absence of flux reversals, some iron segments have a flux variation which can be expressed as a dc component with a ripple (Fig. 15(a), yoke section Y3). In conventional SRMs, the flux is bipolar and the magnitude of eddy-current loss is higher under the same excitation. Hence a reduction in eddy-current loss is achieved even though the iron is saturated.

The second component of core-loss is hysteresis loss. The area enclosed by the hysteresis loops is the total energy dissipated by hysteresis-loss and is given by,

$$W_h = \oint H \, dB \tag{2.7}$$

Fig. 2.7 shows a hysteresis loss loop under bipolar excitation. For unipolar flux, hysteresis loss is restricted to the first quadrant. The frequency of the unipolar flux is double in the FRFS iron

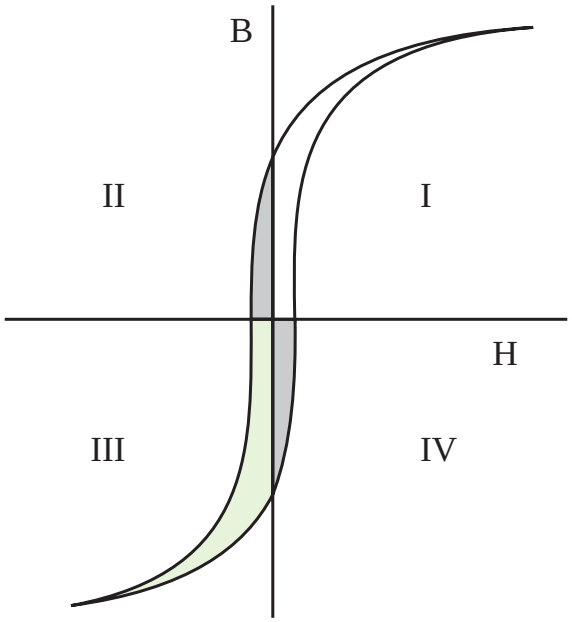

Figure 2.7: Hysteresis energy loop for a ferromagnetic material.

core but the area enclosed by the minor loop less than 50%. The loss due to the shaded regions is not present in the FRF iron core. Furthermore, two-phase machines are designed to have a region where both phases can generate positive torque in order to self-start at any rotor position. In the FRFS SRM, flux from both phases will always be additive instead of destructive, which results in lower core loss.

2.3 Design procedure for the 6/3 and 6/9 SRMs

The power density of any machine is proportional to the volume of a cylinder encapsulating the air gap of the machine.

$$P \propto (2r)^2 L_z \tag{2.8}$$

where L_z is its stack length of the SRM.

Let k_d be the electrical duty cycle of each phase. The duty cycle of the phase is greater than 0.5 for overlap in the conduction period of both phases, in order to generate continuous positive

torque. Let k_e be the desired efficiency of the SRM. Define constants:

$$\sigma_s = \frac{L_a^s}{L_a^u} \tag{2.9}$$

and

$$\sigma_u = \frac{L_a^u}{L_u} \tag{2.10}$$

where L is self-inductance of a phase, subscripts a and u denote the unaligned and aligned positions, respectively, and superscripts, u and s denote the unsaturated and saturated cases of self-inductance.

The desired average output torque at the desired operating for the SRM can be written as,

$$T_{avg} = \frac{1}{2} i^2 \frac{dL}{d\theta} = \frac{1}{2} i^2 \frac{L_a^s}{\theta_i} \left(1 - \frac{L_u}{L_a^s}\right) \tag{2.11}$$

where, θ_i is the conduction angle corresponding to the duty cycle k_d.

$$\theta_i = \frac{360 k_d}{2 P_r} \tag{2.12}$$

where P_r is the number of rotor poles. At the rated operating point the average back-emf of an SRM is equal to the available dc bus voltage from the power converter (neglecting losses).

$$v \cong \frac{d\lambda}{dt} = i\ \omega_m \frac{L_a^s - L_u}{\theta_i} \tag{2.13}$$

From 2.11 and 2.13, for a desired average speed and torque, constants (2.9) and (2.10) can be estimated.

The power output for an SRM is given by [37],

$$P = \frac{\pi^2}{120} \left(1 - \frac{1}{\sigma_s \sigma_u}\right) k_e\ k_d\ B\ A_s\ N_r\ (2r)^2\ L \tag{2.14}$$

where B be the average aligned flux density in the main pole of the SRM. The average flux density of main and auxiliary stator poles are the same. Let the ratio between the machine‘s bore and stack length be k. Let the main stator pole arc to be θ_{mp} and rotor pole arc to be θ_{rp}. The main rotor pole arc must be chosen to be greater than the θ_i. The output power can then be rewritten as,

$$P = \frac{\pi^2}{120} \left(1 - \frac{1}{\sigma_s \sigma_u}\right) k_e\ k_d\ B\ A_s\ N_r\ (2r)^2\ k \tag{2.15}$$

For a given radius r if the air gap, the magnetic field intensity in the air gap is calculated as,

$$H_g = \frac{B \ \ A_{mp}}{\mu_o A_g} \tag{2.16}$$

A_{mp} is the area of the main stator pole and A_g is area of the air gap calculated by estimating the effective length and width of the air gap after correction with Carter‘s coefficients, show in section 2.6.

The total number of turns per phase can be estimated by,

$$T_p h = \frac{l'_g H_g}{i} \tag{2.17}$$

The height of the stator yoke is,

$$H_s = \frac{1}{2}D - r - \frac{1}{2}r\theta_{mp} \tag{2.18}$$

where D is the outer diameter of the SRM.

Since each auxiliary stator pole carries half the flux, the pole arc of the main stator pole is,

$$\theta_a = \frac{1}{2}\theta_{mp} \tag{2.19}$$

and the height of the rotor yoke is equal to the height of the stator yoke because they carry the same flux as the rotor.

2.4 Basis for comparison

Several parameters and design criteria are applied to the design of the two machines. These parameters are:

- self-starting capability is incorporated into both SRMs to reduce cost and increase efficiency;
- the nominal operating voltage is 325 V-dc ;
- minimum radial air gap length between the stator and rotor is set to 0.3 mm;
- M19 steel is used for stator and rotor laminations;
- shaft diameter is same for both machines;

- stator frame used in designing both SRMs are same, hence the outer diameter of both machines is limited;
- operating speed of both machines is 1800rpm;
- rated torque of the SRMs is 3.75 N-m;
- asymmetric rotor pole faces are utilized in the design of the SRMs in order to facilitate torque profiling for self-starting and torque ripple reduction.

2.5 Results of the Comparison

2.5.1 SRM Dimensions

The 6/3 SRM was designed first and provided a benchmark for designing the 6/9 SRM. Once the 6/9 SRM lamination shape was optimized for torque production, the current ratings of the two machines were chosen to be the same leading to a lesser weight of the 6/9 SRM and hence a lower cost machine. The rated current for both machines is 10A. The 6/3 SRM has a heavier stator, rotor and windings when compared to the 6/9 SRM. The rotational inertia of the 6/3 rotor is approximately 3.5 times greater than the 6/9 rotor. This is due to the lower volume and weight of the rotor is which greatly affected by stack length. The 6/9 SRM has 30% less stack height than the 6/3 SRM. Keeping the stack length of both machines equal would result in a 15% lower rated current in the 6/9 SRM for the same operating conditions. Depending on the application requirements, a lower rated current may be more important than a lower machine weight. For the purpose of this comparison, the rated current of both SRMs are taken to be the same. The dimensions of the SR machines designed for the comparison are summarized in Table A.1 in appendix A.1.

2.5.2 Inductance Profile

Static inductance profiles of the 6/3 and 6/9 SRMs for various phase currents are shown in Fig. 2.8. The positive inductance slope region of the 6/3 SRM is approximately 75^o which is greater than the its conventional stroke angle (60^o) resulting in an overlap between the positive inductance slopes of the two phases. The rotor poles of the 6/3 and 6/9 SRMs have non-uniform pole faces and wide pole arcs in order to maximize the positive inductance slope region. The positive inductance

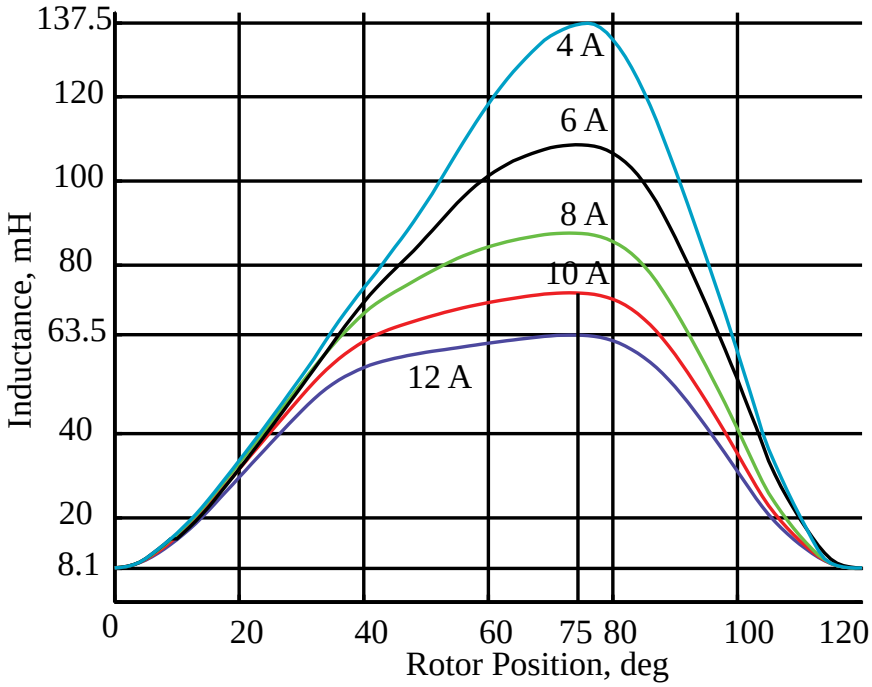

(a) 6/3 SRM

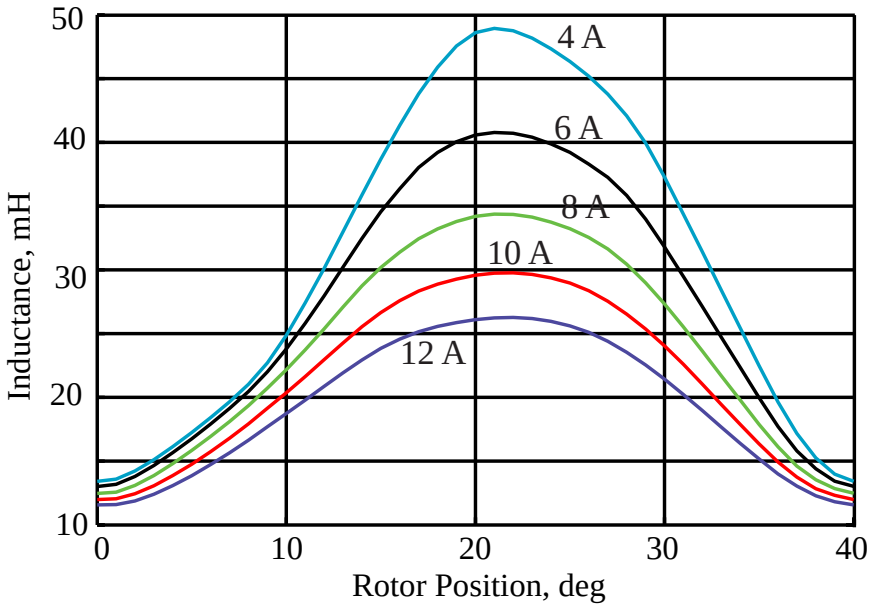

(b) 6/9 SRM

Figure 2.8: Static inductance profiles of both SRMs for various currents

slope region is approximately 2^o greater the conventional stroke angle of 20^0 in the 6/9 SRM. An overlap in the rising inductance regions between the two phases also facilitates unidirectional self-starting at any rotor position. This feature can be seen in the torque profiles of the two machines which is shown in the following section. The lesser rotor pole pitch of the 6/9 SRM is unfavorable toward increasing the positive inductance slope region. Pole pitch is defined as the angle between the centers of two adjacent rotor poles.

2.5.3 Torque Profiles

The overlap in the positive inductance slope between the two phases of both SRMs results in an overlap in the positive torque generated by each phase. Fig. 2.9 shows the positive torque profiles of the 6/3 and 6/9 SRMs. This overlap allows for positive torque generation at all rotor positions.

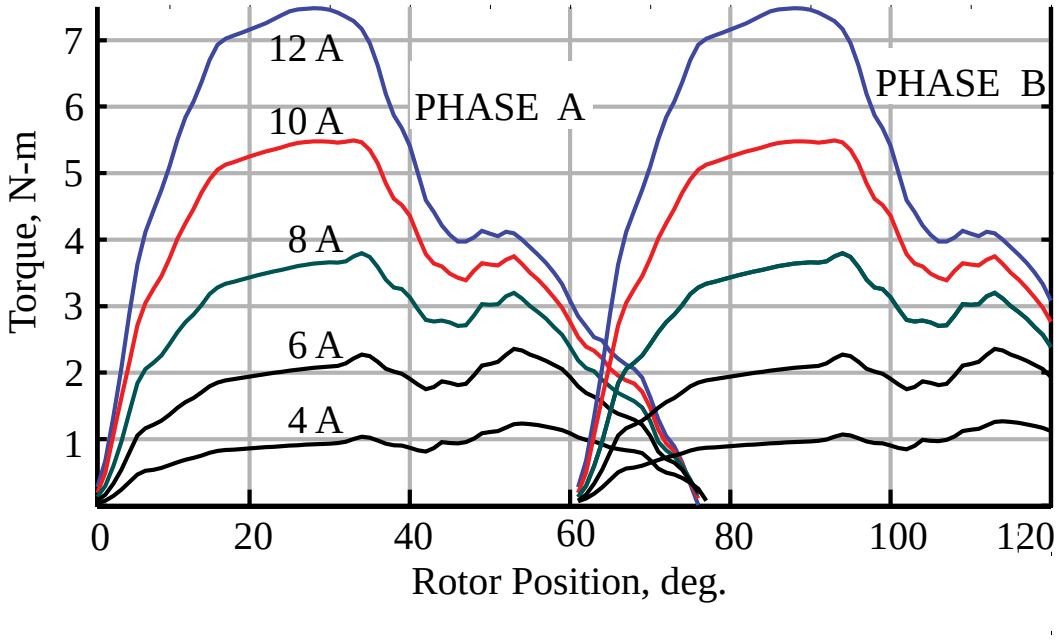

(a) 6/3 SRM

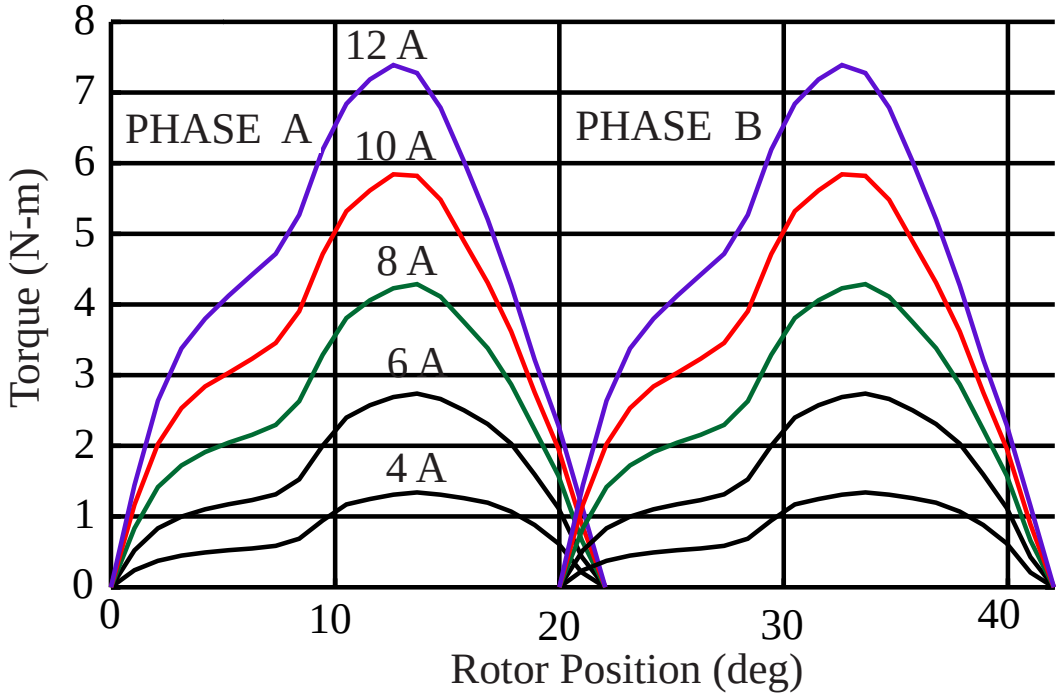

(b) 6/9 SRM

Figure 2.9: Static torque profiles of both SRMs for various currents

Hence self starting without external parking mechanisms for unidirectional rotation is achieved for both SRMs. The magnitude of the net torque generated by both phases in the overlapping region of the 6/3 SRM is greater than that of the 6/9 SRM. The lower rotational inertia of the rotor in the 6/9 SRM lends itself to a lesser amount of torque that is required to start the SRM from standstill. There is a 20% overlap between the torque generated by both phases of the 6/3 SRM and approximately 10% overlap in the 6/9 SRM. The larger rotor pole pitch of the 6/3 SRM allows greater flexibility in shaping the rotor pole to distribute torque over a wider stroke angle without sacrificing power density. Increasing the rotor pole arc in the 6/9 SRM by 4^o resulted in a 21% drop in average static torque. The average torque with respect to phase currents is shown in Table 2.1.

Table 2.1: Comparison of the average static torque in the two SRMs

Current	6/3 SRM	6/9 SRM
4	0.8	0.8
6	1.7	1.7
8	2.6	2.7
10	3.5	3.7
12	4.5	4.7

Fig. 2.10 shows the torque ripple in the SRMs during dynamic simulation at 1800 rpm. An asymmetric converter is used to drive the two SRMs. The 6/3 and 6/9 SRMs have advanced excitation angles that are 6^o and 1.5^o, respectively and advanced commutation angles which are 15^o and 3^o, respectively. The 6/9 SRM has a greater torque ripple than the 6/3 SRM with a rated load of 3.75 N-m on both machines. The peak-to-peak torque ripple is 5.1 N-m for the 6/3 SRM and approximately 7 N-m for the 6/9 SRM.

Fig. 2.11 shows the normalized power spectrum of the electromagnetic torque shown in Fig 2.10. The 6/3 SRM has a phase switching frequency of 90 Hz at 1800rpm. The first and second harmonics are the most dominant frequencies in the electromagnetic torque for the 6/3 SRM because of two phases. The 6/9 SRM has a phase switching frequency of 270 Hz at 1800 rpm and its torque shows that the second harmonic to be most dominant frequency because of two phases. When these

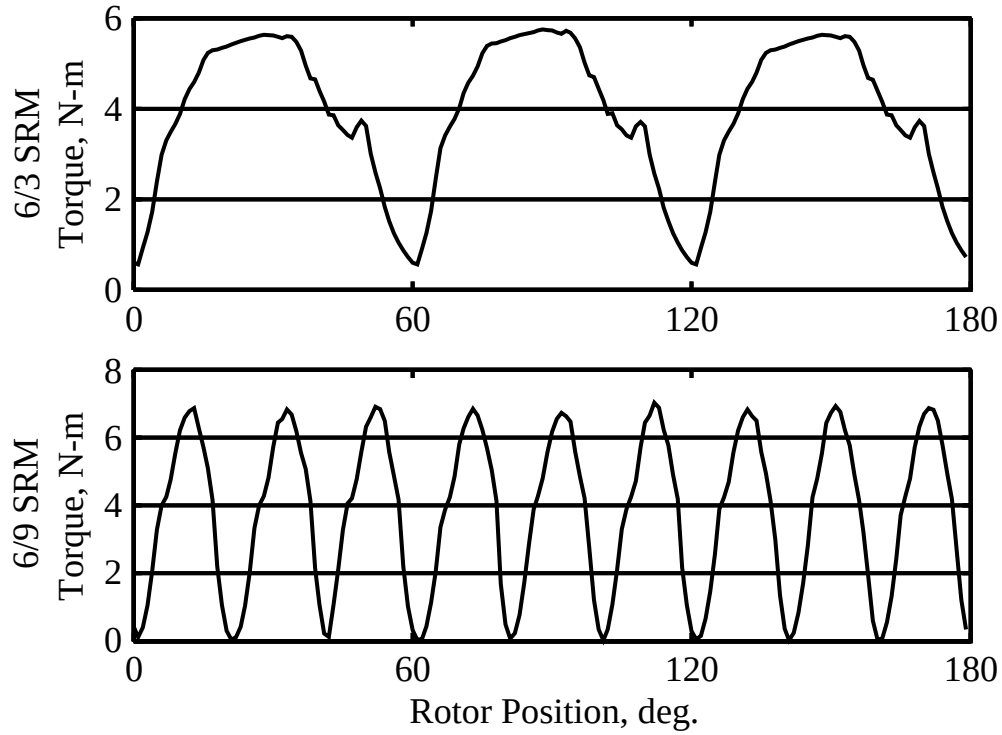

Figure 2.10: Simulated electromagnetic torque at 1800 rpm with 3.75 N-m load

torque harmonics correspond to a vibration mode frequency of the stator, undesirable audible noise is amplified.

2.5.4 Normal/Radial Forces in the Air Gap

Radial and tangential forces in SRMs play a major role in generating undesirable acoustic noise. Majority of the normal forces are concentrated in the regions around the excited stator poles. Instantaneous forces in the air gap are estimated by evaluating the Maxwell stress tensor directly in FE software. The Maxwell stress tensor is sensitive to location of the contour over which the radial force is calculated and the quality of the mesh which the contour passes through. The contour over which the the maxwell stress tensor is integrated is placed very close to the stator pole surfaces (0.02 mm). Ideally the contour would need to be placed on the inner surface of the stator. It is assumed all the radial force is concentrated on the pole faces of the stator poles.

The global force acting on a body can be calculated by integrating the Maxwell stress tensor over a closed surface. Therefore, the global force density can be expressed as, [66],

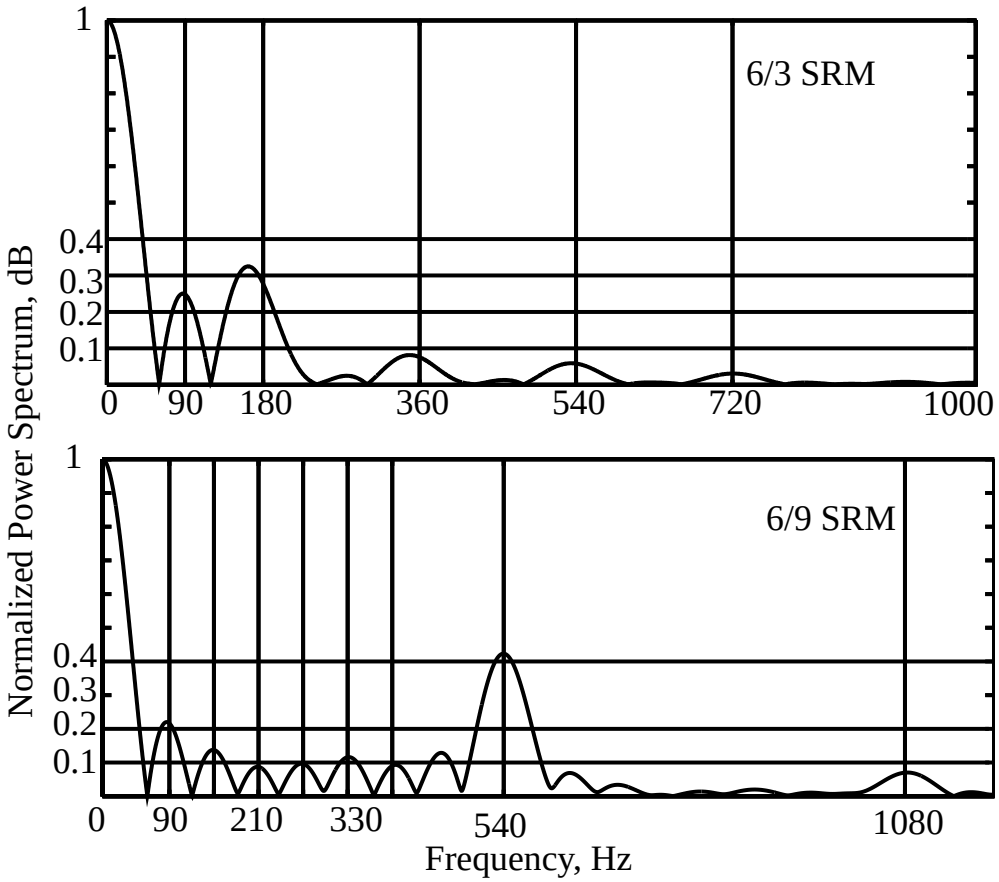

Figure 2.11: Normalized power spectrum of the electromagnetic torque for both SRMs at 1800rpm

$$\begin{aligned}
\overrightarrow{F} &= \oint (\mathbf{T} \cdot \overrightarrow{n})\, ds \qquad (2.20)\\
&= \oint \left(\overrightarrow{H} \left(\overrightarrow{B} \cdot \overrightarrow{n} \right) - \frac{1}{2} \overrightarrow{n} \left(\overrightarrow{B} \cdot \overrightarrow{H} \right) \right) ds \\
&= \oint \left(\frac{1}{\mu_o} \overrightarrow{B} \cdot B_n - \frac{1}{2\mu_o} \overrightarrow{n} \left(\overrightarrow{B}^2 \right) \right) \\
&= \oint \left(\frac{1}{\mu_o} B_n B_t \overrightarrow{t} + \frac{1}{2\mu_o} \left(B_n^2 - B_t^2 \right) \overrightarrow{n} \right) ds \qquad (2.21)
\end{aligned}$$

where $\mathbf{T}$ is the maxwell stress tensor, $\overrightarrow{n}$ and $\overrightarrow{t}$ are the unitary normal vector and tangential vector, on the contour, respectively. B_t and B_n are the tangential and normal component of the flux density, respectively. The first term of (2.21) is normal force, and the second term is tangential force.

2.6 Analytically estimating peak force unbalance

Maximum radial force occurs at the fully aligned position when the flux density is maximum for a phase current. The presence of unbalanced radial force can be estimated analytically to check for the presence of unbalance.

In the fully aligned position, the rotor does not generate torque, because the derivative of inductance is zero at that rotor position for all currents. Assume, the flux density vector in the air gap between the stator and rotor has a purely normal component.

The average radial air gap length between the main stator pole and rotor is, $\bar{l}_{gm}$. The average radial air gap length between the an auxiliary stator pole and rotor is, $\bar{l}_{ga}$. Due to the presence of slots between the stator poles, the effect width of the air gap can be estimated in accordance to Carter's principle. Since the flux density decreases gradually between the slots of the stator and rotor, the effect of fringing flux, the effective length and width of the air gap between the stator and rotor is not equal to the overlap width between the stator and rotor.

The width of the portion of the slot between stator poles where the flux density is essentially zero is given by [79],

$$w_e = k \cdot w_s \tag{2.22}$$

where, w_s is the length of the slot and k is the correction factor, which is expressed as,

$$k_{\{m,a\}} = \frac{2}{\pi}\left[\tan^{-1}\left(\frac{w_{s\{m,a\}}}{\bar{l}_{g\{m,a\}}}\right) - \frac{2\, l_{g\{m,a\}}}{w_{s\{m,a\}}} \ln\sqrt{1+\left(\frac{w_{s\{m,a\}}}{\bar{l}_{g\{m,a\}}}\right)^2}\right] \approx \frac{\frac{w_{s\{m,a\}}}{\bar{l}_{g\{m,a\}}}}{5+\frac{w_{s\{m,a\}}}{\bar{l}_{g\{m,a\}}}} \tag{2.23}$$

The slots widths for the main poles and auxiliary poles are not equal since the auxiliary poles carry only half the total flux. The slot width around the main pole is,

$$w_{sm} = r\frac{\pi}{2} - r\left(\frac{\pi}{3} + \frac{\theta_{ap}}{2} + \frac{\theta_{mp}}{2}\right) \tag{2.24}$$

where θ_{mp} is the arc of the main pole, θ_{ap} is the arc of the auxiliary pole and r is the average radius of the air gap between the stator and rotor.

The average slot width around the auxiliary rotor pole is,

$$w_{sa} = \frac{1}{2}\left[2r\left(\frac{\pi}{3} - \frac{\theta_{ap}}{2}\right) + w_{sm}\right] \tag{2.25}$$

The effective air gap width width for the main and auxiliary poles, respectively, are:

$$w_{em} = r \cdot \theta_{mp} + w_{sm}(1 - k_m) \tag{2.26}$$

$$w_{ea} = r \cdot \theta_{ap} + w_{sa}(1 - k_a) \tag{2.27}$$

The Carter factor for the main and the auxiliary stator pole, respectively, are,

$$k_{cm} = \frac{w_{msp}}{w_{msp} - k_m w_{sm}} \tag{2.28}$$

$$k_{ca} = \frac{w_{asp}}{w_{asp} - k_a w_{sa}} \tag{2.29}$$

The equivalent length of the air gap for the main and auxiliary rotor poles, respectively, become,

$$l'_{gm} = k_{cm} \cdot \bar{l}_{gm} \tag{2.30}$$

$$l'_{ga} = k_{ca} \cdot \bar{l}_{ga} \tag{2.31}$$

Since the main poles carry the total flux from the phase and the rotor poles carry only have the total flux, the radial force per axial length in the aligned position can be approximated for the main and auxiliary poles, respectively,

$$F_m = \frac{B_{gm}^2}{2\mu_o} w_{em}, \mathrm{N/m} \tag{2.32}$$

$$F_a = \frac{\left(B_{gm}\dfrac{w_{em}}{2w_{ea}}\right)^2}{2\mu_o} w_{ea}, \mathrm{N/m} \tag{2.33}$$

where B_{gm} is average flux density in the air gap of the main stator pole. The average flux density of the auxiliary pole is expressed as a function of the flux density in the main stator pole air gap.

The peak unbalance radial force becomes,

$$F_u = F_m - 2F_a \cos\left(\frac{\pi}{3}\right) = F_m - F_a \tag{2.34}$$

2.6.1 Radial force simulation results

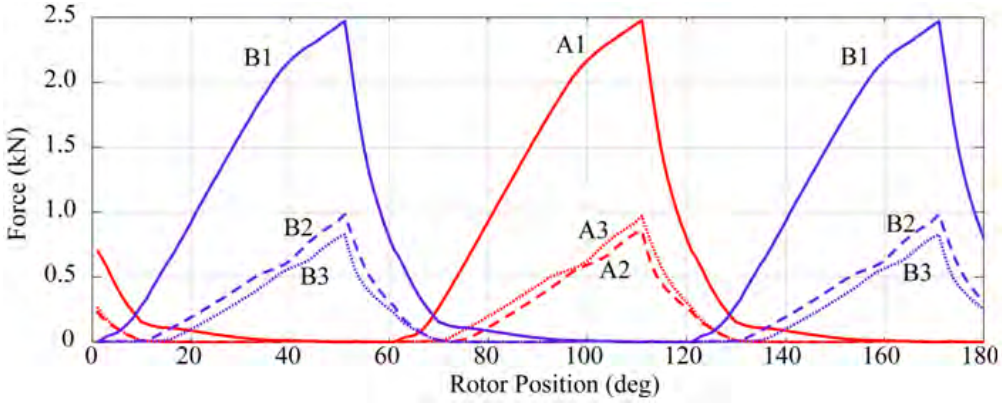

(a) 6/3 SRM

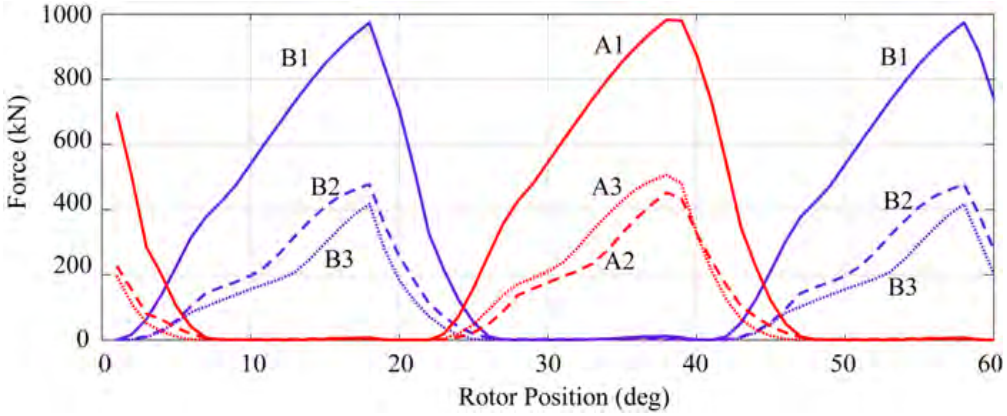

(b) 6/9 SRM

Figure 2.12: Radial force vs. rotor position for the 6/3 and 6/9 SRMs during operation

Figs. 2.12(a) and 2.12(b) show the average radial force around the three excited stator poles which is calculated from the force densities around each stator pole for each rotor positioninstanta-

neous radial force in the air gap around the stator poles for the 6/3 and 6/9 SRMs respectively. The force results are plotted under the same load conditions as the dynamic FEA simulations earlier with 3.75 N-m load. Radial force around the the auxiliary stator poles is less than that of the main pole because each pole carries half the flux of the main pole and has a smaller pole arc. Fig. 2.13 shows the resultant force magnitude after taking the vector sum of the radial forces along the center of the main stator poles. The radial force shows an unbalance in the direction of the main poles as the phases operate. The peak radial force resultant for the 6/3 SRM is three times greater th an the 6/9 SRM. The area of the rotor pole and stator pole faces in the 6/9 are approximately one-third of the stator and rotor pole faces in the 6/3 SRM while the average torque versus phase current are the same in both machines. This difference in pole face area and the gearing effect due to higher pole count give the 6/9 SRM the lower radial force unbalance advantage over the 6/3 SRM.

The maximum flux density for stator poles, by design, is the knee-point of the stator core‘s B-H characteristics. For the stator core material used in the designed machines, the knee point is approximately 1.65 T. The mean flux density in the air gap of the main stator pole of the 6/3 SRM is,

$$B_{gm} = 1.65\frac{w_{em}}{r\theta_{mp}} = 1.48 \tag{2.35}$$

The peak unbalance radial force becomes,

$$F_u = F_m - 2F_a \cos\left(\frac{\pi}{3}\right) = 1.63\text{kN} \tag{2.36}$$

The peak unbalance force for the 6/3 SRM at the aligned position from finite element simulations is 1.44 kN. The error from estimating the peak unbalance force at the rated operating point for the 6/3 SRM by rapid analytical calculations and time-consuming finite element simulations is 12%, which is within an acceptable range, given the rapid nature of the calculations, which does not include the effects of magnetic saturation at the rated operating point.

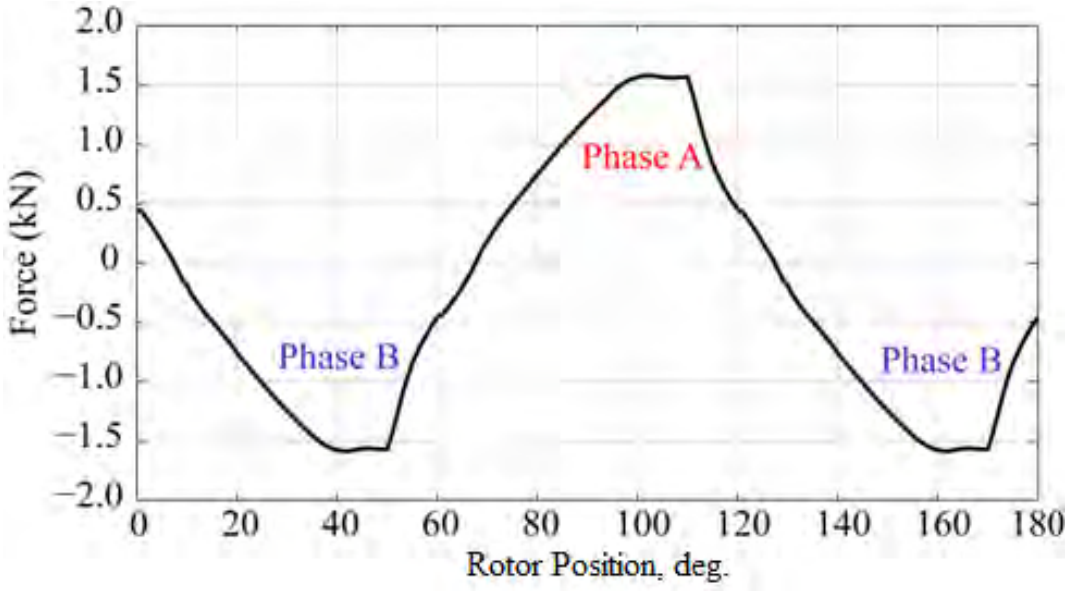

(a) 6/3 SRM

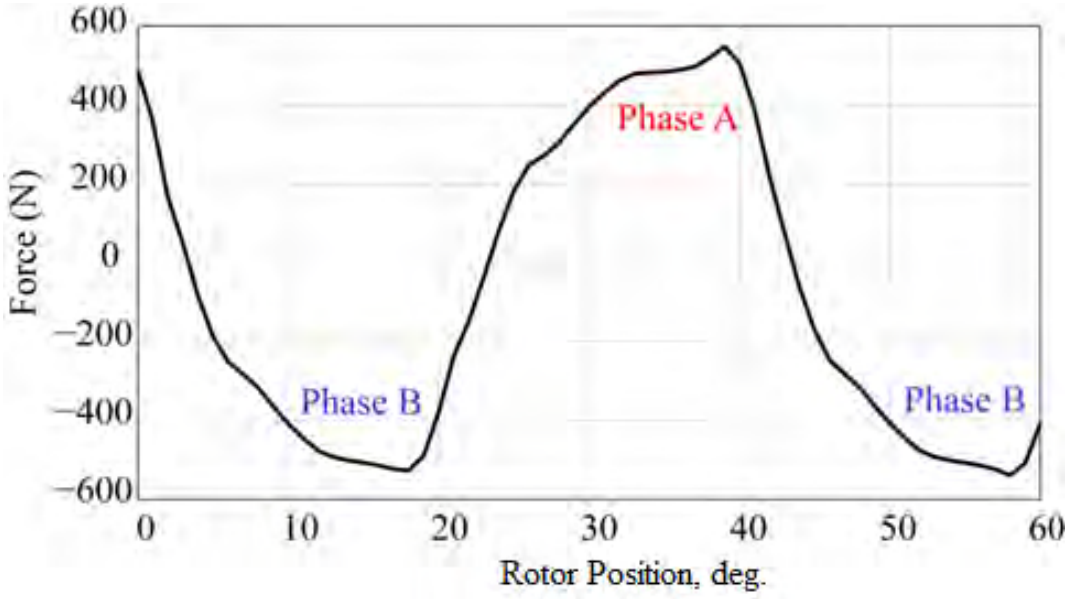

(b) 6/9 SRM

Figure 2.13: Radial forces resultant for both SRMs

2.6.2 On balancing of normal forces

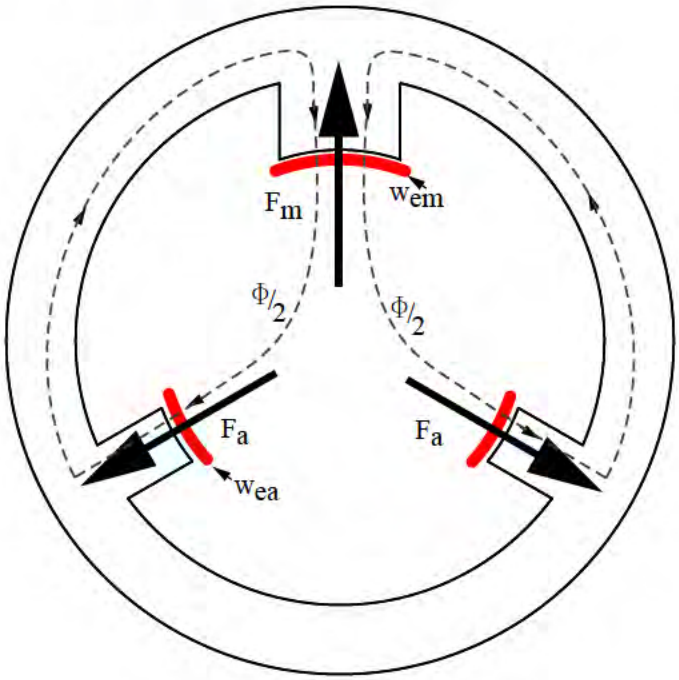

Figure 2.14: Balancing of radial forces in the 6-stator pole SRM

A simple way to envision the balancing of radial forces is illustrated in Fig. 2.14. The force around the main pole would have to be canceled by the auxiliary poles. The ratio of the effective width of the auxiliary air gap to the main air gap for balanced radial forces is,

$$\frac{F_m}{F_a} = \frac{4w_{ea}}{w_{em}} = 1 \tag{2.37}$$

The pole arc of the auxiliary pole would have to be, approximately, one-fourth of the main pole arc. Since each auxiliary pole carries half the flux of the main pole, reducing pole width to one quarter would result in higher saturation and lower power density.

2.6.3 Core Losses

Core losses are proportional to the frequency of the flux, the magnitude of the flux density and weight of material traversed by the flux. A unique feature of the 6/3 and 6/9 SRMs is that the stator and rotor pole combinations gives give two-third utilization of the stator and rotor back

irons at any time of its operation thus resulting in smaller flux paths. In conventional SRMs flux traverses the entire stator yoke resulting in greater core losses. Smaller flux paths require smaller magneto motive force (mmf) leading to higher efficiency during operation. Dynamic FE simulations

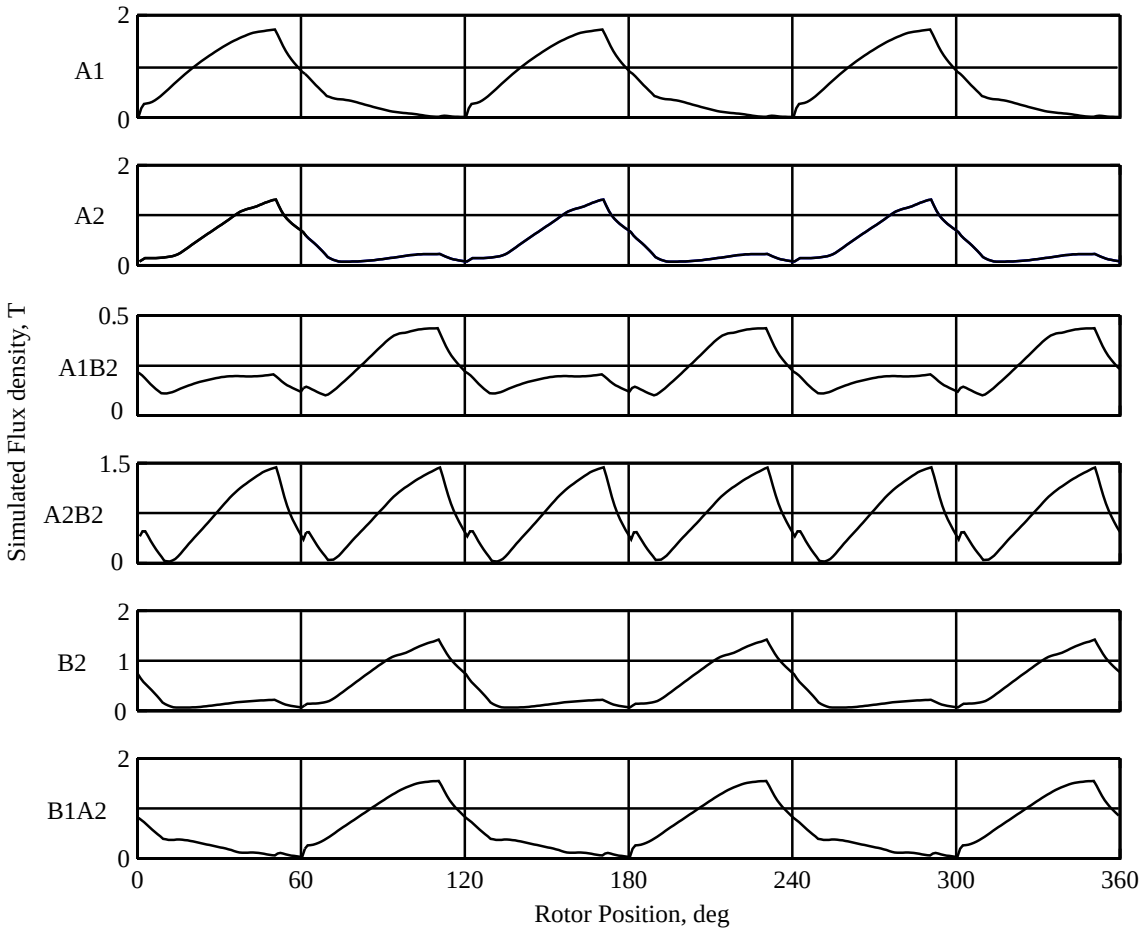

Figure 2.15: Balancing of radial forces in the 6-stator pole SRM

of the SRMs at 1800 rpm with asymmetric converter are performed and the average flux densities for each stator and rotor section are calculated for every degree of rotation. The average flux densities are curve fitted using fourth-order polynomial equations. Eddy losses can then be directly by integrating for energy the curve fitted flux density expressions using (2.5). Fig 2.15 shows the flux densities in the various stator iron section from dynamic simulations for the 6/3 SRM. A subset of the custom polynomial expressions and their integration in Matlab are included in Appendix A.3. Hysteresis losses in the stators of both SRMs are reduced due to unipolar flux waveforms. The eddy and hysteresis losses for both machines are given in Table 2.2.

Table 2.2: Core-loss estimate for the two machines, W

	6/3 SRM		6/9 SRM	
	Eddy	Hysteresis	Eddy	Hysteresis
Stator	6.0	7.6	14.5	11.1
Rotor	3.3	4.9	6.3	5.4
Total	22		38.3	

The core-losses for the 6/3 SRM is 43% lower than the 6/3 SRM due to the lower phase switching frequency of the 6/3 SRM. The phase switching frequency of the 6/3 SRM is three times greater than the 6/9 SRM but the 6/9 SRM has 36% less weight than the 6/3 SRM.

2.7 Experimental Results

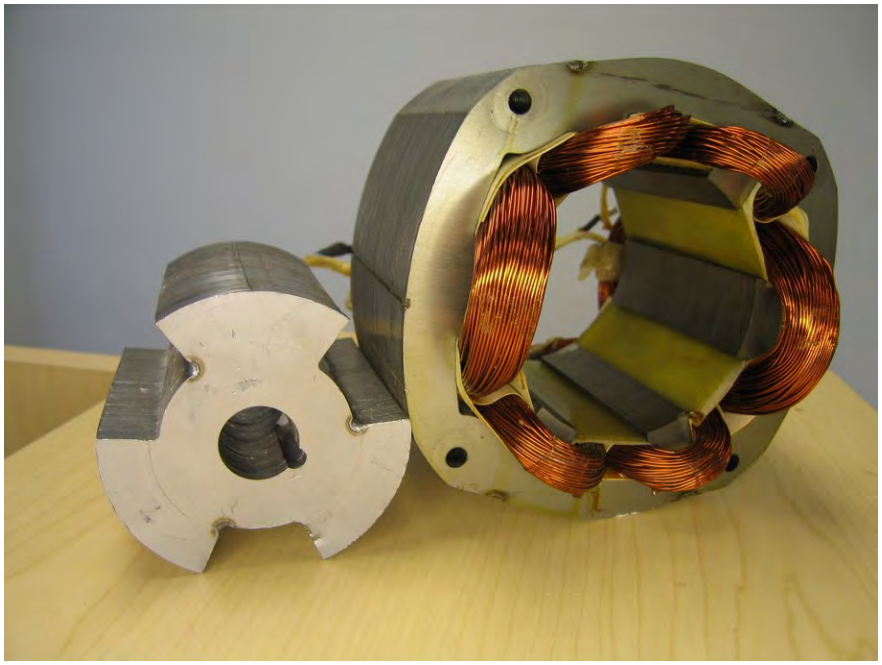

Figure 2.16: Experimental setup used to measure inductance characteristics of the 6/3 SRM.

A prototype of the designed 6/3 SRM was available for correlation of the inductance profile from FE simulations to verify the validity of the design of the SRMs. Fig. 2.18 shows the measured and

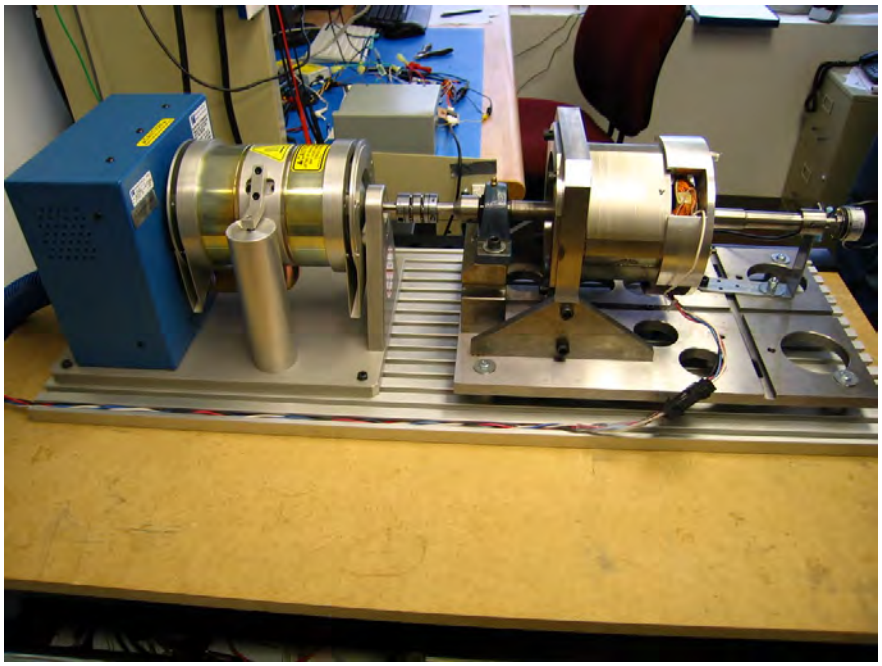

Figure 2.17: Rotor and stator of the 6/3 SRM used to measure inductance characteristics.

FEA inductance of the 6/3 SRM for three currents. There is good correlation of the inductance from FEA and measured values at high saliency ratios and small error at high currents which is an acceptable error given the error in the material data provided by the manufacturer and eccentricities in the air gap of the prototype machine.

2.8 Summary and Conclusions

This chapter compared two SRM configurations with no flux-reversal in the stator. The following contributions and conclusions can be drawn from the analysis,

- 6/3 SRM is advantageous for torque profiling with asymmetric rotor pole faces without greatly sacrificing power density.
- 6/9 SRM has higher power density for the same operating conditions as the 6/3 SRM.
- Both SRMs are capable for self-starting from any position for unidirectional rotation and have no flux reversals in the stator iron. This makes this class of SRMs the first to have no flux-reversal in the stator iron which reduces core loss and increases efficiency.

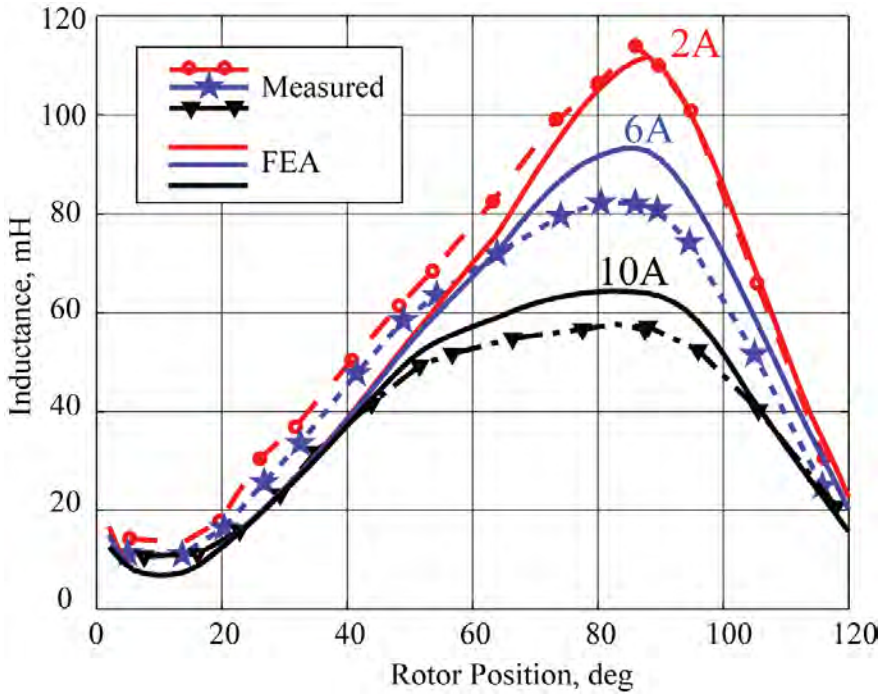

Figure 2.18: Experimentally measured inductance correlated with FEA inductance of the designed 6/3 SRM

- A machine procedure for the 6/3 and 6/9 SRMs have been derived from fundamental equations for the first time.
- Radial force analysis of both machines are conducted through fundamental equations and finite element simulations. Due to the gearing effect of having higher number of rotor poles, the 6/9 SRM has lower unbalanced radial forces than the 6/3 SRM and higher torque density.
- Unbalanced radial forces can not be eliminated without significant loss in power density of the machine. This is a drawback of this class of SRMs and can lead to premature failure of the bearings in these machines.
- Core loss in both machines are evaluated through fundamental Steinmetz equations to show the lower core loss in this class of SRMs.

Chapter 3

Doubly Salient PM Flux Reversal Free Switched Reluctance Machine (DSPMSRM)

This chapter presents the evolution, modeling and enhancements of the novel DSPMSRM. Due to the drawbacks of the first FRFS SRM, the e-core and its derivate the 4ecore SRM were developed and they displayed balanced normal forces. The derivation of a doubly salient permanent magnet assisted SRM in Section 3.1. The new DSPMSRM takes advantage of the shared pole to increase power density of the 4ecore SRM further. Non-linear modeling of the DSPM is presented in Section 3.3 followed by static and dynamic simulation results.

3.1 Novel DSPMSRM

The conventional DSPM takes an SRM, cuts its back iron to place PMs. PMs create a rotating field as a result of varying reluctance. Unlike conventional PM machines where PMs attached to the rotor mechanical rotate resulting in a varying field and almost no saliency, the DSPM achieves this through its stationary magnets and variation in saliency. The resulting machine is one with higher power density that can extract torque from the interaction between PMs and phase current as well as torque from variation of reluctance when a phase is excited. The new PM structure is shown in Fig. 3.1 and a conventional DSPM is shown in Fig. 1.4.

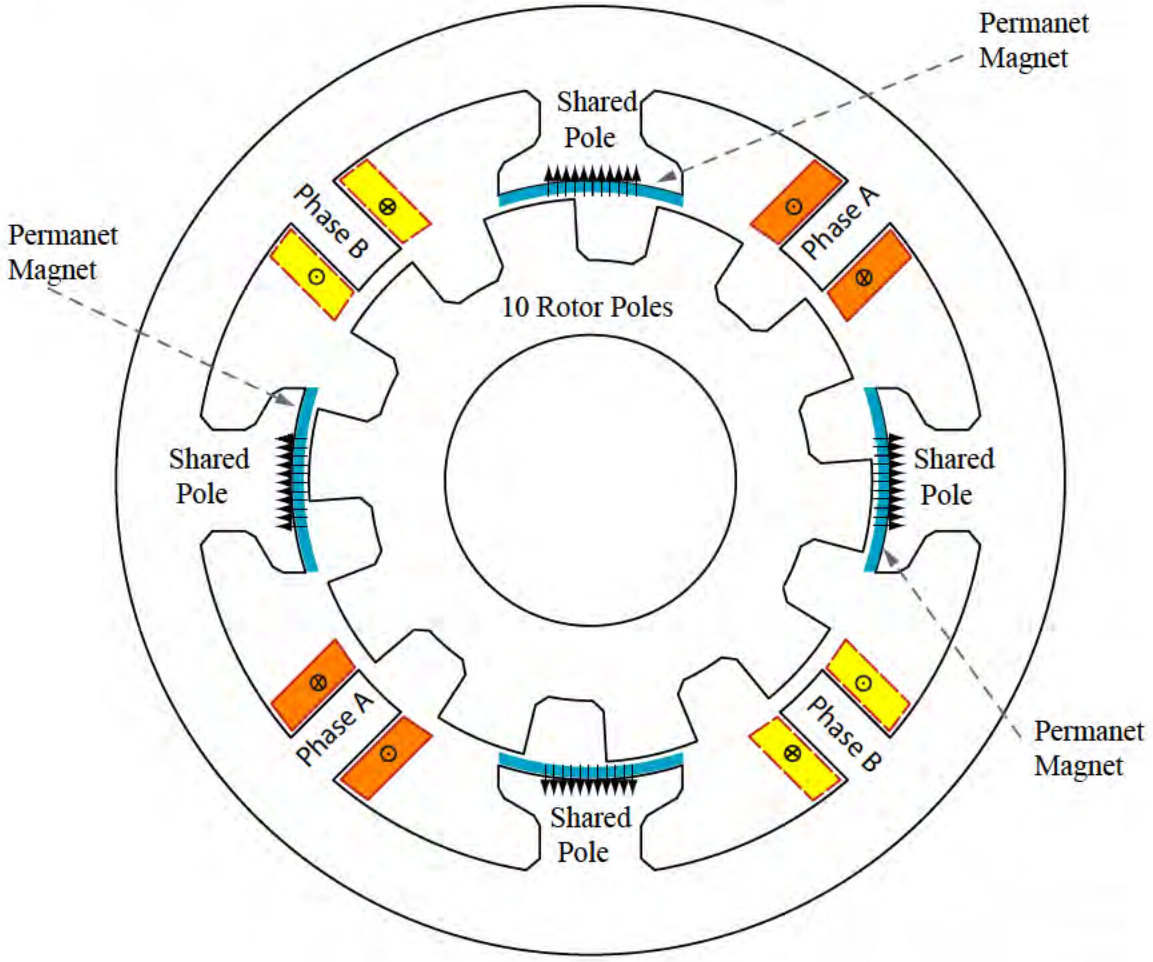

Figure 3.1: Novel DSPMSRM with monolithic structure with PMs on the shared pole.

The new DSPMSRM differs from conventional DSPMs and 4ecore SRM in the following ways:

- The new PM motor has a monolithic structure and does to need to break the back-iron in order to insert magnets. This feature would make this type of machine more attractive for manufacturing compared to segmental DSPMs.
- PMs are placed directly in the air gap of the machine instead of locations of the back-iron.
- Since unipolar excitation is used, the magnet does not face opposing MMF excitation, which may result in demagnetization, in case of a fault. Even under a winding fault, current will remain unipolar, hence the magnet‘s field will only be coupled with an MMF in the same direction.
- Since the common pole air gap does not have variation of reluctance, the majority of air gap torque is produced around wound stator poles.
- Cogging torque will be introduced in this 4-ecore SRM due to the introduction of PMs and asymmetric rotor pole profiling.
- Magnets are attached to the shared pole faces with the same magnetization direction, all focused with opposite polarity of the phase windings.
- Increasing the size or thickness of the magnets does not increase the power density of the machine and results in a significant decrease in reluctance torque.

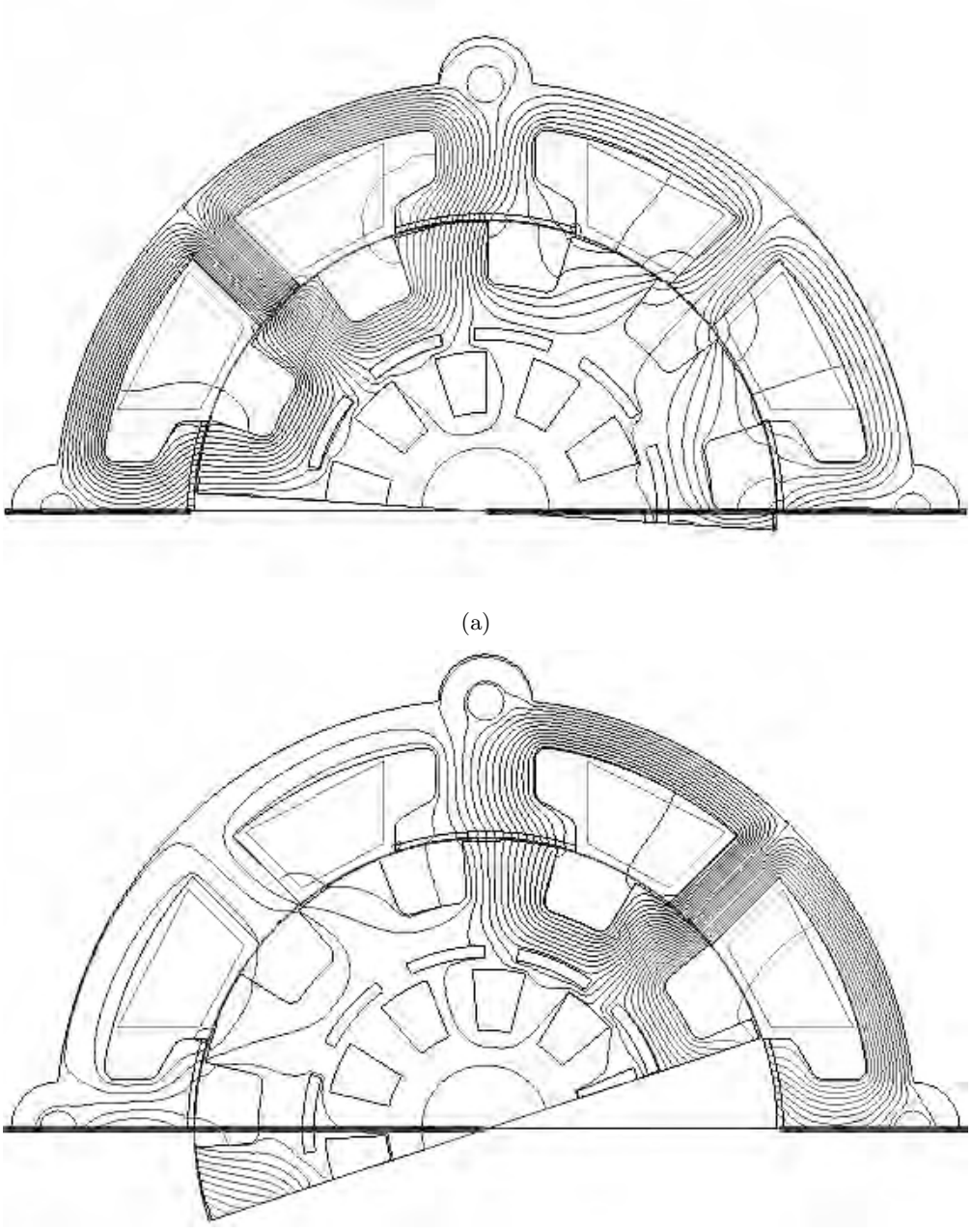

(a)

(b)

Figure 3.2: Magnetic flux path contours of the novel DSPMSRM for the (a) unaligned and (b) aligned positions with electric loading of 630 A/m.

3.1.1 Principle of operation

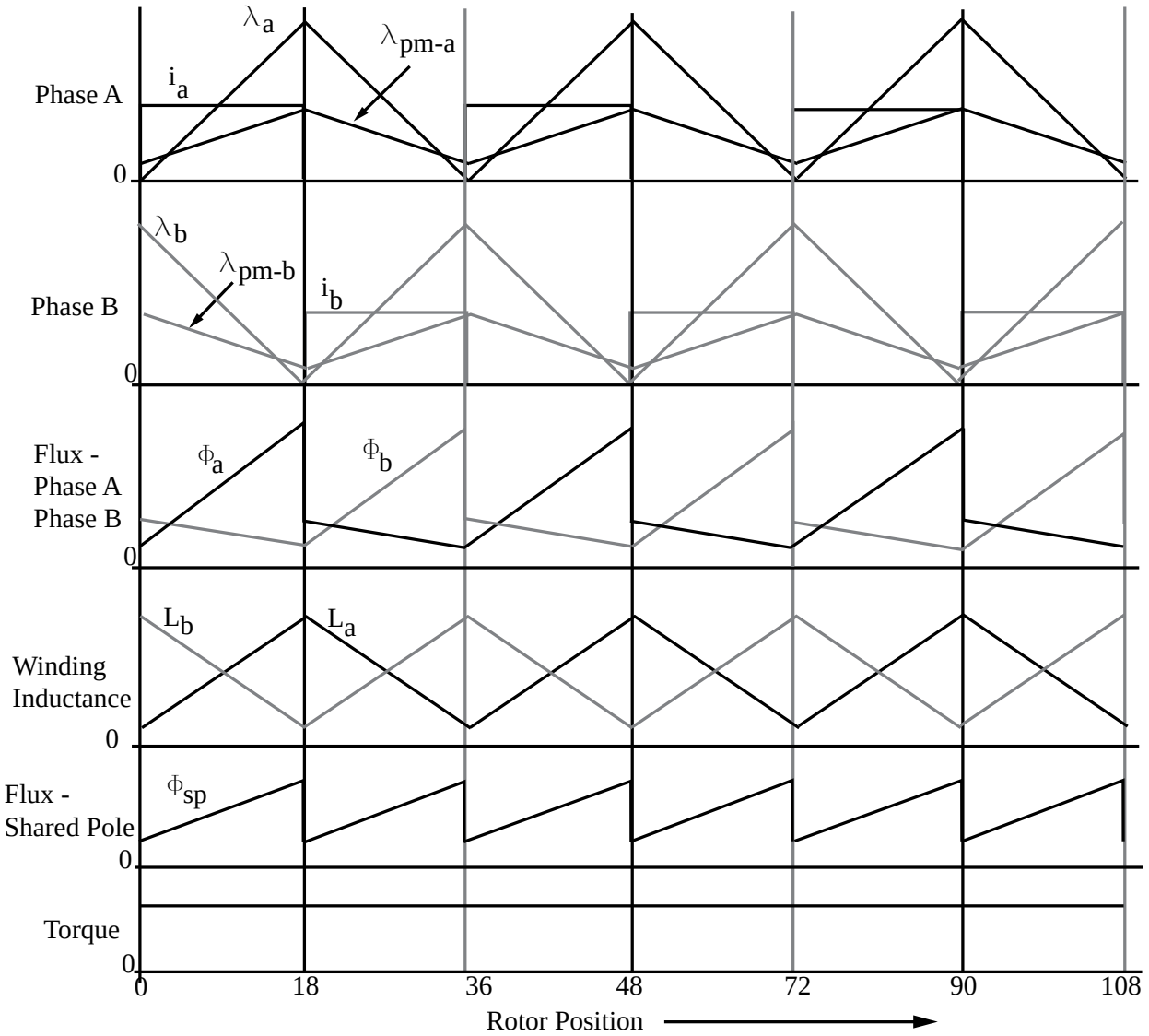

Figure 3.3: Principle of operation for the DSPMSRM. 0 degrees corresponds to the rotor position where the rotor being fully unaligned with phase A.

Fig. 3.3 shows ideal operation of the DSPMSRM with rectangular currents. Fig. 3.4 shows the operating principle of a 4ecore SRM. A properly designed DSPMSRM will have the same frequency of operation of the 4ecore before inserting magnets, for any rotor speed. Mutual inductance between the phase windings is assumed to be negligible hence a phase winding‘s flux does not link with itself through the leakage path of the other phase‘s wound pole. Phase A is excited at the position of

minimum inductance for its phase. The applied voltage results in increasing current in the phase windings and the addition of the winding‘s self flux and magnet flux. The magnet flux and winding flux combine to generate positive torque for that phase. Current is commutated before phase flux-linkage or inductance decreases. Once Phase A‘s current has been commutated, Phase B is excited for the period where its phase self inductance slope is positive. Similar to Phase A, current builds up in the phase winding and a positive torque is generated in machine. When its winding‘s self inductance is minimum, current is commutated before its inductance starts decreasing. The 4ecore SRM and DSPMSRM have the same fundamental frequency components for all their magnetic properties. Flux only flows through excited poles of the 4ecore SRM when a phase winding carries current. In the DSPMSRM, winding flux and PM flux combine to make total phase flux and when the winding is commutated, only PM flux decreases as reluctance of the unexcited phase pole‘s air gap decreases. Flux through a stator phase pole does not decay to zero at any time. Additional flux of the PM increases flux-linkage resulting in higher derivative of flux linkage for the same phase current in DSPMSRM. Torque generated by the DSPMSRM is greater than the 4ecore SRM for the same excitation current. It is apparent that this mode of operation only requires unipolar current in the DSPMSRM instead of bipolar current. This reduces converter costs since common two phase SRM drives which have lower cost than two phase full bridge inverters can be used.

λ_a	Flux-linkage from exciting Phase A‘s winding	i_a	Current in Phase A‘s winding
λ_b	Flux-linkage from exciting Phase B‘s winding	i_b	Current in Phase A‘s winding
λ_{pm-a}	PM flux-linkage induced in Phase A‘s winding	Φ_a	Flux through Phase A‘s stator pole
λ_{pm-b}	PM flux-linkage induced in Phase B‘s winding	Φ_a	Flux through Phase A‘s stator pole
λ_{pm-b}	PM flux-linkage induced in Phase B‘s winding	L_a	Phase A winding inductance
Φ_{sp}	Flux through the shared pole	L_b	Phase A winding inductance

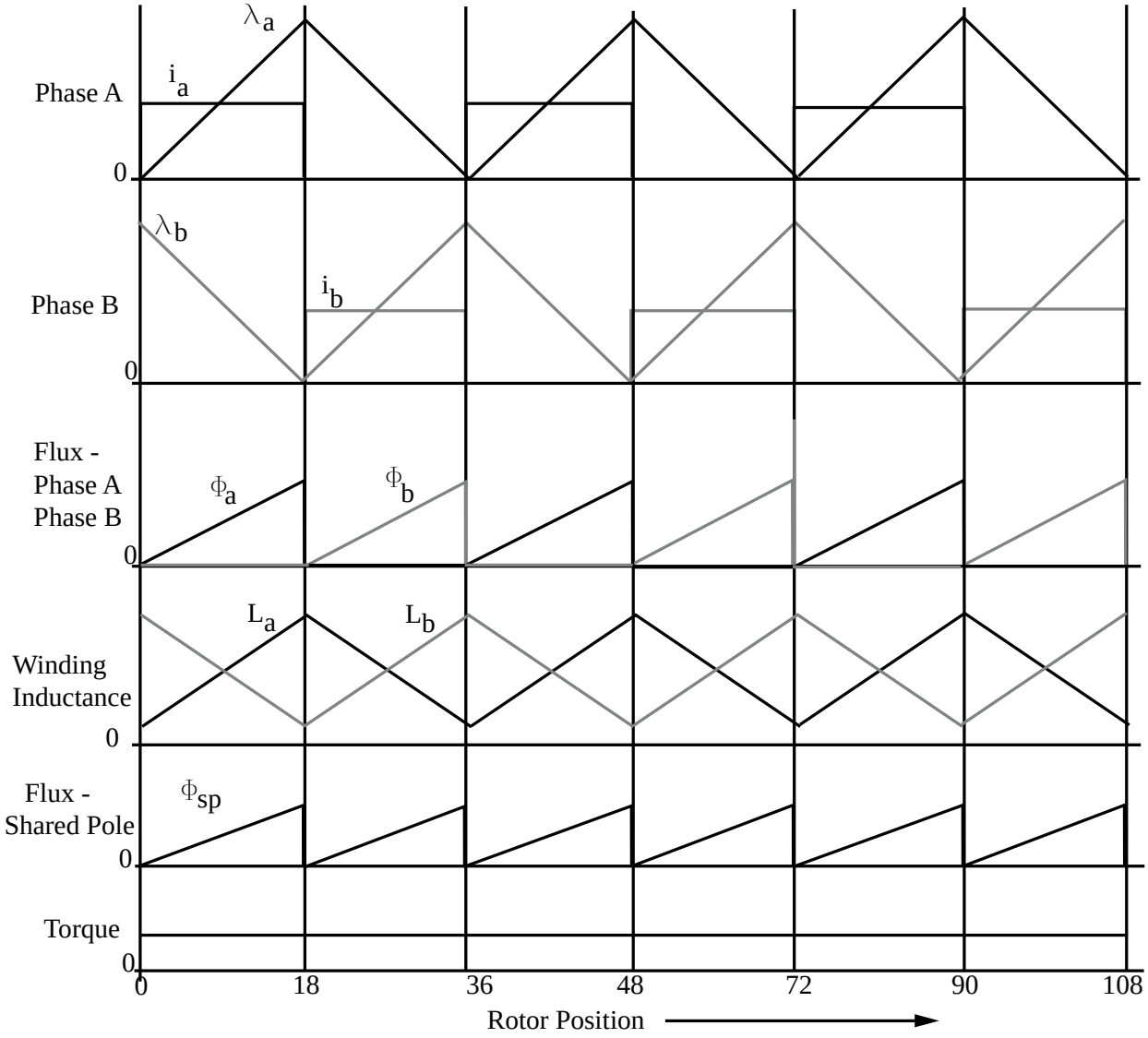

Figure 3.4: Principle of operation for the 4ecore SRM. 0 degrees corresponds to the rotor position where the rotor being fully unaligned with phase A.

3.2 Standard modeling of DSPMs[55]

This section will present the drawbacks of conventional DSPM modeling found in literature. The model is largely derived from [55] and uses many linear approximations which hold true in the case where the magnet torque dwarfs the reluctance torque. The voltage model of a DSPM assumes linear magnetic behavior and symmetric rotor pole faces. Voltage of an excited phase windings is written as,

$$v = Ri + \frac{d\lambda}{dt} \tag{3.1}$$

where v is the phase voltage, R is the phase resistance, i is phase current and λ is the phase flux-linkage. The phase flux linkage is the total flux linkage from the PM and phase current.

$$\lambda(\theta) = L(\theta)i + \lambda_{pm}(\theta) \tag{3.2}$$

where, θ is the rotor position, L is the phase‘s self inductance, and λ_{pm} is the flux linkage induced by the PM. A phase‘s self inductance at every rotor position and current is calculated by subtracting the magnet induced flux-linkage without phase current excitation from total phase-winding flux linkage with phase current excitation.

$$L(\theta, i) = \frac{\lambda - \lambda_{pm}}{i} \tag{3.3}$$

Electrical and mechanical power are obtained by multiplying current to both sides of (3.1).

$$\begin{aligned} P = v\ i &= i^2R + i\frac{d\lambda}{dt} \\ &= i^2R + Li\frac{di}{dt} + i^2\frac{dL}{dt} + i\frac{d\lambda_{pm}}{dt} \end{aligned} \tag{3.4}$$

Ignoring resistive losses, the stored magnetic energy and the output power are a function of mechanical energy, approximated by,

$$P_{out} \approx \omega_r \left(\frac{1}{2} i^2 \frac{\partial L}{\partial \theta} + i \frac{\partial \lambda_{pm}}{\partial \theta_r} \right) \tag{3.5}$$

The electromagnetic torque can be obtained from (3.5),

$$T = \frac{1}{2} i^2 \frac{\partial L}{\partial \theta} + i \frac{\partial \lambda_{pm}}{\partial \theta_r} \tag{3.6}$$

This widely used model is based on linear analysis and has the following drawbacks;

- The effect of cogging torque is neglected. The torque expression used in DSPMs, shown in (3.6) will result in zero torque, if the phase current is zero. Cogging torque is a result of PM flux in the machine and variable reluctance with respect to rotor position. In an SRM with a symmetric rotor, cogging torque is negligible and becomes significant when the rotor pole face is profiled for torque shaping. Hence, the model can be used in an average sense over one electrical cycle, and not for accurate instantaneous torque estimation.
- The effect of mutual inductance on the motor is neglected. In many SRMs, the effect of mutual inductance is low, by design. During operation, motor windings are switched where only one phase carries current at a time. In this operating mode, mutual inductance is zero.
- The effect of magnetic saturation is neglected. Magnet induced flux linkage estimated with zero current is not equal to magnet induced flux linkage when the winding current is large, causing the reluctance of the iron to change significantly.

$$\lambda_{pm}|_{i=0} \neq \lambda_{pm}|_{i \neq 0} \tag{3.7}$$

3.3 Non-linear model of the DSPMSRMs

The electro-mechanical model of the SRM will be derived from the principle of virtual work. In general, SRM models ignore mutual inductance, since SRM phases are generally designed to be magnetically isolated. In the non-linear model derivation presented in this section, the effect of mutual inductance will be incorporated into the model. Due to computational complexity, core-loss will be neglected from the model.

The fundamental electrical model of a two phase DSPMSRM is,

$$\begin{bmatrix} v_a \\ v_b \end{bmatrix} = \begin{bmatrix} R & 0 \\ 0 & R \end{bmatrix} \begin{bmatrix} i_a \\ i_b \end{bmatrix} + p \begin{bmatrix} \lambda_a \\ \lambda_b \end{bmatrix} \tag{3.8}$$

where, subscripts a, b denote the two motor phases A and B, respectively. Symbols v_a and v_b are the instantaneous voltages applied by the power converter to phases A and B respectively, R is the phase resistance, i_a and i_b are the instantaneous phase currents for both phases, λ_a and λ_b are the instantaneous flux-linkages of phases A and B, respectively and p is the time-derivative operator.

Electromagnetic torque in a motor can be expressed in terms of the incremental change in coenergy with respect to a incremental change in rotor position [37].

$$T = \frac{\partial W'_f}{\partial \theta} = \frac{1}{2}\mathbf{i}^T \frac{\partial \mathbf{L}}{\partial \theta}\mathbf{i} \tag{3.9}$$

where $\delta W'_f$ is the incremental change in coenergy which is equal to the armature reaction field energy. Equation (3.10) assumes linear magnetic characteristics. With linear magnetization characteristics the coenergy of the DSPMSRM is equal to its armature reaction stored magnetic energy. Hence,

$$W'_f = \frac{1}{2}\mathbf{i}^T \mathbf{L}\mathbf{i} \tag{3.10}$$

The phase current vector, $\mathbf{i}$, is of the form:

$$\mathbf{i} = \begin{bmatrix} i_a \\ i_b \\ i_{pm} \end{bmatrix} \tag{3.11}$$

and the inductance matrix, $\mathbf{L}$, is of the form:

$$L = \begin{bmatrix} L_{aa} & L_{ab} & L_{a-pm} \\ L_{ba} & L_{bb} & L_{b-pma} \\ L_{pm-a} & L_{pm-b} & L_{pm} \end{bmatrix} \tag{3.12}$$

Due to reciprocity, the following hold:

$$L_{ab} = L_{ba}, \qquad L_{a-pm} = L_{pm-a} \qquad L_{b-pm} = L_{pm-b} \tag{3.13}$$

L_{aa} and L_{bb} are the self inductances of phases A and B, respectively, L_{ab} and L_{ba} are the mutual inductances of phase A w.r.t. to phase B and phase B w.r.t. to phase A, respectively. The magnet in the DSPMSRM is modeled as a fictitious winding having one turn. The fictitious current due to the PM is expressed as,

$$i_{pm} = H_c \cdot l_{pm} = B_r \cdot A_{pm} \cdot R_{pm} \tag{3.14}$$

where H_c is the coercive force of the PM, A_{pm} is axial cross section of the PM, R_{pm} is the reluctance of the PM and l_{pm} is the height or radial thickness of the PM. Therefore L_{pm} is the fictional inductance of the PM expressed as a winding with one turn.

L_{pm-a}, L_{pm-a}, L_{a-pm} and L_{b-pm} are mutual inductance between the fictitious winding and phase A, fictitious winding and phase B, phase A and fictitious winding, and phase b and the fictitious winding, respectively.

Electromagnetic torque or air gap torque developed by the motor when one or both phase windings are excited can be derived by the principle of virtual work. According to the principle of virtual work, an infinitesimal change in input electrical energy will result in an infinitesimal change in the armature reaction field energy and mechanical energy.

The instantaneous machine torque as a function as currents and inductance is obtained as,

$$T = \left\{ \frac{1}{2} \left(i_a^2 \frac{\partial L_{aa}}{\partial \theta} + i_b^2 \frac{\partial L_{bb}}{\partial \theta} \right) + i_a \cdot i_b \frac{\partial L_{ab}}{\partial \theta} \right\} ... \\ + \left[\frac{1}{2} \left(i_a \cdot i_{pm} \frac{\partial L_{pm-a}}{\partial \theta} + i_b \cdot i_{pm} \frac{\partial L_{pm-b}}{\partial \theta} \right) \right] ... \\ + \frac{1}{2} i_{pm}^2 \frac{\partial L_{pm}}{\partial \theta} \tag{3.15}$$

The first term in curly braces is reluctance torque which arises from variation of self and mutual inductance of the motor phases. The second term in square brackets is due to the interaction of the magnetic field from the PMs and the stator windings. The last term on the third line is cogging torque. Cogging torque is present due to variations of self inductance of the phase windings corresponding to the PM field. Cogging torque is present in all PM machines where variation of reluctance between phases is not symmetric, even if phase windings are not excited. SRMs are usually designed to operate with very low mutual inductance between phases. In that case, the electromagnetic torque in one phase can be expressed as,

$$T = \frac{1}{2} \left(i_a^2 \frac{\partial L_{aa}}{\partial \theta} + i_b^2 \frac{\partial L_{bb}}{\partial \theta} \right) ... \\ + \left[\frac{1}{2} \left(i_a \cdot i_{pm} \frac{\partial L_{pm-a}}{\partial \theta} + i_b \cdot i_{pm} \frac{\partial L_{pm-b}}{\partial \theta} \right) \right] ... \\ + \frac{1}{2} i_{pm}^2 \frac{\partial L_{pm}}{\partial \theta} \tag{3.16}$$

Since flux-linkage can be written as the product of phase current and inductance, phase winding flux-linkages in equation (3.8) can be written as,

$$\lambda_a = L_{aa}\, i_a + L_{ab}\, i_b + L_{pm-a}\, i_{pm} \tag{3.17}$$

$$\lambda_b = L_{bb}\, i_b + L_{ab}\, i_a + L_{pm-b}\, i_{pm} \tag{3.18}$$

The electrical dynamics shown in equation (3.8) can be re-written by substituting equations (3.17) and (3.18) in equation (3.8). The electrical dynamics for phase A of the DSPMSRM, ignoring core and PM losses, can be written as,

$$
\begin{aligned}
v_a &= R\, i_a + i_a \frac{dL_{aa}}{dt} + L_{aa}\frac{di_a}{dt} + i_b \frac{dL_{ab}}{dt} + L_{ab}\frac{di_b}{dt} + i_{pm}\frac{dL_{pm-a}}{dt} + L_{pm-a}\frac{di_{pm}}{dt} \\
&= R\, i_a + i_a \frac{dL_{aa}}{dt} + L_{aa}\frac{di_a}{dt} + i_b \frac{dL_{ab}}{dt} + L_{ab}\frac{di_b}{dt} + \frac{\lambda_{pm-a}}{dt}
\end{aligned} \tag{3.19}
$$

where

$$
\frac{\lambda_{pm-a}}{dt} = i_{pm}\frac{dL_{pm-a}}{dt} + L_{pm-a}\frac{di_{pm}}{dt}
$$

Similarly the electrical dynamics for phase B is written as,

$$
\begin{aligned}
v_b &= R\, i_b + i_b \frac{dL_{bb}}{dt} + L_{bb}\frac{di_b}{dt} + i_a \frac{dL_{ab}}{dt} + L_{ab}\frac{di_a}{dt} + i_{pm}\frac{dL_{pm-b}}{dt} + L_{pm-b}\frac{di_{pm}}{dt} \\
&= R\, i_b + i_b \frac{dL_{bb}}{dt} + L_{bb}\frac{di_b}{dt} + i_a \frac{dL_{ab}}{dt} + L_{ab}\frac{di_a}{dt} + \frac{\lambda_{pm-b}}{dt}
\end{aligned} \tag{3.20}
$$

where

$$
\frac{\lambda_{pm-b}}{dt} = i_{pm}\frac{dL_{pm-b}}{dt} + L_{pm-b}\frac{di_{pm}}{dt}
$$

The electric model shown in equations (3.15), (3.19) and (3.20) include the cogging torque from the motor and mutual inductances. Simplification of the complete model is useful to facilitate rapid simulation of the motor performance characteristics. Since the proposed DSPMSRM is to be operated as an SRM, mutual inductance between phase windings can be assumed to be negligible. By the principle of conservation of energy, the average work done by cogging torque in one electrical cycle is zero. If these assumptions are made, the conventional linear model presented in Section 3.2 can be used.

3.4 Design Procedure for DSPMSRM

In order to successfully design a DSPMSRM, a power equation that is composed of machine dimensions, electric and magnetic conditions such as peak flux density and power supply limitations

is invaluable. A rapid estimation of power output for a machine using equations that are familiar to machine designers will aid in the rapid sizing of the machine for a certain application. A flux-linkage approach is used to derive the sizing equations for the DSPMSRM. Flux weakening mode of operation where the phase current polarity is reversed, leading to opposing the magnets MMF is avoided. The wound rotor poles should be excited to have constructive addition of MMF with the PM. Since DSPMs are generally operated with bipolar current, reluctance torque and armature reaction torque are additive in half the electrical cycle and subtractive in the negative cycle. Reluctance torque is proportional to the square of the current and derivative of flux-linkage. Hence, reversing current polarity will not change the reluctance torque vector‘s direction. Armature reaction torque is proportional to current and derivative of flux-linkage, and reversing the current in the negative flux-linkage derivative region will reverse the torque vector, so as to always generate unidirectional torque. The design procedure outlined in this section will show the design procedure to drive the SRM with positive currents. Let l_g be the height of the air gap between the rotor

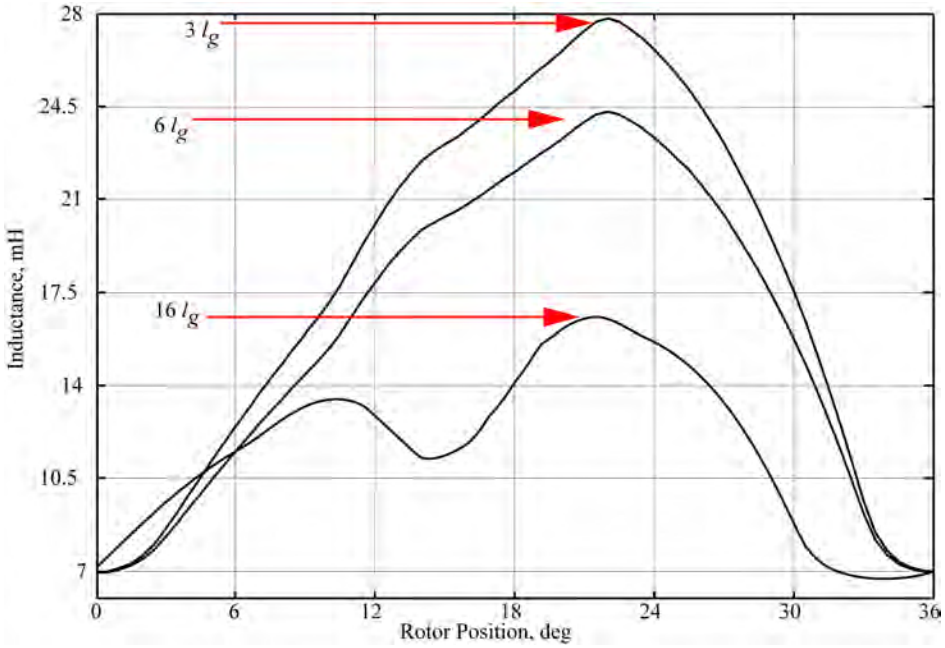

Figure 3.5: Variation of phase self inductance as a function of air gap length and magnet thickness.

and wound stator pole. In order to have majority of the flux generated by the wound stator pole return through the shared pole, the total length of the PM and its facing air gap should be less than $8 \cdot l_g$. Fig. 3.5 shows the variation in phase inductance with varying thickness of the magnets. A thick magnet would force the phase winding‘s flux to take a leakage path through the second‘s

phases pole. The leakge path through the second phase‘s pole is present because the reluctance of the leakage path is lower than returning to the PM whose permablity is close to air. The mutual inductance between the phases would also increase and the magnitude of reluctance torque would be reduced significantly.

The air gap power of the SRM at the desired rated speed is,

$$P_{out} = \overline{T} \cdot \omega_m \tag{3.21}$$

where $\overline{T}$ is the average torque per electrical cycle.

Average torque can be expressed as a function of peak phase current and flux-linkage at that current level,

$$\overline{T} = \frac{1}{2} i \frac{\lambda_{max} - \lambda_{min}}{d\theta} = i \frac{\lambda_{max} - \lambda_{min}}{\beta_s} \tag{3.22}$$

Expressing the maximum flux-linkage in terms of the peak flux density in the wound stator pole,

$$\lambda_{max} = B \cdot A_{sp} \cdot T_{ph} = B \cdot \frac{D}{2} \cdot L \cdot \beta_s \cdot T_{ph} \tag{3.23}$$

where B is the average flux density in the main stator pole at the aligned position, A_{sp} is the area of the wound stator pole, D is diameter of the air gap , β_s is the stator pole arc and L is the stack height.

Define the constant:

$$\sigma_s = \frac{\lambda_{min}}{\lambda_{max}} \tag{3.24}$$

$$P_{out} = \frac{1}{2} i^2 \frac{\lambda_{max} - \lambda_{min}}{d\theta} = \frac{1}{2} i^2 \ \ \frac{\lambda_{max} - \lambda_{min}}{\beta_s} \tag{3.25}$$

The output power can be rewritten as:

Let k_e be the efficiency of the DSPMSRM and k_d be duty cycle where the SRM phase is producing positive torque.

Combining, (3.23), (3.24) and (3.25), the output power is given by,

$$P_{out} = k_e \, k_d \, \frac{\pi^2}{120}(1 - \sigma_s) B \, A_s \, D^2 \, L \, \omega_{rpm} \tag{3.26}$$

where ω_{rpm} is machine speed in rev/min and A_s is the electric loading. Equation (3.26) is the usual form of a output power equations for electric machines. During the initial design, values of specific loading, peak flux density and operating speed are defined or are specified constants. The ratio (3.24) can be chosen based on the required average torque. Therefore, the power of the SRM is proportional to the volume enclosed by the air gap or bore of the machine, D^2L. The bore diameter for a power level can be estimated by rearranging (3.26),

$$D = \sqrt{\frac{\pi \, D}{k_e \, k_d \, \frac{\pi^2}{120}(1 - \sigma_s) B \, A_s \, L \, \omega_{rpm}}} \tag{3.27}$$

For many applications the outer diameter of the machine is limited, hence the stack length of the machine can be estimated by rearranging the power equation.

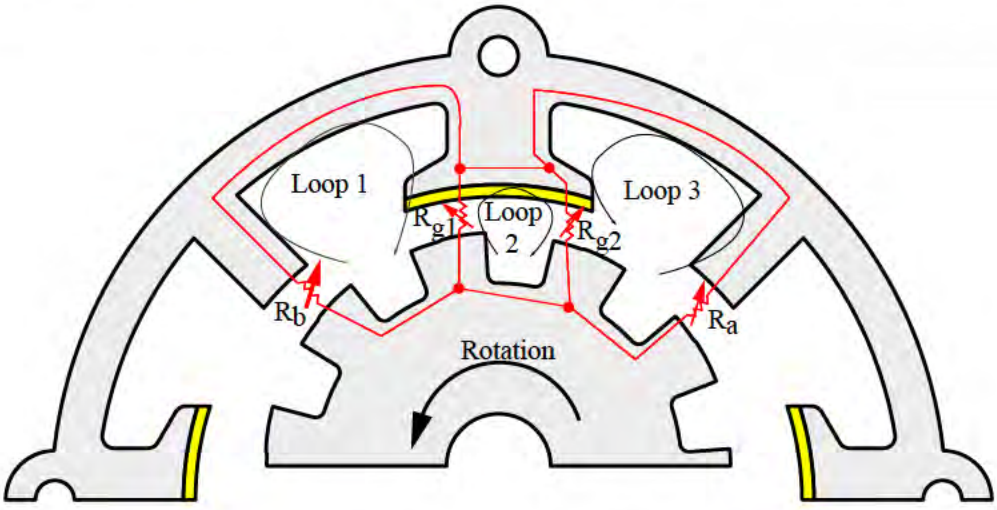

Figure 3.6: Magnetic equivalent circuit for a portion of the SRM.

The area of the wound stator pole face is given as:

$$A_{sp} = \frac{D\ L\ \beta_s}{2} \tag{3.28}$$

The arc of the shared pole is always equal to one rotor pole pitch.

$$\theta_{cp} = \frac{2\pi}{10} \tag{3.29}$$

Fig. 3.6 shows the magnetic equivalent circuit (MEC) for one quarter of the machine. References [53, 52] showed the variation of reluctance of the shared pole w.r.t to rotor position is zero. Also current enclosed by Amperean Loop 2 is also zero since there is a PM attached to the shared pole. Since the reluctance of Loop 2 is constant, it will be neglected in the analysis. Work done by cogging in one electrical cycle is zero and its effect will be ignored. Since the machine phases are excited in sequence, the effect of Loop 1 will be ignored. Loop 3 will be used to examine the power generated by one phase at a time. Due to magnetic symmetry of the structure of one phase, every Amperean loop in a comprehensive magnetic circuit does not need to be analyzed. Assume, R_a and R_b are the reluctances of the air gap around the pole for Phase A and B, respectively. R_{g1} and R_{g2} are the reluctances of the air gap plus the PM around the two overlapping common poles.

Considering magnetic linearity, the flux from the PM constructively adds with the windings flux, the total flux going through the wound stator pole is

$$\Phi = B\ A_{sp} \tag{3.30}$$

Only half the flux through the wound stator pole goes through each shared pole, hence flux density in the air gap around the shared stator pole and over lapping portion of the magnet is,

$$B_{cp} = \frac{1}{2} B\ \frac{A_{sp}}{A_{cp}} = \frac{1}{2} B\ \frac{\beta_s}{\beta_r} \tag{3.31}$$

where β_r is the rotor pole arc. Neodymium magnets have a linear demagnetization characteristic and are chosen as the PM material for the design. The demagnetization characteristics for the magnet can be expressed as:

$$H_m = H_c \left(1 - \frac{B_m}{B_r}\right) \tag{3.32}$$

where B_m is the flux density of the magnet surface overlapped with the rotor pole, which is equal to the flux density in the overlapped region of the air gap around the shared pole. After choosing a specific PM with H_c and B_r, the height of the PM in the air gap can be estimated as:

$$h_{pm} = \frac{B_{cp} \cdot 2\ l_g}{\mu_o H_c \left(1 - \frac{B_m}{B_r}\right)} \tag{3.33}$$

The arc of the PM is equal to the arc shared pole. Electric loading for a machine without PMs and two phases is usually expressed as,

$$A'_s = \frac{T_{ph}\ i}{\frac{\pi}{2} D} \tag{3.34}$$

Modifying (3.34) for the DSPMSRM to incorporate PMs,

$$A_s = \frac{T_{ph}\ i + 2H_c h_{pm}}{\frac{\pi}{2} D} \tag{3.35}$$

For a peak phase-current the number of winding turns per phase can be obtained:

$$T_{ph} = \frac{\pi\ D\ A_s}{2} - 2H_c h_{pm} \tag{3.36}$$

The thickness of the stator yoke is half the stator pole width,

$$h_{sy} = \frac{D}{2}\frac{\beta_s}{2} \tag{3.37}$$

The stator pole height,h_s can be estimated from required the winding area. Fig. 3.7 shows the dimensions of the shared pole that can be varied to accommodate a winding, depending on

the maximum desired current density in the wire. The width of the shared pole core, w_{cps}, can be varied from a maximum of $\frac{\pi D}{10}$, to a minimum $1.5w_{sy}$ since the shared pole may carry flux from both phases depending on the control strategy implemented. A reasonable estimate for the minimum height of the shared pole slot is $h_{sps} = 5(l_g + h_{pm})$ to prevent flux-leakage and saturation at the tips of the shared pole. The height of the stator pole can be reduced by modifying the width of the shared pole core, until the winding fits in the slot. The outer diameter of the DSPMSRM can then be expressed as:

$$D_o = D + 2\left(h_s + h_{sy}\right) \tag{3.38}$$

The height of the rotor yoke is equal to the stator yoke, h_{sy}. The height of the rotor pole depends on the constrained shaft size and it is normal to choose a rotor pole height that is equal to or greater than the stator pole height, to reduce the weight of the rotor.

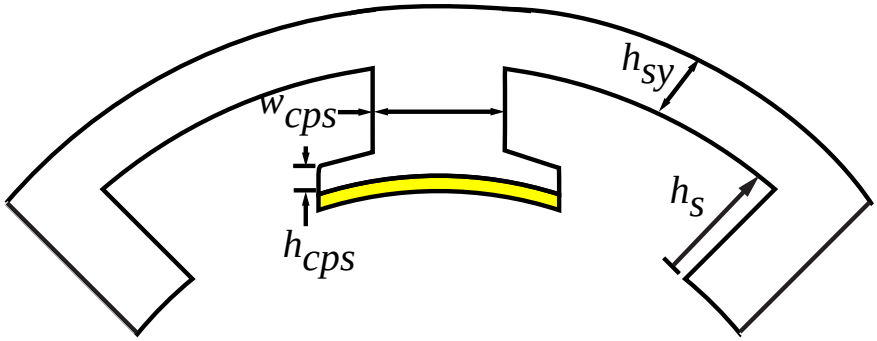

Figure 3.7: Design of the shared pole to accommodate a winding.

Average torque of the DSPMSRM, neglecting resistive loss can be rewritten in terms of flux linkage,

$$\begin{aligned}
\overline{T} &= \frac{1}{2} i^2 \frac{dL}{d\theta} + i\frac{d\lambda_{pm}}{d\theta} && (3.39)\\
&= \frac{1}{2} i \frac{d\lambda_i}{d\theta} + i\frac{d\lambda_{pm}}{d\theta} \\
&= T_{ph}\, i \left[\left(\frac{1}{2}\frac{\phi_i}{d\theta}\right) + \left(\frac{d\phi_{pm}}{d\theta}\right)\right] \\
&= T_{ph}\, i \left[\left(\frac{1}{2} T_{ph}\, i \frac{dP}{d\theta}\right) + \left(2H_c h_{pm}\frac{dP}{d\theta}\right)\right] && (3.40)
\end{aligned}$$

where P is the permeance of air gap. The term on the left inside the square brackets is torque generated by reluctance only and the term on the right is the torque contributed by armature reaction. The ratio of reluctance torque to magnet torque for various current levels, below magnetic saturation is,

$$\frac{T_{\text{reluctance}}}{T_{\text{pm}}} = \frac{\frac{1}{2}T_{ph}\ i}{2H_c h_{pm}} = \frac{T_{ph}\ i}{4H_c h_{pm}} \tag{3.41}$$

The average in permeance over one electrical cycle, if there is no overlap between the wound stator pole and rotor pole in the fully unaligned position, is given by,

$$\frac{dP}{d\theta} \cong \frac{10}{\pi} \cdot \mu_o L \left\{ \left[\frac{l_g}{\frac{1}{2}\frac{D}{2}\left(\frac{\pi}{4} - \frac{\pi}{10} - \frac{\beta_s}{2} - \beta_r\right)} \right] - \left[\frac{\frac{D}{2}\beta_s}{l_g} \right] \right\} \tag{3.42}$$

The change in permeance over one electrical cycle, if there is overlap between the wound stator pole and rotor pole in the fully unaligned position, is given by,

$$\frac{dP}{d\theta} \cong \frac{10}{\pi} \cdot \mu_o L \left\{ \left[\frac{\frac{1}{2}\frac{D}{2}\left(\beta_s - \beta_r\right)}{l_g} \right] - \left[\frac{\frac{D}{2}\beta_s}{l_g} \right] \right\} \tag{3.43}$$

Equations (3.41), (3.42) and (3.43) are significant to understand the benefit of attaching a PM to the shared pole. Consider Fig. 3.8(a), from finite element analysis, which shows the flux-linkage characteristics evaluated for a 4ecore SRM without a PM and the same 4ecore SRM with a PM attached to its shared pole. The lower solid trace is the flux-linkage for various currents at the unaligned position for the 4ecore SRM. The upper trace is the flux-linkage at the fully aligned position. The dotted traces are for the 4ecore with PMs. The unaligned position trace for the DSPMSRM is offset by λ_{pm}^{u}. The flux-linkage characteristics on the right shows the same flux linkage characteristics after removing the offset at the unaligned position to compare the areas of the two flux-linkage characteristics. The area enclosed by flux-linkage characteristics for any machine signifies their output mechanical work. The figure on the right shows the aligned flux-linkage of the DSPMSRM is offset from the conventional SRM by a constant amount until magnetic saturation sets. In Fig. 3.8(b), work done by reluctance only is shaded differently from the work

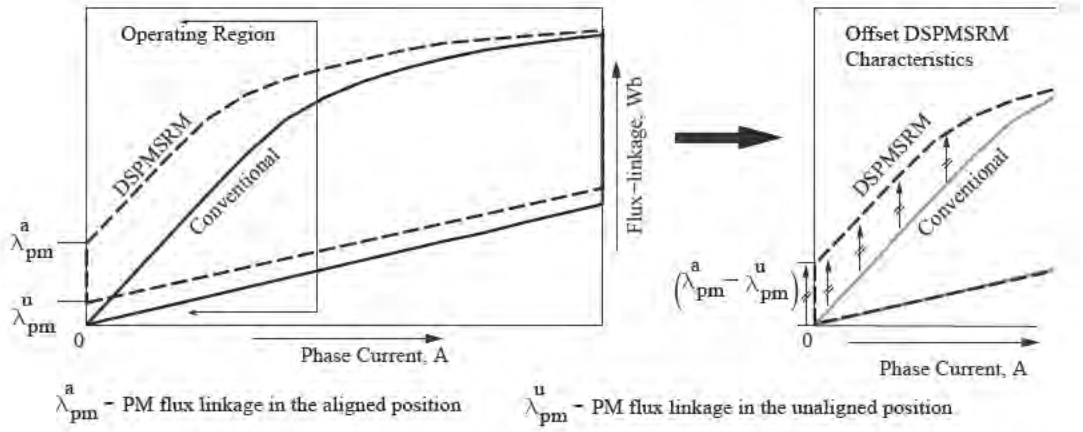

(a)

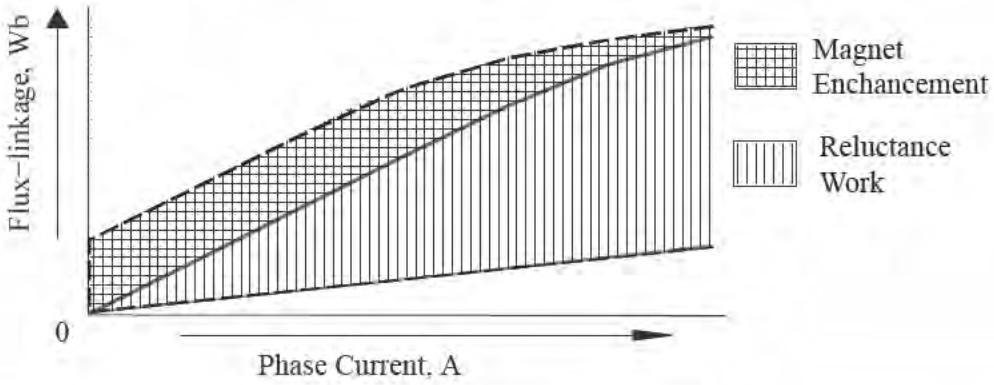

(b) DSPM

Figure 3.8: Graphical representation of the work enhancement of the DSPMSRM. (a) Overlay of the SRM and DSPMSRM flux-linkage characteristics (b) Work enhancement in the DSPMSRM

enhancement produced by adding PMs. The area enclosed by the PM enhancement is rectangular as is normal in PM machines, while the area enclosed by reluctance contribution is triangular. If a magnet with a higher twice as much coercive force is used, the rectangular PM enhancement area would be greater. The phase winding current required to operate at a certain power level would be reduced due to the magnet, which can be considered as a current source.

Chapter 4

Comparison of the DSPMSRM and SRM

Comparing the enhancement of the novel machine to its predecessor is be presented in the following sections of this chapter. An already available optimized 4ecore SRM is taken as a baseline motor.

The frame size of the existing 4ecore motor is maintained in the novel DSPMSRM. Inner and outer radii of the stator and rotor are also kept constant. The stack length of the DSPMSRM to the 4ecore SRM to show the enhancement in power density. In the second case, stack length of the DSPMSRM is modified to decrease the peak output power of the SRM, and match its output capability to that of the 4ecore SRM.

A PM with linear demagnetizing characteristics is chosen for its high energy density. A rare-earth, neodymium-iron-boron PM (NdFeB), grade N42 is incorporated into the shared pole of the 4ecore SRM. The properties of the magnet are:

- Relative permeability, $\mu_r = 1.099$
- Coercivity, $H_c = -9.5 \cdot 10^5$ A/m
- Remanence, $B_r = 1.31$ T
- Magnet thickness, 1 mm

4.1 Cogging torque

From Fig. 3.6, (3.19) and (3.20) cogging torque can be expressed as,

$$T_{cog} \cong -\frac{1}{2} i_{pm}^2 \frac{dL}{d\theta} = \Phi_{pm}^2 \frac{dR}{d\theta} \tag{4.1}$$

The term $\frac{dR}{d\theta} = 0$ when fringing fields in the air gap are neglected. Due to the presence of minor asymmetric variations in the distribution of the magnetic field in the air gap when the rotor rotates, cogging torque is developed. Ideally, when a rotor pole approaches a stator pole of one phase, the change in reluctance is equal to the rotor pole leaving the stator pole of the second phase, making the change in reluctance zero as the rotor rotates. If asymmetry is introduced in the rotor pole faces the rotor pole this effect can be amplified and extracted for self-starting. Asymmetry on the rotor pole faces introduces overlap on the positive torque profiles of both phases, and the net change in reluctance of both phases will not be zero when the inductance characteristics of both phases have the same slope. Hence the effect of fringing and asymmetry leads to increase in the cogging torque.

Due to effects of magnetic saturation in the magnetic characteristics of the iron, electromagnetic torque is calculated using the Maxwell stress tensor on finite elements in the air gap between the stator and rotor. Leakage flux which does not couple with the rotor, affects the magnetization characteristics of the phase windings, but does not affect generated electromagnetic torque. Air has linear magnetization characteristics and energy stored in the magnetic field of the air gap is equal to its coenergy.

Electromagnetic torque is obtained by integrating the tangential force from the Maxwell stress tensor over a circle in the air gap between the rotor and stator. The tensor expression shown in (2.20), rewritten for torque is

$$T = \frac{1}{\mu_o} \oint B_n B_t ds = \frac{r^2 L_z}{\mu_o} \int_0^{2\pi} B_n B_t d\theta \tag{4.2}$$

where r is the radius of the circle in the air gap and L_z is the stack or axial length of the machine. Since the tensor is evaluated in the air gap, all field coupling effects like cogging, PM

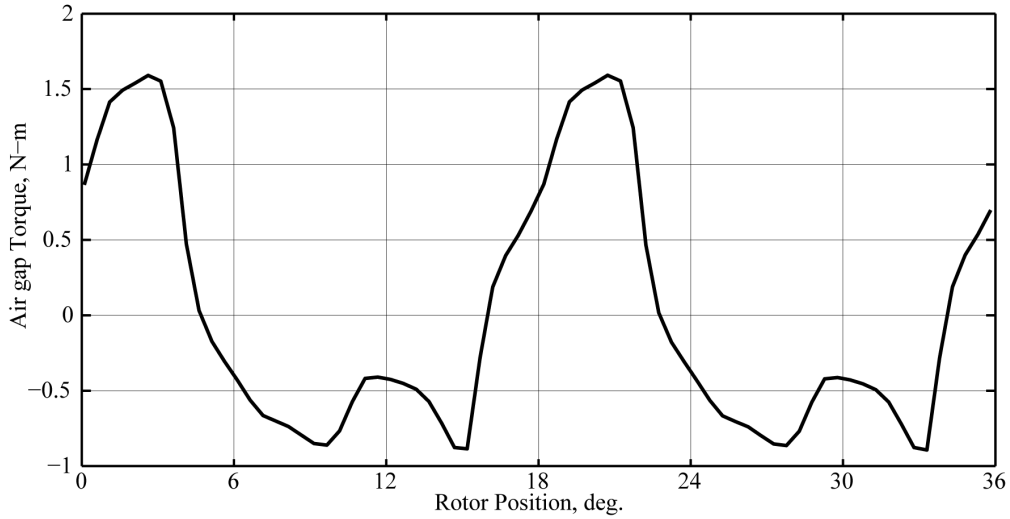

Figure 4.1: Cogging torque from DSPMSRM.

torque and reluctance torque are included. Cogging torque due for the novel DSPMSRM, is shown in Fig. 4.1. The cogging torque cycles twice per electrical period. One electrical cycle is equal to 36 mechanical degrees of rotation of the rotor. In SRMs, torque from phase winding excitation has the same period as the electrical cycle. Without current excitation in the DSPMSRM, the resultant torque that is the net of the torque that is generated around each wound pole which results in the cogging torque oscillating twice per electrical cycle.

4.2 Comparison of static torque profiles

Static torque profiles for the conventional 4ecore SRM and compared to the novel DSPMSRM. Fig. 4.2 shows the instantaneous torque w.r.t to rotor position and phase current. Table (4.1) shows the average torque versus current for both machines. Average positive torque for every current in one electrical cycle is calculated using the expression,

$$T_{avg}(i) = \frac{1}{2}\frac{1}{2\pi}\int_0^{2\pi} |T(\theta)|_{i=constant} \quad d\theta \tag{4.3}$$

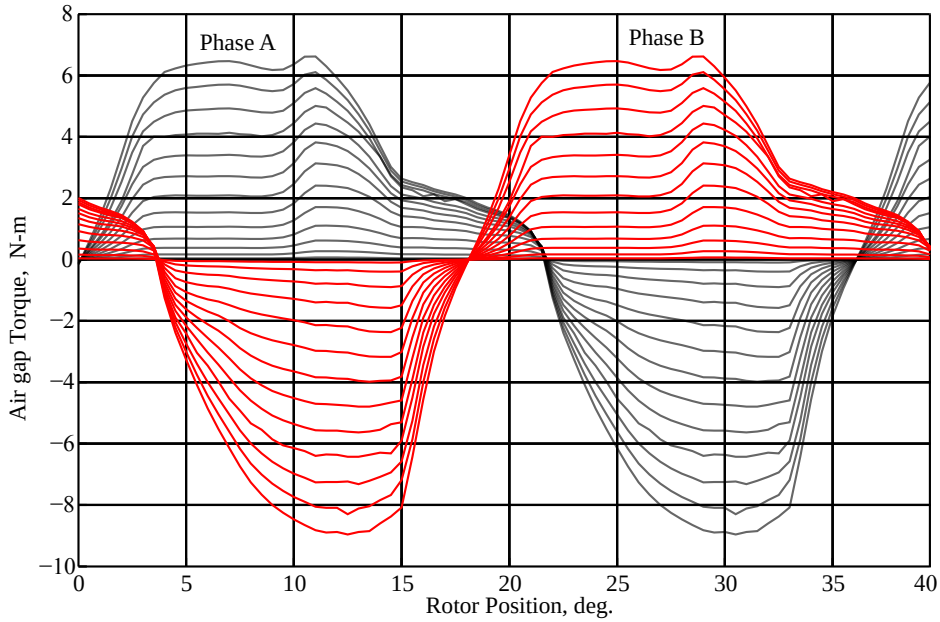

(a) Conventional 4-ecore SRM

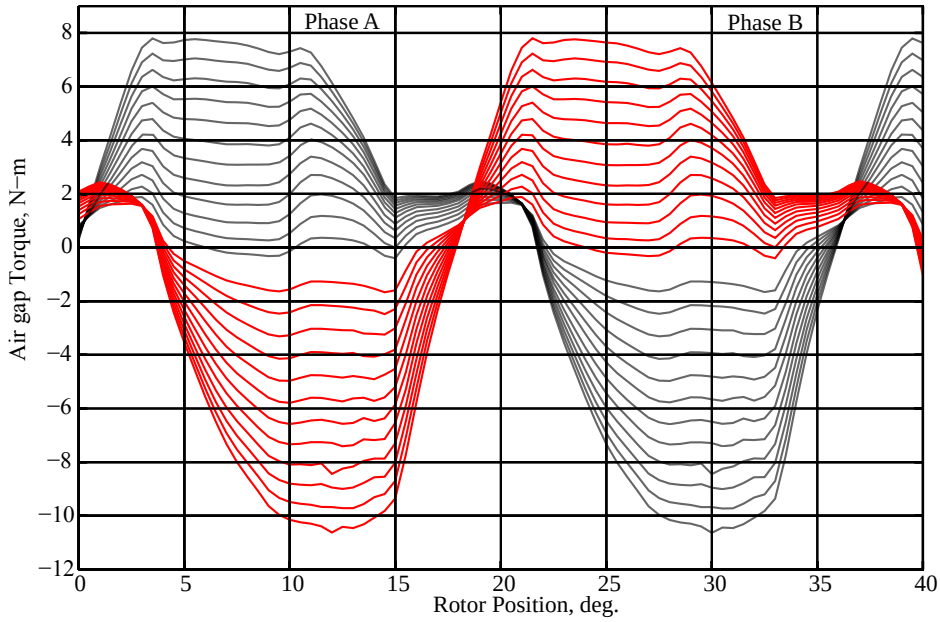

(b) Novel DSPMSRM

Figure 4.2: Electromagnetic torque of (a) conventional 4-ecore SRM and (b) novel DSPMSRM for phase currents from 0A to 13A in 1A increments for both phases.

Table 4.1: Average torque w.r.t phase current for the conventional and novel machine.

Phase Current, A	Conventional, N-m	Novel DSPMSRM,N-m	% Increase
1	0.04	0.8	1900
2	0.17	1.0	488.2
3	0.37	1.3	251.4
4	0.66	1.8	172.7
5	1.0	2.2	120.0
6	1.4	2.5	78.6
7	1.8	3.0	66.7
8	2.2	3.4	54.6
9	2.6	3.7	42.3
10	3.1	4.1	32.3
11	3.4	4.4	29.4
12	3.76	4.7	25.0
13	4.1	5.1	24.4

From results of the comparison of static average torque for constant current excitation, enhancement of novel DSPMSRM is apparent. The average torque at 1A phase current excitation is high due to the dominant effect of cogging torque in the machine. The torque profile around 1A has more than two zero crossings in one electrical cycle. In the 4ecore SRM average torque at low excitation currents (less than 2A) is negligible and torque only has two zero crossings per electrical cycle. At currents higher than 2A, DSPMSRM torque resembles a regular SRM, with only two zero crossings per electrical cycle. One of the key improvements, of this SRM is the enhancement of torque overlap between phases. Torque overlap between phases greater in the DSPMSRM mainly due to the effect of cogging at those rotor positions. Another important difference is the intersection of the torque profiles. In a conventional SRM, without PMs, the torque profiles intersect at the full aligned position. In the novel DSPMSRM, the torque profiles intersect at 1N-m. These results show the need to include cogging torque in the electromechanical model of the DSPMSRM.

Fig. 4.3 shows the contribution of reluctance torque in the DSPMSRM. Reluctance torque is estimated by setting the coercive force of the PM to zero which effectively disables its intrinsic field. Table 4.2 summaries the average torque contributed from reluctance and PMs w.r.t to phase current under single phase excitation. Torque contribution by the PM is estimated by subtracting the reluctance contribution from the average torque for the DSPMSRM, shown in Table 4.1 for each current level, respectively. Average reluctance torque increases with current level and is the dominant torque producing mechanism. Since the approximate positive torque period from reluctance contribution is the same as total torque contribution, the PM enhances the total torque production in the machine. The DSPMSRM‘s magnets enhance the reluctance torque by approximately 40% at the rated operating condition.

It should be noted that the ratio between pure reluctance torque and magnet torque can be varied by changing the a few key parameters in the machine. Increasing the number of winding turns will increase the MMF generated by the phase and overall higher reluctance torque for the same phase current excitation. Increasing the magnet‘s coercive force will increase the contribution of the magnet torque while keeping the reluctance torque roughly the same. Decreasing the thickness of the magnet will decrease the overall length of the air gap and enhance the reluctance torque significantly. SRMs have significantly smaller air gap than ac machines. The greater the thickness of the PM, the greater the length of the magnet and a significant drop in the contribution of

reluctance torque will occur. As discussed in Chapter 3, increasing the magnet thickness will result in the machines frequency of operation doubling and net zero reluctance torque which is the case in DSPMs with large magnets. It is preferred to have magnets with high energy product and thickness as small as possible, to enhance the variation in reluctance of the DSPMSRM. Due to manufacturing limitations that exist in today‘s market, manufacturing magnets with low dimensional tolerance and small thickness, less than 1mm, is not feasible on a large scale.

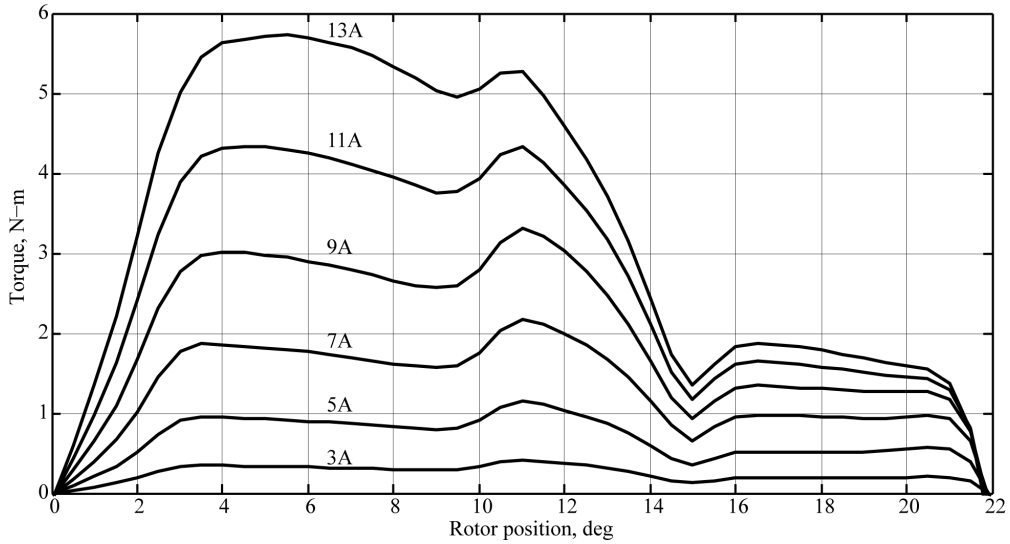

Figure 4.3: Torque contributed by reluctance in the DSPMSRM.

Table 4.2: Average torque w.r.t phase current contributed by phase current and reluctance only.

Phase Current A	Reluctance Contribution N-m	Magnet Contribution N-m	% Total
3	0.25	1.05	80%
5	0.69	1.5	69%
7	1.33	1.66	56%
9	2.0	1.65	45%
11	2.8	1.62	36%
13	3.5	1.6	31%

The percentage increase in electromagnetic torque in the novel machine decreases as the phase

current level increases. The operating point of the 4ecore srm is approximately 3.6 N-m at its rated speed. RMS current required to generate that average torque for the 4ecore SRM is approximately 11.4 A, and for the novel DSPMSRM, it is 8.7 A. The reduction in RMS current for 3.6 N-m average torque is 26%, which would lower resistive losses and core-losses for the novel DSPMSRM. At 50% of the output load the reduction in RMS current for the conventional machine and DSPMSRM are 7A and 4A, respectively. A 43% reduction in RMS current is required to generate the same output torque.

4.3 Magnetizing characteristics

Comparison of the magnetization characteristics is an important tool to compare the output power capabilities of electric machines. Figs. 4.4(a) and 4.4(b) show the magnetization characteristics of the conventional and novel machines, respectively, when only one machine phase is excited. Flux-linkage vs. phase current plotted for rotor positions from the unaligned position to the aligned position are depicted in the figures. Fig. 4.4(c) shows both magnetization characteristics overlapped for comparison. The lower bound is total flux-linkage of a phase winding from the phase current and induced PM flux at the unaligned position. The upper bound is total flux-linkage at the aligned position. By the principle of virtual work, area enclosed by the current-position-flux-linkage trajectory is e total output mechanical work due to reluctance and PM torque. Since net output work done by cogging over one electrical cycle is zero, magnetizing characteristics are sufficient to evaluate average work done in one electrical cycle for both machines, by:

$$dW = \int_0^i \left(\lambda(\theta_u, i) - \lambda(\theta_a, i)\right) di \tag{4.4}$$

where θ_u and θ_a are the rotor positions where flux linkage is minimum and flux-linkage is maximum for each current, respectively.

Table 4.3 shows the work done during one electrical cycle of conduction period for the DSPM-SRM. The work done in one electrical cycle is calculated and converted to average torque by,

$$T_{avg} = \frac{dw}{\theta_u - \theta_a} \tag{4.5}$$

The average torque correlates well with the average torque from finite element simulations using the Maxwell stress tensor to evaluate the instantaneous torque in the air gap of the DSPMSRM,

shown in Table 4.1. Discrepancies are due to minor errors in the integration of the flux-linkage characteristics.

Table 4.3: Work and average torque done from magnetization characteristics.

Phase Current A	Novel DSPMSRM mJ	Novel DSPMSRM N-m	Conventional mJ	Conventional N-m
1	1960	0.74	14	0.037
2	1829	0.88	57	0.17
3	1693	1.21	128	0.35
4	1536	1.68	227	0.63
5	1407	2.07	352	0.96
6	1258	2.46	493	1.36
7	1103	2.87	643	1.73
8	946	3.28	798	2.09
9	786	3.67	954	2.53
10	624	4.04	1109	2.99
11	463	4.4	1265	3.29
12	304	4.76	1416	3.69
13	148	5.1	1564	4.07

4.4 Comparison of self inductance

Since permeability of the PM is roughly equal to permeability of free space, the PM increases total reluctance of the DSPMSRM and result in a lowering of phase inductance compared to the 4ecore SRM. To calculate self inductance of the novel DSPMSRM, the machine is simulated by disabling the magnets‘ field. The magnet is disabled by creating a material with the same permeability of the PM without any remanence or coercivity in place of the PM.

Figs. 4.5(a) and 4.5(b) show the inductance vs. position for current levels for the 4ecore SRM and DSPMSRM, respectively. Reduction of phase self inductance due to presence of PMs in the

air gap path is apparent from the Fig. 4.5(b). Minimum inductance of the SRM in these designs are approximately equal, 7mH, since the a majority of the flux from the excited phase is returning through the unexcited stator poles instead of the larger permeance path of the shared pole. The air gap around would stator poles is 0.3mm while the effective air gap around the shared stator poles is 1mm greater due to the magnet. Inductance at the aligned position is reduced by 30% at the current excitation of 1A.

Fig. 4.6 shows the torque constants and saliency ratio of both machines as a function of phase current. The torque constant is calculated using the following expression,

$$k_t = \frac{L_u(i) - L_a(i)}{\theta_u - \theta_i} \tag{4.6}$$

where L is self-inductance of a phase, subscripts a and u denote the unaligned and aligned positions, respectively. The saliency ratio of the SRM, is the ratio of its minimum inductance to its maximum inductance at various current levels. The greater the saliency ratio, the higher the torque contributed by reluctance variation and phase winding excitation. The saliency ratio of the novel SRM is lower than the conventional SRM due to the larger effective air gap. The permeability of the magnet is equivalent to air which decreases the saliency of the novel SRM and accounts for the reduction in pure reluctance torque.

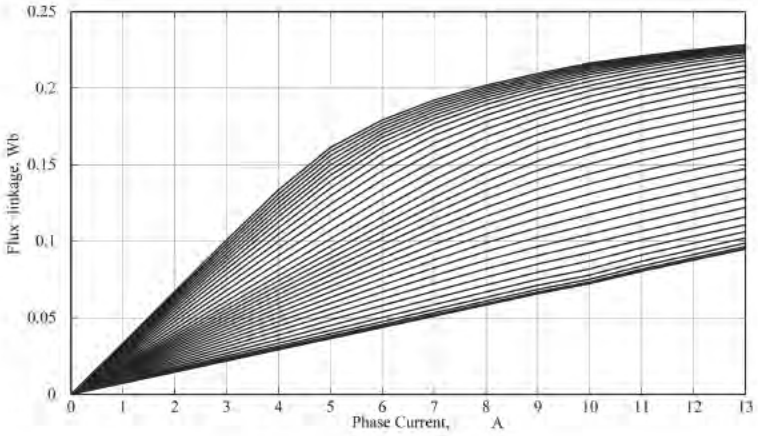

(a) Conventional 4-ecore SRM

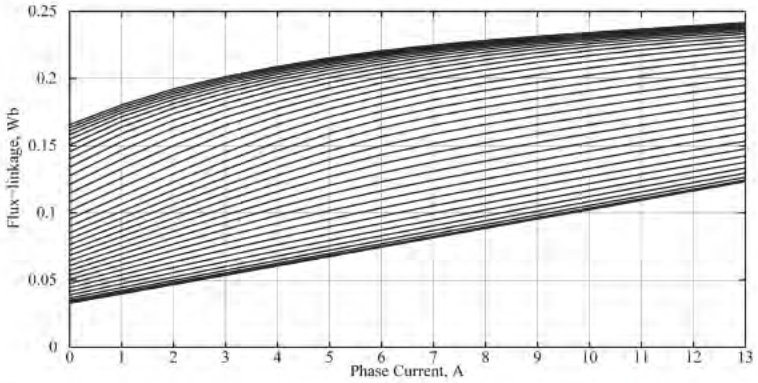

(b) Novel DSPMSRM

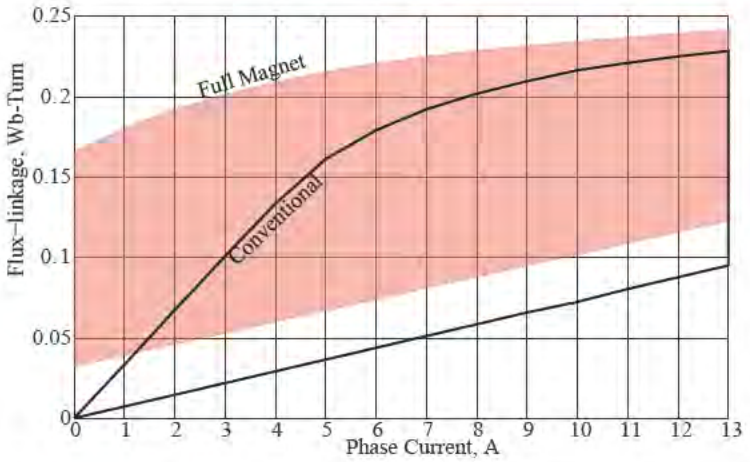

(c) Comparison of both characteristics

Figure 4.4: Magnetization characteristics (a) conventional 4-ecore SRM and (b) novel DSPMSRM for phase currents from 0A to 13A in 1A increments from the aligned to unaligned position

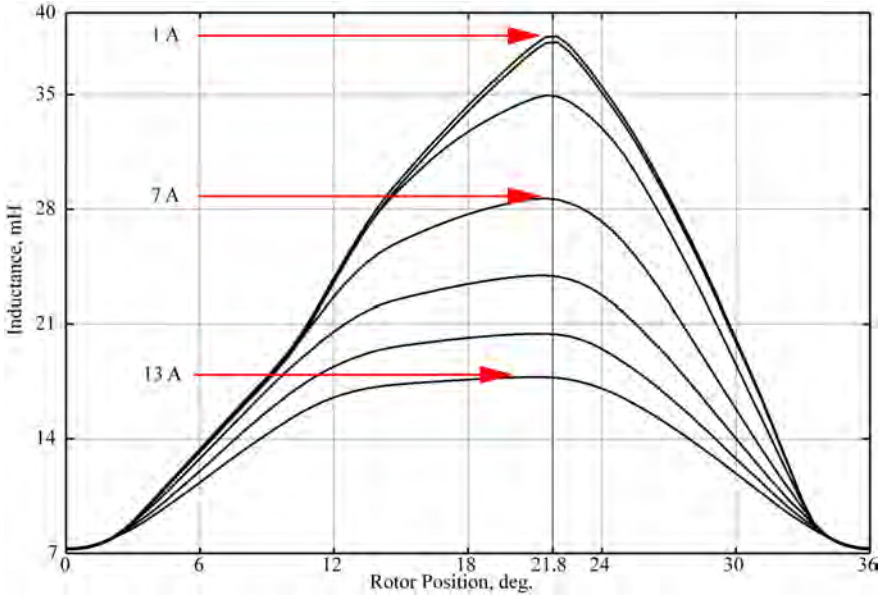

(a) Conventional 4-ecore SRM

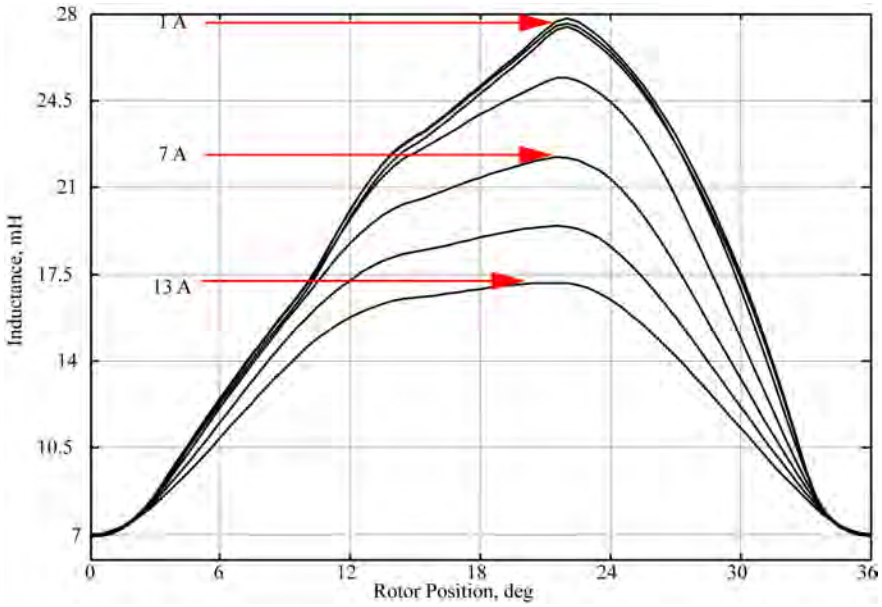

(b) Novel DSPMSRM

Figure 4.5: Inductance characteristics (a) conventional 4-ecore SRM and (b) novel DSPMSRM for phase currents from one rotor alignment to the next rotor alignment with the stator phase pole.

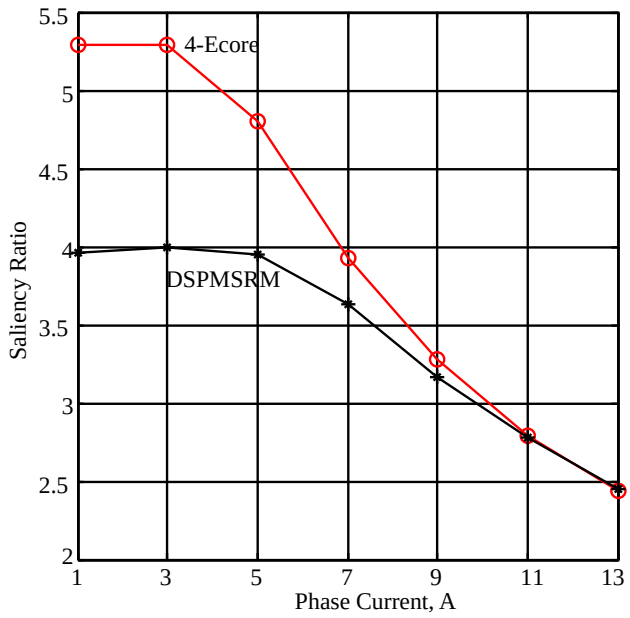

(a) Saliency Ratio

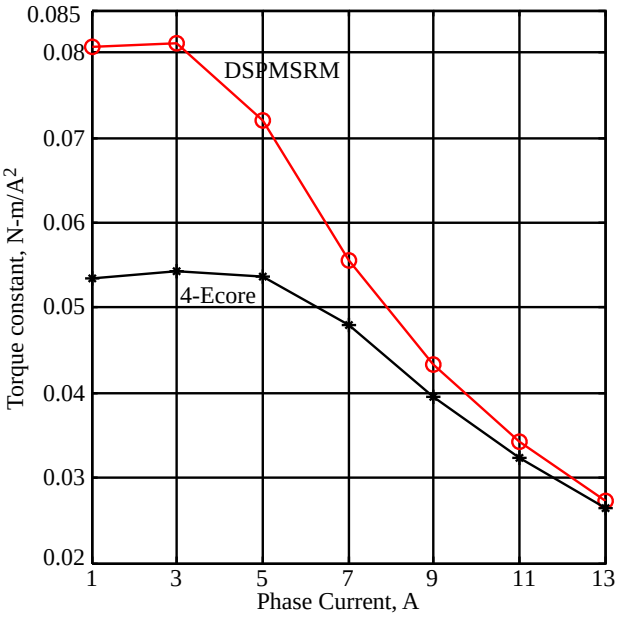

(b) Torque Constant

Figure 4.6: (a) Saliency and (b) torque constant for the conventional 4ecore SRM and novel DSPM-SRM for phase currents.

4.5 Dynamic simulation of the DSPMSRM

Dynamic simulations are carried out for the novel DSPMSRM and 4ecore SRM. The power converter shown in Fig. 4.7(a) is employed to control the motor-drive system. Full non-linear system simulation is performed with the aid of finite element analysis. Effects of end turn inductance which is not modeled in 2D finite element analysis, is used in series with the phase windings. End turns for the machine is estimated using [65],

$$L_e = 2\ N^2\ \mu_o \frac{\overline{L}_{end}}{\pi} \ln\left(\frac{8\frac{\overline{L}_{end}}{\pi}}{0.447\sqrt{h_c\ d_c}} - 2\right) \tag{4.7}$$

where N is the number of around one pole of the SRM, $\overline{L}_{end}$ is the mean length of an end turn assuming a semicircular end winding, and h_c and d_c are the height and axial thickness of the end winding. Winding dimensions were measured from a prototype of the 4ecore SRM. End turn inductance for the novel DSPMSRM is equal since both machines have the same winding configuration, frame size and stack height. Calculated end turn inductance per phase is 1.2 mH.

In order to predict efficiency, core-loss is obtained after post-processing magnetic field density in each iron mesh element. Due to limitations of finite element modeling, the solver does not account for core-loss while solving for fields. Therefore, the core-loss has no effect on the solution. Core-loss for electrical steel is estimated using the Steinmetz equation without DC field bias,

$$P_{core} = P_e + Ph = k_1 B^2 + K_2 B^{1.5}, \mathrm{W/m^3} \tag{4.8}$$

where B is the peak flux density. The eddy current loss is

$$P_e = k_c f^2 B^2 \mathrm{W/m^3} \tag{4.9}$$

and the hysteresis loss is,

$$P_h = k_h f B^2 \mathrm{W/m^3} \tag{4.10}$$

Substituting (4.9) and (4.10) in (4.8) and rearranging,

$$k_1 = k_d c k_h f + k_c f^2 \tag{4.11}$$

$$k_2 = k_e f^{1.5} \tag{4.12}$$

The eddy current coefficient is a function of the electrical steel's conductivity, σ, and lamination thickness, d. M-19 24G steel is used in both machines. The eddy loss coefficient is [95],

$$k_c = \pi^2 \sigma \frac{d^2}{6} \tag{4.13}$$

Manufacturer data-sheets which express core-loss (W) as a function of peak flux density (B) with sinusoidal excitation are used to estimate coefficient, k_1, by minimizing the squared error using the function,

$$\sum \left[W(B,f) - \left(k_1 B^2 + K_2 B^{1.5} \right) \right]^2 \cong \sum \left[W(B,f) - \left(k_1 B^2 \right) \right]^2 \tag{4.14}$$

where $W(B,f)$ is total core loss for a frequency and peak flux density combination, in the material. Excessive loss is normally neglected because its contribution in total core loss is very small compared to the the sum of hysteresis and eddy loss. The hysteresis loss coefficient becomes,

$$K_h = \frac{k_1 - k_c f^2}{f} \tag{4.15}$$

Coefficients estimated by the method shown above are programmed into finite element software to estimate core-loss from dynamic simulations. In Chapter 2, manual estimation of core-loss is performed by evaluating energy lost from the flux density cycle. In this chapter, core-loss is estimated dynamically by the finite element program without having to approximate flux densities in various iron sections and integrate. The drawback of the automated method by programming Steinmetz's equation in the finite element program is loss of separation of eddy and hysteresis losses. Only total loss core-loss is estimated.

For the dynamic simulation, both motors are operated as torque drives. The rotor is locked to an external velocity source rotating at 3600 rev/min and instantaneous output torque is measured. To estimate efficiency of the motor, without considering mechanical losses, output power is appended by core-loss and resistive loss to estimate machine efficiency at the simulated operating point:

$$\text{Efficiency}\% = \frac{P_{out}}{P_{out} + P_{core} + P_r} \cdot 100 \tag{4.16}$$

where P_r is resistive loss and P_{out} is air gap power - the product of average torque and rotor velocity.

Air gap power cannot to be used measure efficiency of a motor in a real application, due to mechanical losses during rotation. Consider a simple first order mechanical load with no gearing,

$$J\frac{d\omega}{dt} + B_f\,\omega = T_e - T_l \tag{4.17}$$

where J is the inertia of the rotor with shaft and bearing and B_f is the rotation friction coefficient. At steady state, the first term becomes zero and only rotation friction losses remain. The rotation friction coefficient is estimated from data provided from a different motor setup using the same mechanical fixture. Usable output power, shaft power, is air gap power minus friction losses. Measurable efficiency of the mechanical system is:

$$\text{Efficiency}'\% = \frac{P_{out} - P_f}{(P_{out} - P_f) + P_{core} + P_r} \cdot 100 \tag{4.18}$$

where $P_f = B_f\,\omega^2$ is the rotation friction loss. The total friction loss at 3600 rev/min is 298W.

4.6 Single pulse peak power operation

The goal of the simulation is to observe the output power capabilities of both SRMs and their efficiencies. Single pulse voltage for open loop speed control is employed. At the rated operating point, back-emf of the motor is almost equal to source voltage. By using single pulse voltage control, switching losses of the converter are minimized. In a phases‘ electrical cycle, a switch changes its state twice, instead of every switching period in an electrical cycle which increases losses [36].

Single pulse voltage control has a drawback; controlling the current trajectory isn‘t possible. For phase A‘s conduction period, transistor T1 and T2 are switched on for a predetermined period, which builds up current in the motor phase. After the dwell period has passed, both transistors are switched off concurrently and current decays through diodes D1 and D2. Turn on and turn off angles were adjusted dynamically until conventional SRM operated delivered its rated output power, 1384W. Fig. 4.7(b) shows the single-pulse control strategy used in the dynamic simulations.

Figs. 4.8 and 4.9 show steady state results of the simulation from the 4ecore SRM and DSPM-SRM, respectively. The controller was tuned for the 4ecore SRM and same turn on and turn off angles are used for the DSPMSRM. Core-loss estimated from dynamic simulations for the DSPM-SRM and 4ecore SRMs are, 119W and 122W, respectively. Average peak-to-peak torque ripple during simulation of the DSPMSRM is 6.3 N-m and 4.25 N-m for 4ecore SRM. Higher torque ripple for the DSPMSRM is expected due to its higher output power or average torque. The 4ecore machine delivers a torque of 3.65 N-m at 3600 rpm. Air gap power at the rated operating point is 1377W and the input power 1559W, with an rms phase current of 7.6A. Air gap power of the DSPMSRM is 1884W with 2067W input electrical energy. Average output torque is 4.99 N-m. Copper losses for both machines are approximately 64W. Table 4.4 summarizes results from dynamic simulation, which clearly shows the increased power density of the DSPMSRM without flux-reversal in the stator core. Efficiencies of the DSPMSRM and 4ecore are 91.3% and 88%, respectively. To evaluate the DSPMSRM at the same power level as the 4ecore SRM, peak output power of original the DSPMSRM is reduced by decreasing its stack length because power is proportional to volume of the machine, holding other design variables constant. Reducing stack length of the machine also reduces reluctance of the air gaps and PMs. The air gap power of the original DSPMSRM is approximately 30% higher than the reference 4ecore machine. To match the same power level, stack length is reduced by 30% to 38mm. The new number of turns per phase-pole can be estimated by maintaining the same rms phase current for both machines:

$$T'_{ph} = \sqrt{\frac{T_{ph}}{\left(\frac{L'_z}{L_z}\right)}} = \sqrt{\frac{103^2}{\left(\frac{38}{70}\right)}} = 124 \tag{4.19}$$

Table 4.4: Results of dynamic simulations of both machines

	4-Ecore	DSPMSRM
Rotor velocity, rad/s	377	377
Average torque, N-m	3.65	4.99
Air gap power, W	1377	1884
Shaft power, W	1078	1585
Input power, W	1559	2067
Core-loss, W	122	90
Resistive loss, W	64	64
Peak-to-peak torque ripple	4.25	6.3
Motor Efficiency, %	88	91.3
Shaft power efficiency, %	85.5	91.9

Table 4.5: Summary of the reduced stack DSPMSRM simulation

Rotor velocity, rad/s	377
Average torque, N-m	3.89
Air gap power, W	1466
Shaft power, W	1466
Input power, W	1600
Core-loss, W	38
RMS current, A	7.3
Resistive loss, W	53
Efficiency, %	94.3
Shaft power efficiency, %	89.7
Peak-to-peak torque ripple, N-m	6.5

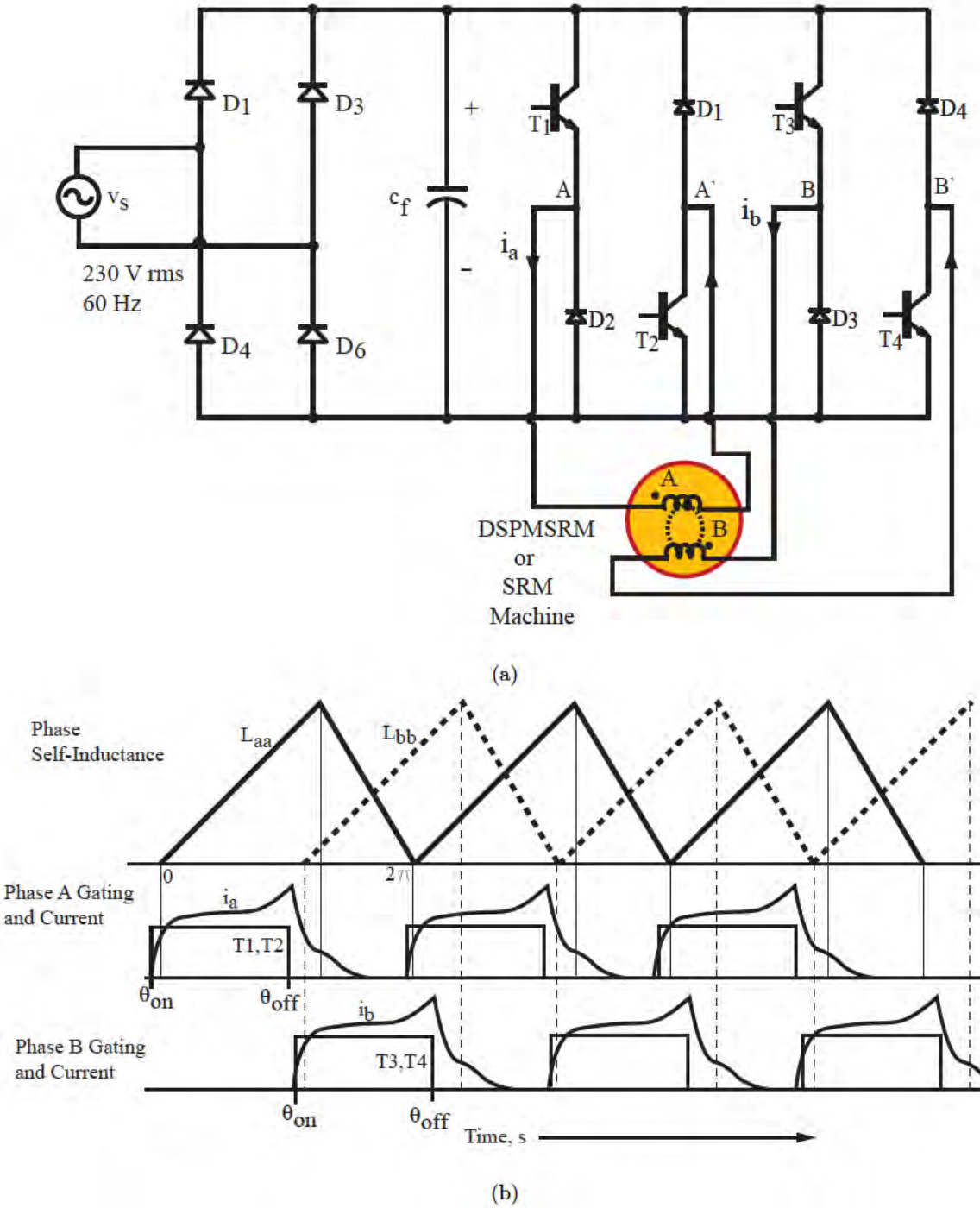

Figure 4.7: (a)Asymmetric power converter used to drive the SRM and (b) single pulse voltage control strategy used in dynamic simulations.

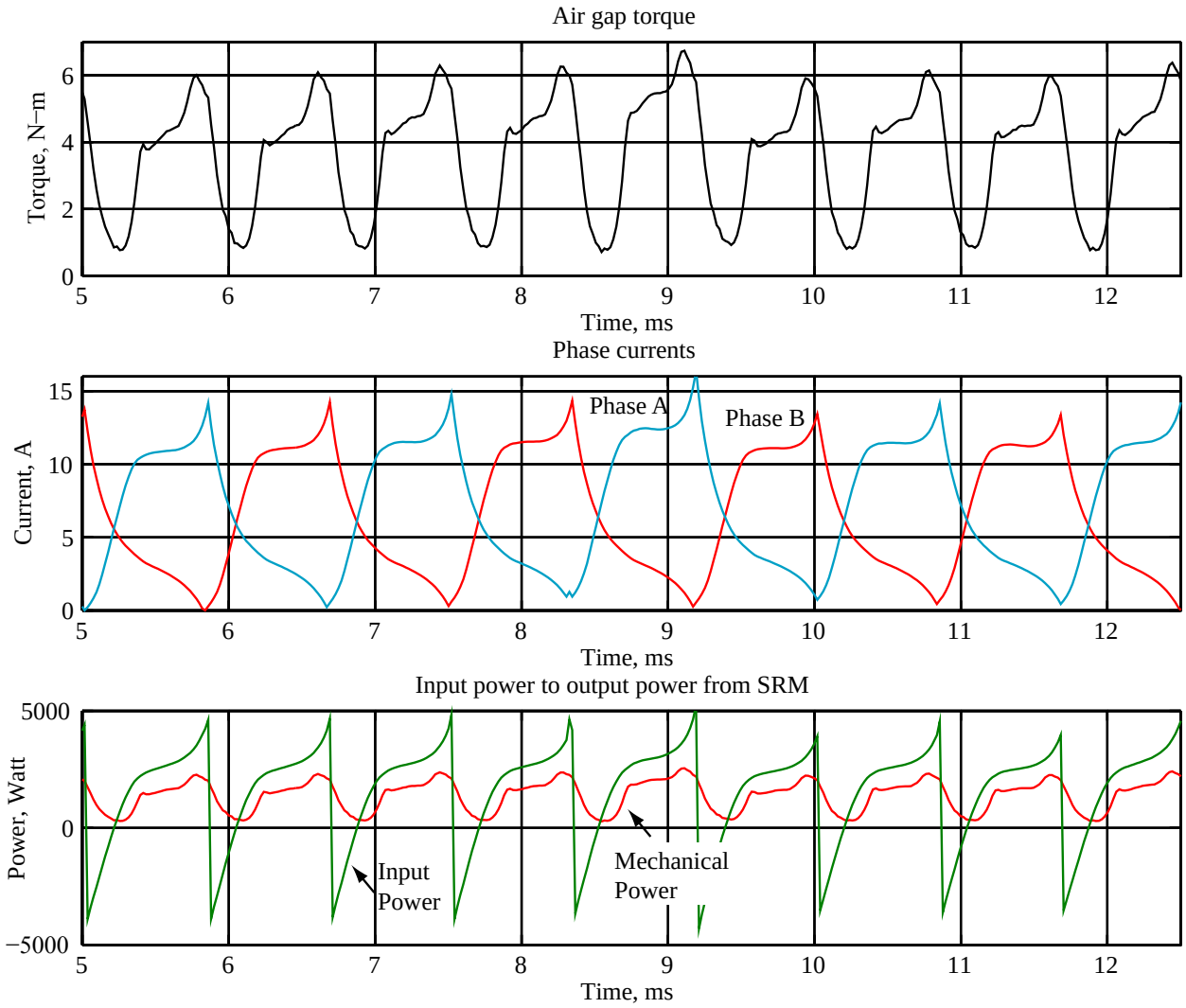

Figure 4.8: Dynamic simulation results of the 4ecore SRM.

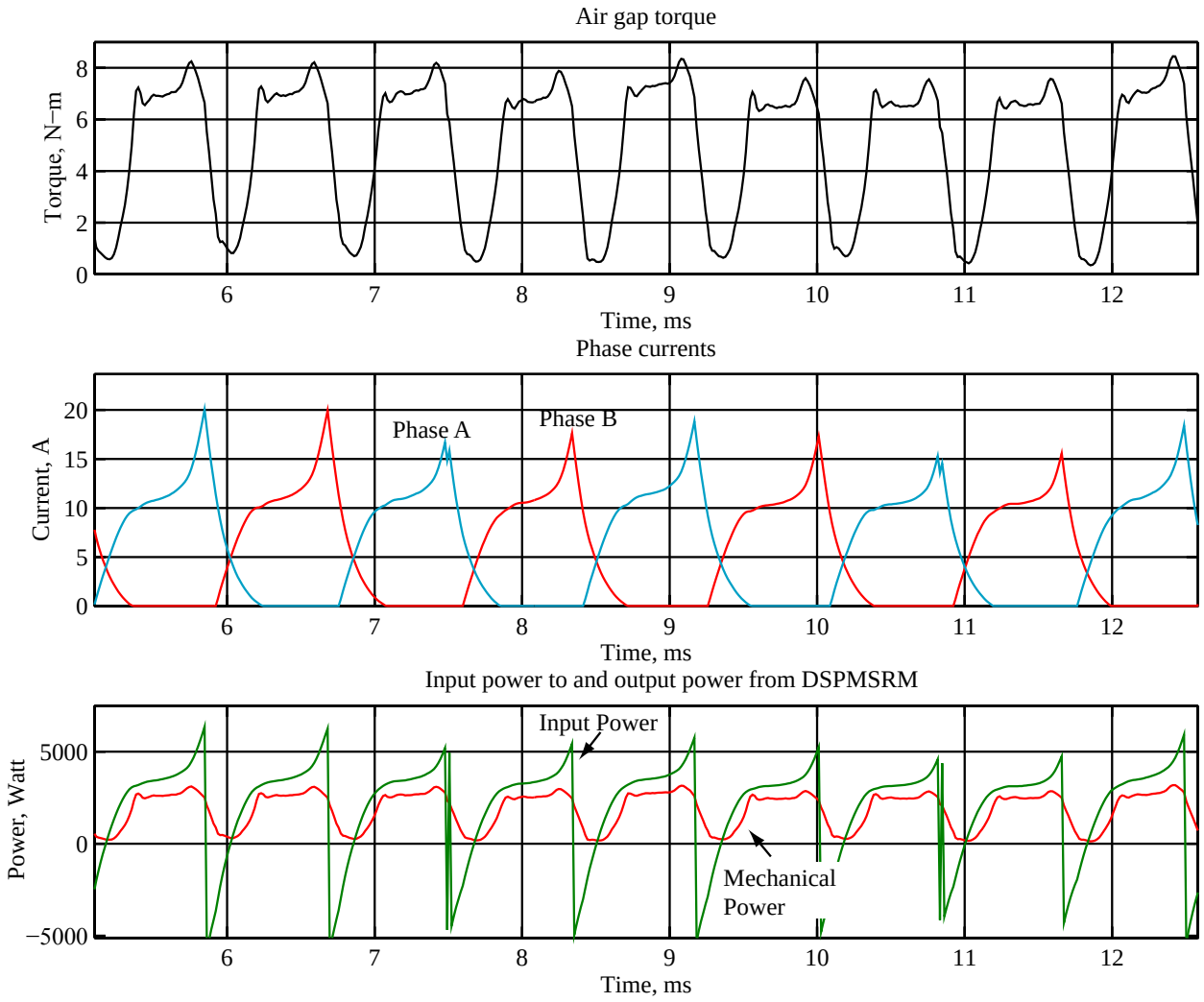

Figure 4.9: Dynamic simulation results of the novel DSPMSRM.

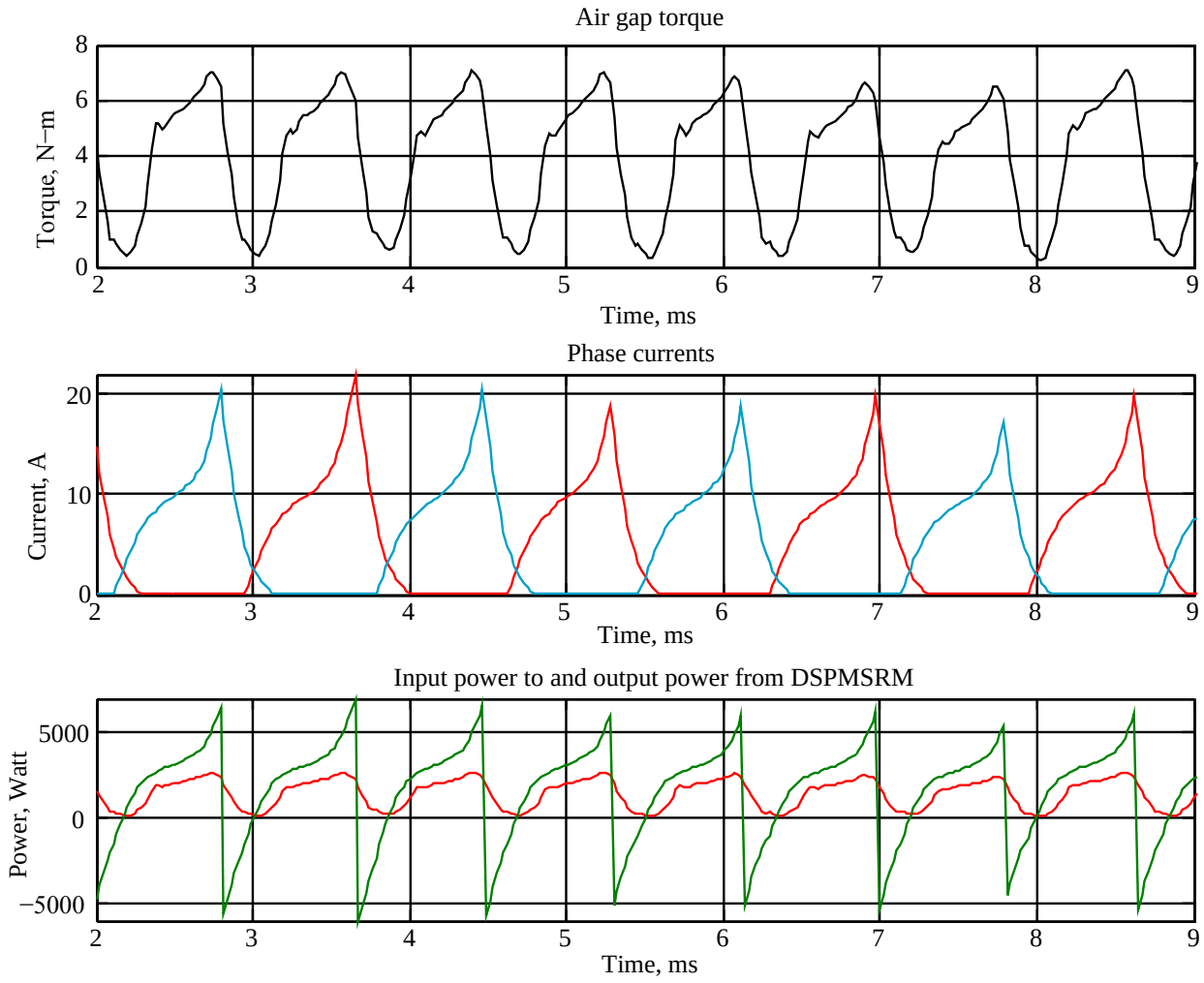

Figure 4.10: Dynamic simulation results of the DSPMSRM for a peak output power 4ecore SRM - 1384 W.

4.7 Characterisation of variable power performance

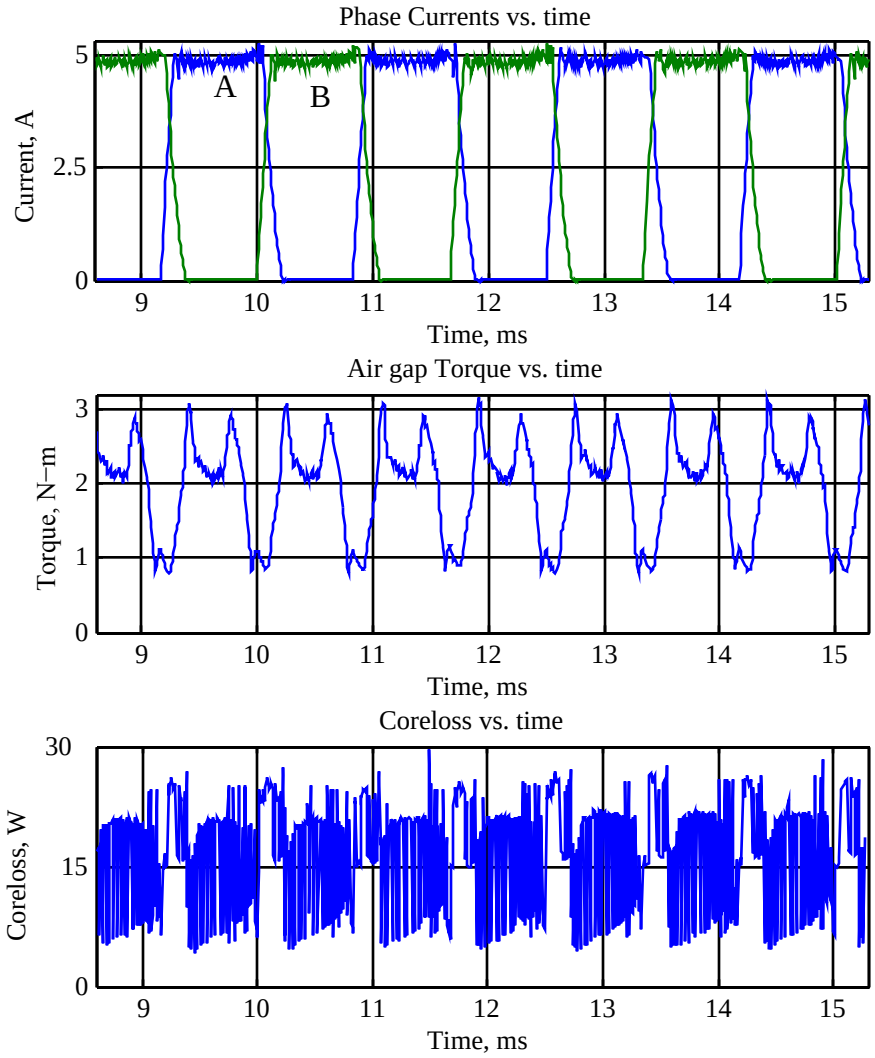

Figure 4.11: Dynamic simulation results of the 55 mm DSPMSRM for phase current command of 5A

The vast majority of research articles about electric machines cite the need to incorporate high efficiency brush-less machines with variable speed capabilities. Yet, most machines are designed to operate at a single power level, where their efficiency is highest. Very few non-servo motors are designed for multiple speed/power operation. Using a motor which is capable of operating at a higher output power than the application requires, causes lower motor drive system efficiency at the lower operating point [18]. Switching losses of power converters remain constant regardless of

speed of the motor under PWM control. Conduction losses increase as the rms current increases. For low power levels, below 10 HP and switching frequencies around 20kHz - 40kHz, switching losses and conduction losses are approximately equal.

Since the proposed DSPMSRM is capable of variable speed/power operation, variable-power efficiency of the DSPMSRM is categorized. The DSPMSRM is simulated as a torque drive (constant speed) with varying current commands to observe performance of the motor. Fixed frequency hysteresis current control is employed to control phase current from levels of 4A to 13A with 1A increments. Sampling frequency of the controller is 150 kHz. Size of the hysteresis band is 0.3A. A three degree of freedom voltage controller, which applies positive dc, negative dc and zero voltage, is employed. Turn on and turns off angles are turned dynamically for minimum torque ripple and maximum air gap power for three ranges of current levels. The dynamic simulation setup to characterize the motor are provided in Appendix A.4. The novel SRM is operated as a torque drive. Speed is fixed and the current command is updated every six electrical cycles by one Ampere.

The motor chosen to be evaluated for variable speed and variable power performance is the 55mm machine capable instead of the reduced stack machine because the 55mm stack prototype was available for experimental evaluation. Figs. 4.11 and 4.12 show the zoomed in results of two dynamic simulations for two distinct currents, namely, 5A and 8A respectively. The results show a significant second harmonic in the torque response at lower currents or loads, 1.6 N-m, at 5A. Hysteresis current control is able to regulate the phase current well with low ripple. Fig. 4.13 and 4.14 show the simulations results from hysteresis current control of the DSPMSRM. Fig. 4.15 shows the motor performance for air gap power levels from 600W to 1500W. The peak efficiency of the motor is around approx. 94.5%. DSPMSRM‘s air gap power efficiency ranges between 92% and 94.5% over the simulated power range. Under PWM operation the peak-to-peak torque ripple is 4.9 N-m. With single pulse control, torque ripple is 1.6 N-m more. At higher loads near the rated operating point of 1500W, the second harmonic of the torque ripple is negligible compared to the fundamental component. The fundamental operating frequency of this machine is 600 Hz at 3600 rpm. The core-loss in the machine increases linearly with increasing power. From 1.1 kW to 1.5 kW output power the core losses stabilize. This is attributed to the choice in excitation angles used to drive the motor. The excitation angles are optimized near the rated operating point. There is a greater overlap in the phase currents of both phases and the variation in flux density in the

stator core is lower at higher loads. Without flux reversals, flux from each phase is additive which increases the dc component of the flux density in the iron of the DSPMSRM, leading to lower core losses.

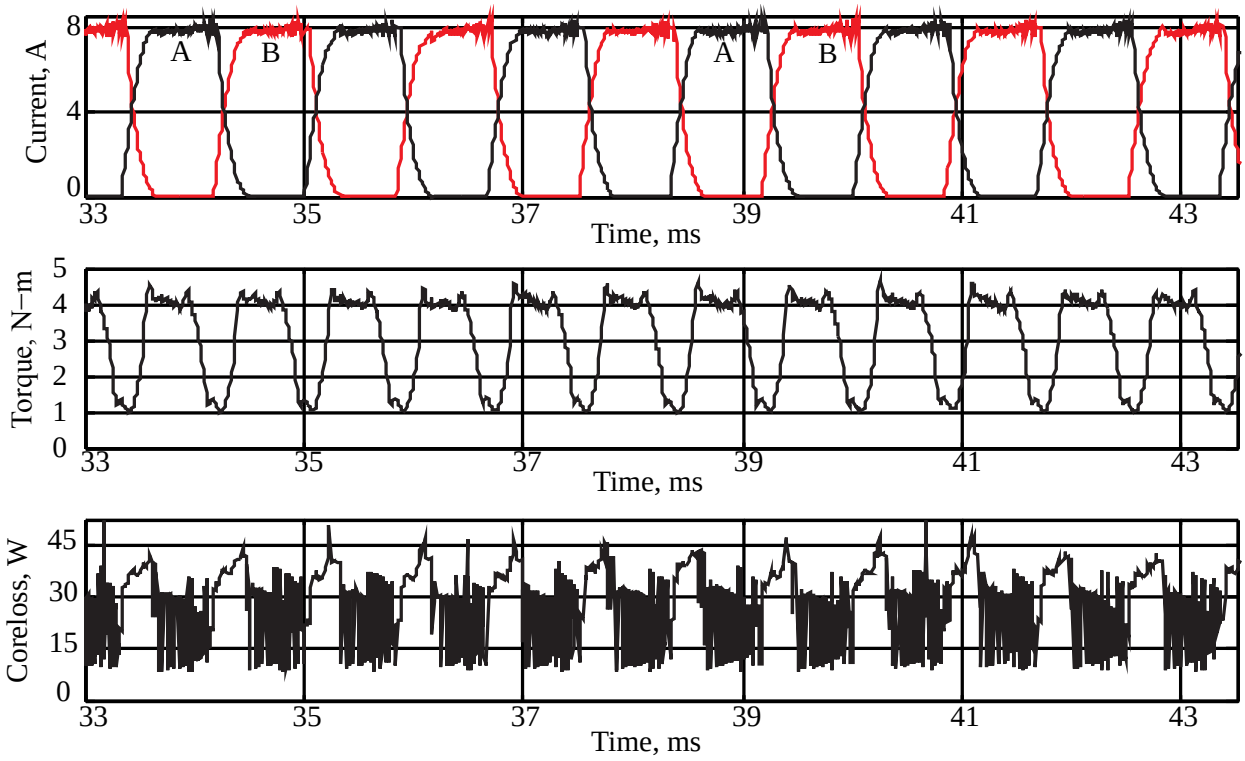

Figure 4.12: Dynamic simulation results of the DSPMSRM for phase current command of 8A

It should be noted that the one-third load efficiency of the motor is significantly higher than conventional SRMs. The enhancements provided by the magnets at partial load increases the partial load efficiency of the DSPMSRM. The 4ecore SRM requires 7.3A rms current to deliver the output power or 1440 W, while the novel SRM requires approximately 5.5A rms current to deliver power at the same output point. This reduction in input current is achieved by the magnet in the stator and can reduce the current rating of the inverter.

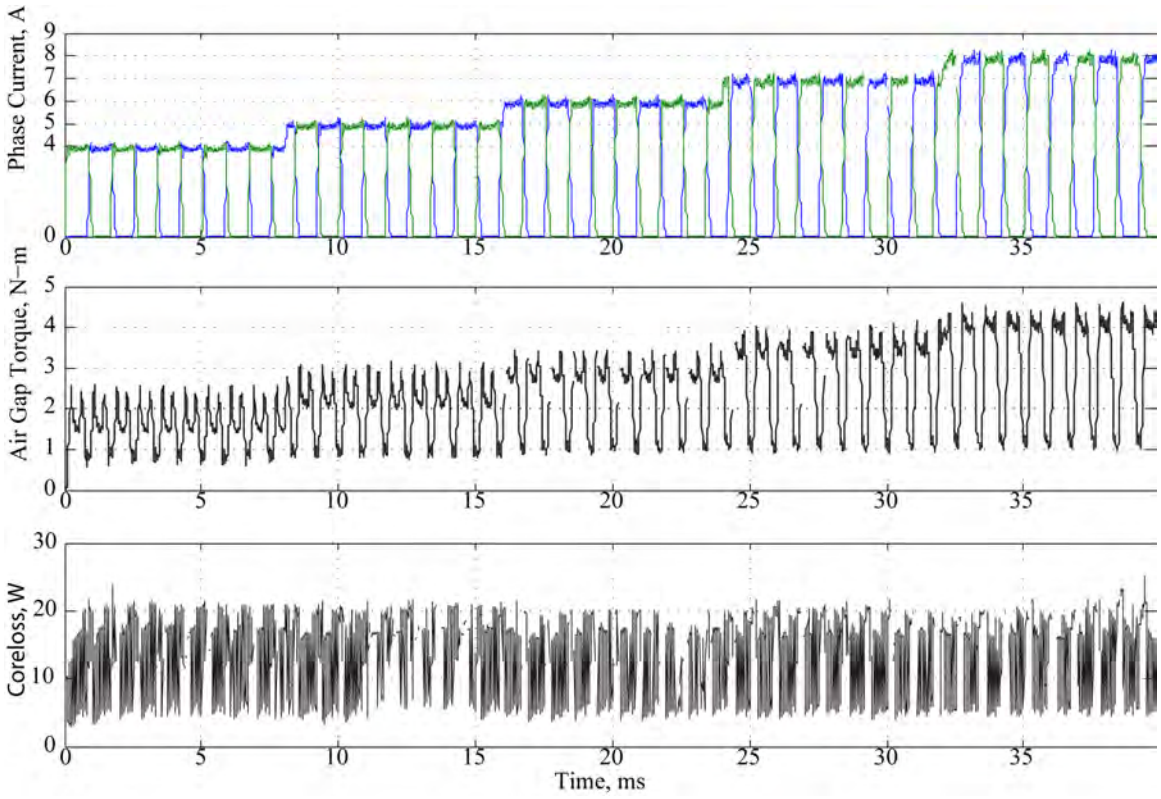

Figure 4.13: Dynamic simulation results of the DSPMSRM for phase current commands from 4A to 8A.

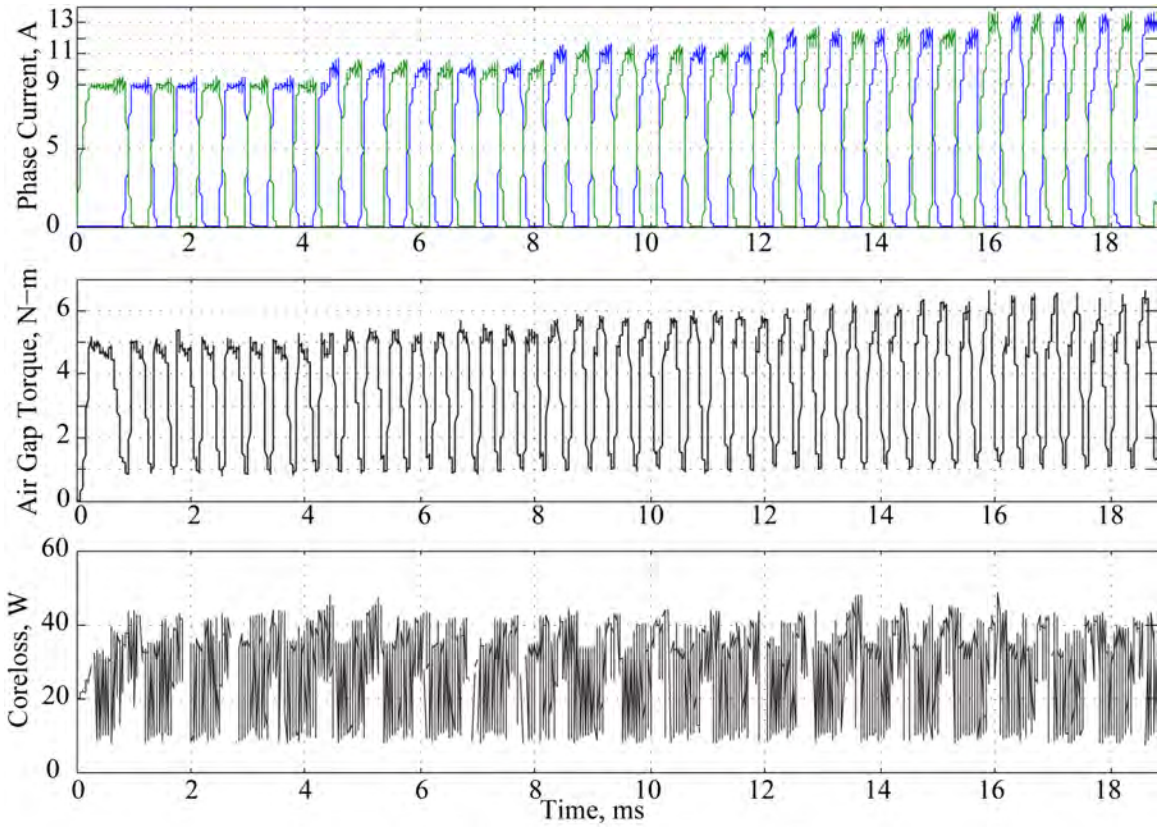

Figure 4.14: Dynamic simulation results of the DSPMSRM for phase current commands from 9A to 13A.

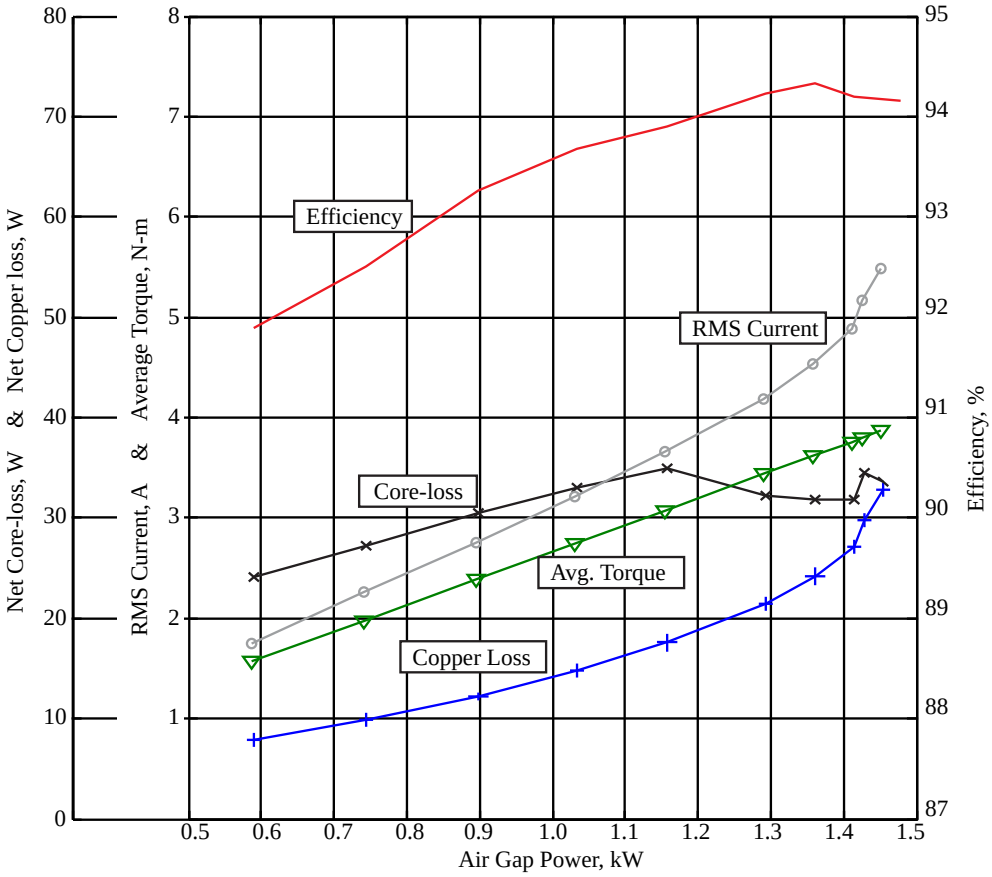

Figure 4.15: Dynamic characterization of the DSPM SRM with 55 mm stack. Rms current, average torque, efficiency, core loss and copper loss vs. air gap power.

Chapter 5

Experimental Results from the Novel DSPMSRM

5.1 Experimental Prototype

The experimental prototype was developed from the machine presented in Chapter 4. The dimensions of the machine are show in Table 5.1. Readily available prototyping M19 steel was chosen for the design. Due to limitation in magnet manufacturing and cost associated with custom magnets, the dimensional tolerance in the manufacturing of the magnets is 0.3mm. This makes the magnets dimension vary by more than the length of the air gap. The magnets received were undersized by 10% from the specified nominal thickness of 1.05mm. Figure 5.1 shows the stator and rotor laminations of the experimental prototype. The stator has an octagonal outer envelope and the rotor has slots in its back iron. The octagonal envelope was used because an existing fixture to accomodate this shape was available to assemble the prototype. These slots are added to reduced weight of the rotor and decrease the core-losses. Since each phase‘s flux does not traverse the rotor diametrically, the majority of the back iron goes unused and is removed. In Fig. 5.1(c) the stacked stators and rotor are shown along with the magnets on the shared pole. Two magnets are placed on the stator to show their thickness and height.

Table 5.1: Dimensions of the DSPMSRM Prototype

Maximum gir gap length, mm	0.3 mm
Maximum air gap length, mm	0.75 mm
Stator outer radius, mm	75
Shaft radius, mm	10
Shared pole arc, deg	36
Stator pole arc, deg	11.5
Rotor pole arc, deg	19
Stack length, mm	55
Winding turns per pole	103
Winding resistance, ohm	0.6
Magnet type	NdFeB
Magnet Energy Product	42 MG-Oe
Nominal thickness, mm	0.95 mm
Wire Gauge	16 AWG
Core Steel	M19 29GA C5

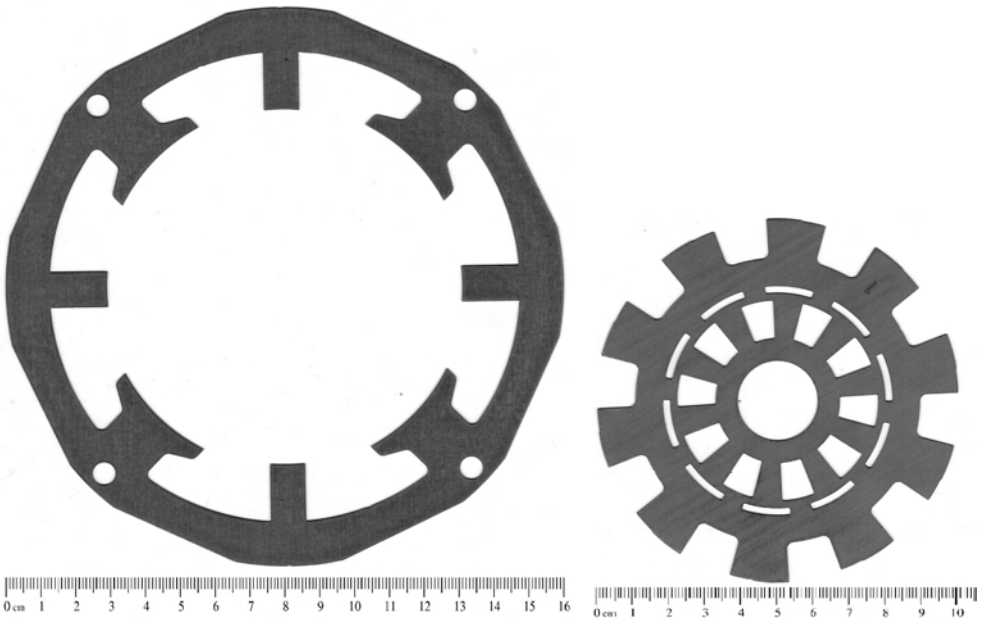

(a) (b)

(c)

Figure 5.1: (a) Stator and (b) rotor laminations used in the experimental prototype and (c) the assembled stator and rotor.

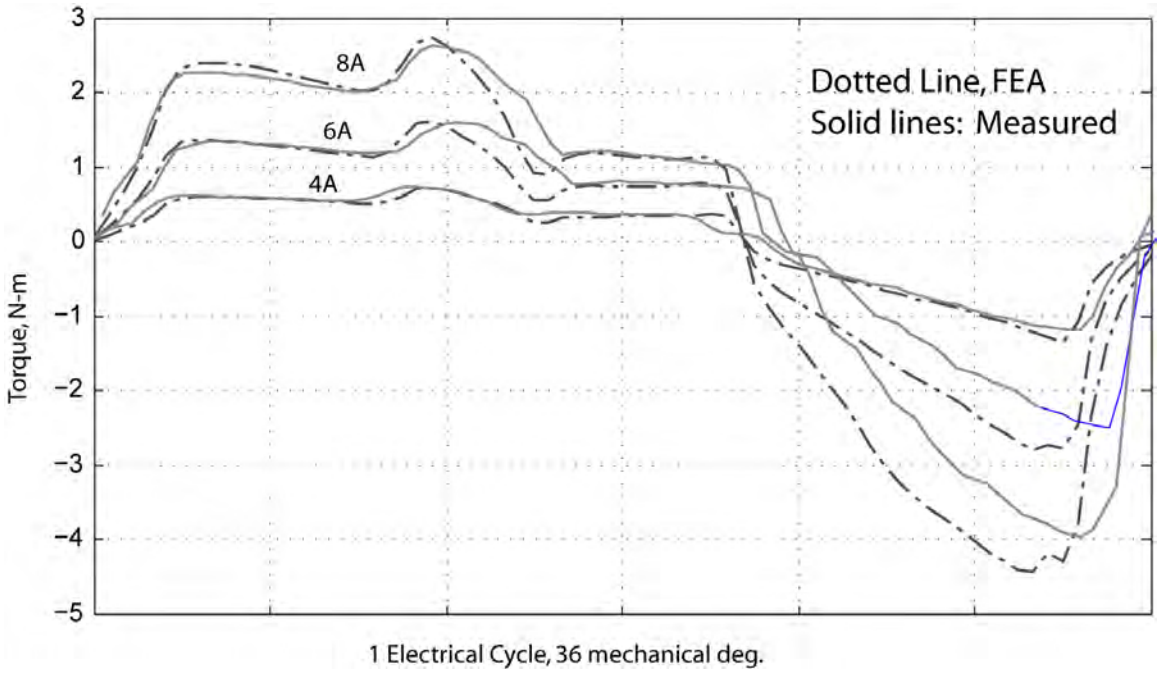

Figure 5.2: Measured and simulated cogging torque.

5.2 Static Torque Measurements

Static torque was measured for each phase for various current levels up to 8A. Due to the limit of the current source, measurements over 8A were not possible. The static torque due to reluctance was measured independently without magnets initially. The prototype was assembled without bonding the magnets to the stator. Fig. 5.2 shows the reluctance torque of the prototype and data derived from FE simulations for one and a half electrical cycles. There is less than 7% difference in the peak positive torque of the prototype at all measured current levels. Due to some slipping in engaging the cogs of the worm gear, the speed of rotation of the rotor could not be controlled precisely. The figure shows good correlation between the predicted and the measured data.

Fig. 5.4 to Fig. 5.8 show the static torque measurements that were taken with a torque cell and worm gear position governor. Due to the limitation of the torque cell, it was not possible to record both rotor position and static torque data dynamically. Hence, the magnitudes of the torque measurements of the estimated characteristics from FEA and experimental data are compared. Fig. 5.3 shows the experimental setup used to measure static torque. A hand drill was used to keep the

speed of rotation of the worm gear steady, less than 2 rpm. Data was saved to a laptop computer and post processed.

The measured cogging torque also correlated well in the experimental prototype. Magnets were bonded to the surface of the rotor pole using a quick setting epoxy and aligned to the center of the pole by plain sight. The peak of the cogging torque is 13% lower than predicted torque. Fig. 5.4 shows the measured and predicted cogging torque in the DSPMSRM. The double frequency per electrical cycle property of the cogging torque is reflected in the figure. The peak value of the estimated cogging torque is 1.65 N-m while the average peak value of the measured data is 1.4 N-m. This discrepancy can be attributed to the manufacturing of the magnets whose nominal thickness is 0.95 mm instead of 1.05 mm. It is normal for arc segment magnets to have minimum thickness of 2.5 mm in most applications. Sintering magnets less than 0.1 inch in thickness and dimensional tolerances that are three-thousandths of an inch is not standard practice in prototyping and manufacturing of electric machines.

Additional measurements of static torque with dc phase current applied to each phase were performed. Figs. 5.5 to 5.8 show the net torque in the motor for both phases and are compared to FEA data. The data is shown for both phases and one and a half electrical cycles. The general shape of the torque correlates well with the FE simulations‘ data. The peak magnitude of the torque also correlates well. There is 12%, 11%, 16% and 7% difference between the peak of the measured and simulated static torque profiles for current levels of 2A, 4A, 6A and 8A respectively. This error is acceptable given the magnet‘s manufacturing. At higher current levels the difference between the predicted and measured current levels is lower, except at 6A where the error is higher than expected but it still correlates well. Since the contribution of magnet torque to the net torque is lower at higher current levels as predicted by Table 4.2 , the impact of the thinner magnet will be low. Inductance for one phase was measured using an LCR meter and 200mA rms load current at 100 Hz. Fig. 5.9 shows the predicted inductance and the measured inductance versus position for one current level. Measuring inductance with current levels over no-load levels was not possible due to the presence of magnets on the stator. The inductance error between the 2D inductance and measured inductance at the unaligned position is 18.5% and the error at the aligned position is 12%. The average error between the measured and predicted inductance data is 16%. This error is acceptable given the manufacturing tolerances of the magnet and diference between the iron

magnetization data sheet and actual material.

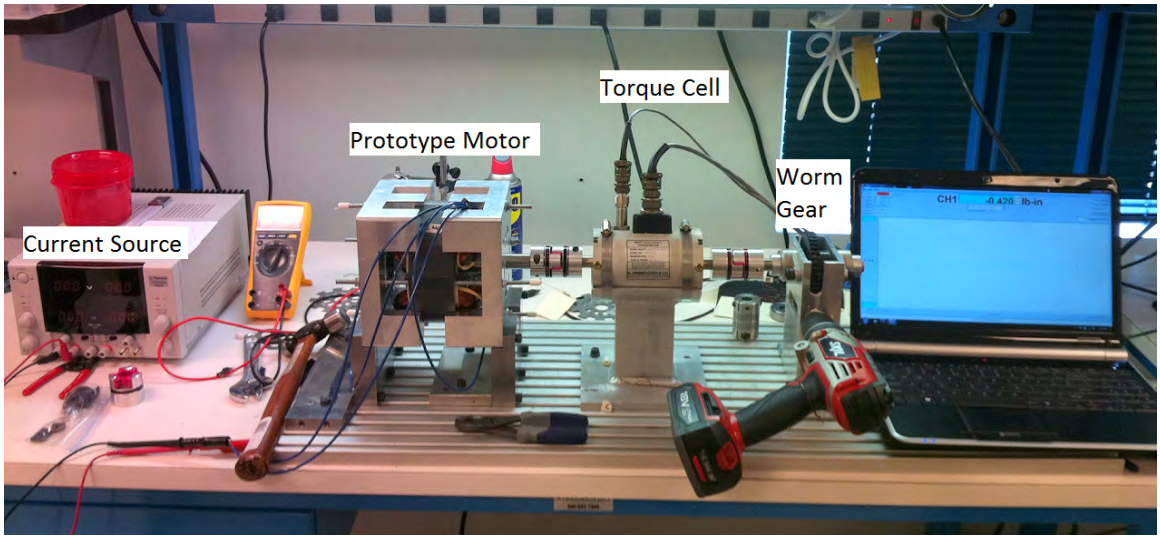

Figure 5.3: Experimental setup used to measure static torque.

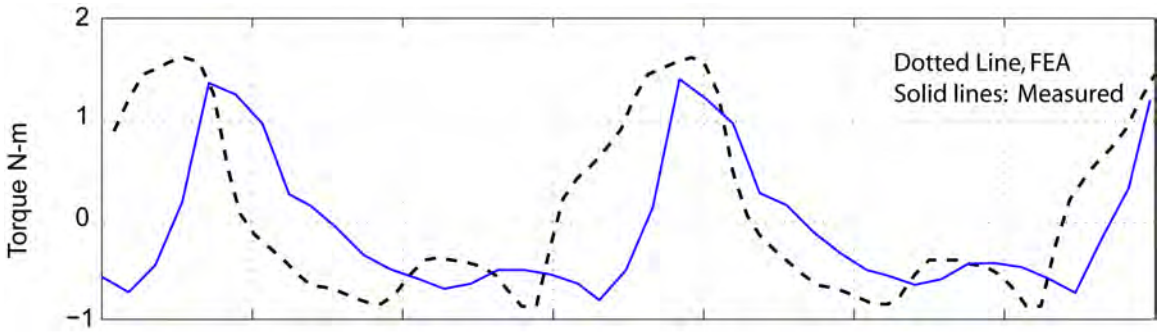

Figure 5.4: Measured and simulated cogging torque.

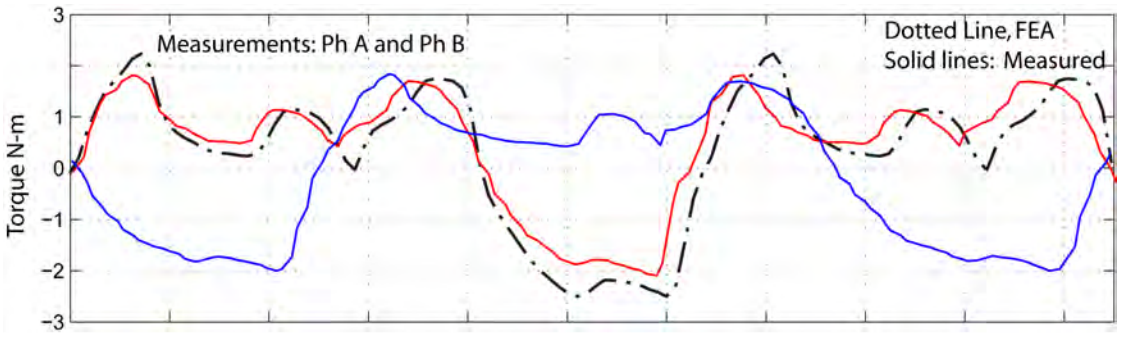

Figure 5.5: Measured and simulated torque for 2A phase current.

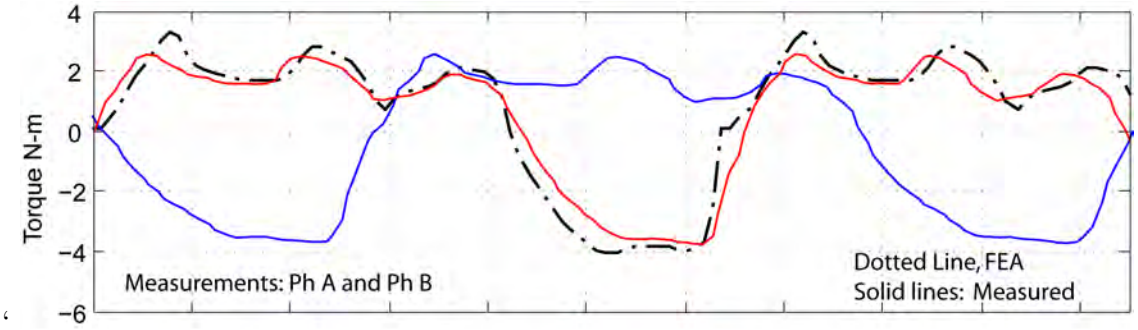

Figure 5.6: Measured and simulated torque for 4A phase current.

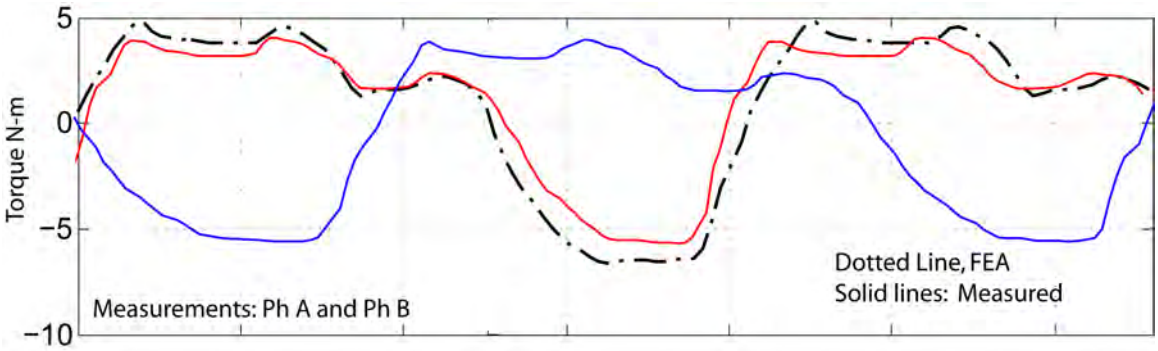

Figure 5.7: Measured and simulated torque for 6A phase current.

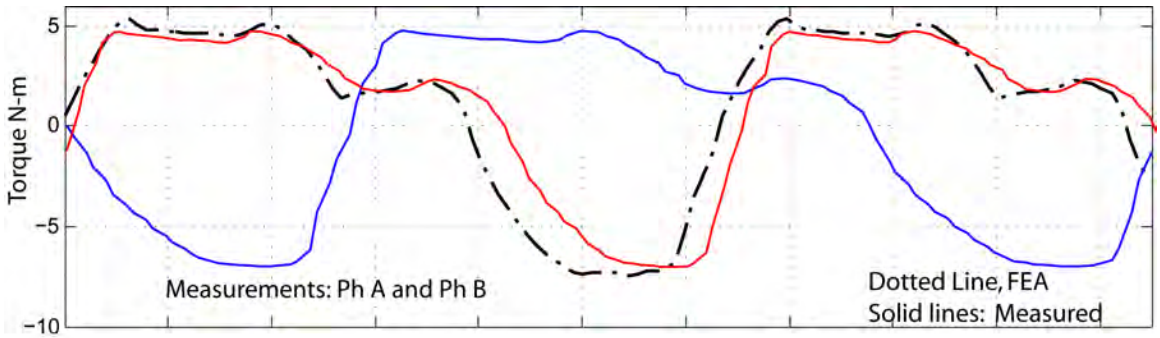

Figure 5.8: Measured and simulated torque for 8A phase current.

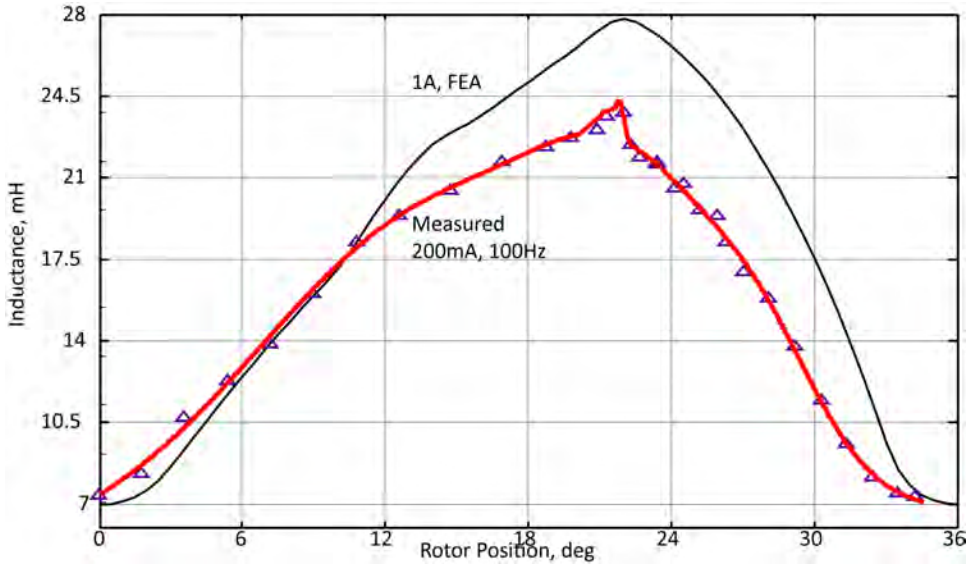

Figure 5.9: Measured inductance at no load and simulated inductance at 1A.

5.3 No Load Back-emf

In order to verify the manufacturing of the prototype completely, back-emf at no load was measured. Back-emf was measured by driving the DSPMSRM with a second SRM at 1800 rpm and 3600 rpm. Fig. 5.10 shows the simulated back-emf at 3600 rpm, having a peak of 276 V. Figs. 5.11(a) and 5.11(b) show the measured no-load back-emf at 1800 rpm and 3600 rpm, respectively. At 3600 the peak back emf is 222V which is 50V lower than the predicted value.

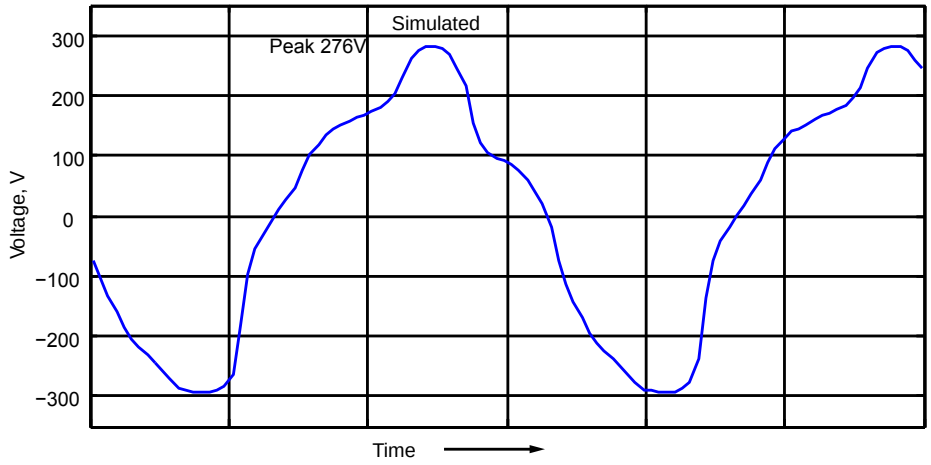

Figure 5.10: Simulated back-emf of the DSPMSRM at 3600 rpm.

Fig. 5.11(a) shows the experimental back-emf both each winding segment. The motor driving the prototype was rotating clockwise and driving the DSPMSRM counterclockwise. Hence the measured back-emf data is mirrored (vertically). The back-emf is linearly proportional to rotor speed and has 18% error as compared to the predicted peak value. This number corresponds well with the error in the measured torque at no load which has 13% error.

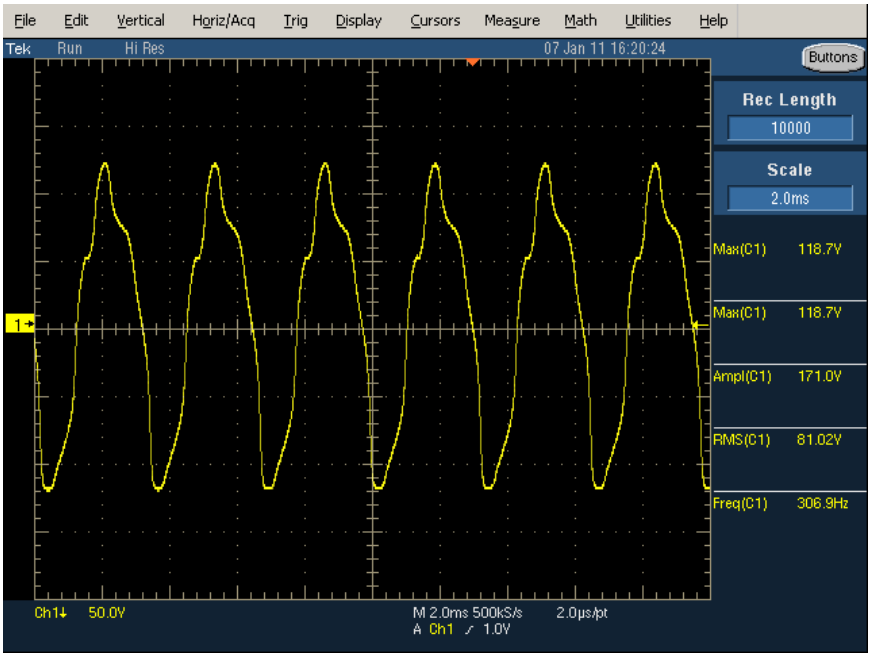

(a)

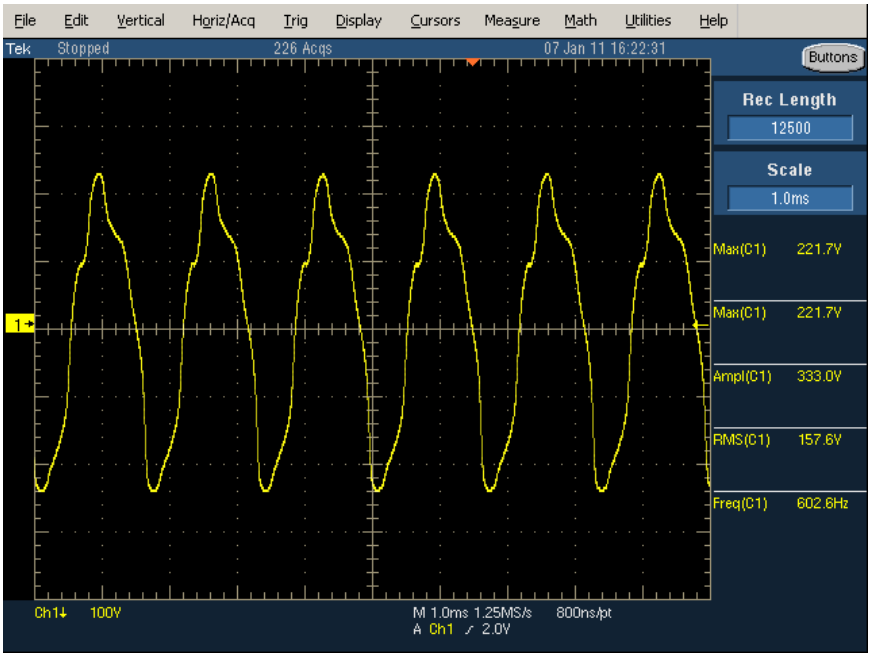

(b)

Figure 5.11: Measured back-emf of the DSPMSRM at no load for two speeds. (a) 1800 rpm and (b) 3600 rpm.

5.4 Dynamic operation and Efficiency

Figure 5.12: Drive's control execution delay.

In order to estimate efficiency of the drive, the DSPMSRM was operated in torque mode. No automatic speed control is used. Fixed turn on and turn off angles, with proportional control is employed to drive the motor. The current loop is executed at a frequency of 16 kHz which is also the PWM frequency. The current level is adjusted through a level knob on the controller and speed is controlled by changing of the load applied through the hysteresis brake. Fig. 5.13 shows the experimental setup with load, DSPMSRM and measurement devices to measure efficiency. Due to the limitations of the DSP on the drive, running the motor with hysteresis current control with 100 kHz sampling was not possible. The drive was not able to run the motor with sufficient accuracy to deliver the required power.

The DSPMSRM requires position accuracy greater of 0.3 mechanical degrees or smaller to operate with high efficiency. The drive has a sampling and control execution delay of two switching

periods which causes a maximum turn on angle error of 2.78 mechanical degrees at the rated speed 3600 rpm. Fig. 5.12 shows the delay between the instant where the drive's current controller determines the phase should be switched on and the current starts rising in the winding. The square wave above the phase currents are the turn on and turn off trigger in the current controller. This delay is quantified on the right side of the scope plot and is labeled as δt. Due to the nature of the drive's firmware, the average delay is +1.34 mechanical degrees. To fully understand the impact of the delay, back-emf shown in Fig. 5.11(b) should be observed closely. The mechanical displacement between the zero crossing of the back-emf and the negative peak is four mechanical degrees. The magnet induced emf varies can vary by 60V with a turn on delay of 1.4 degrees, which reflects on the available voltage to drive the current in the DSPMSRM. Turn on and turn off angles in Appendix A.4.2 show the difference between the turn on and turn off angles between 4A and 13A current commands is 0.6 mechanical degrees.

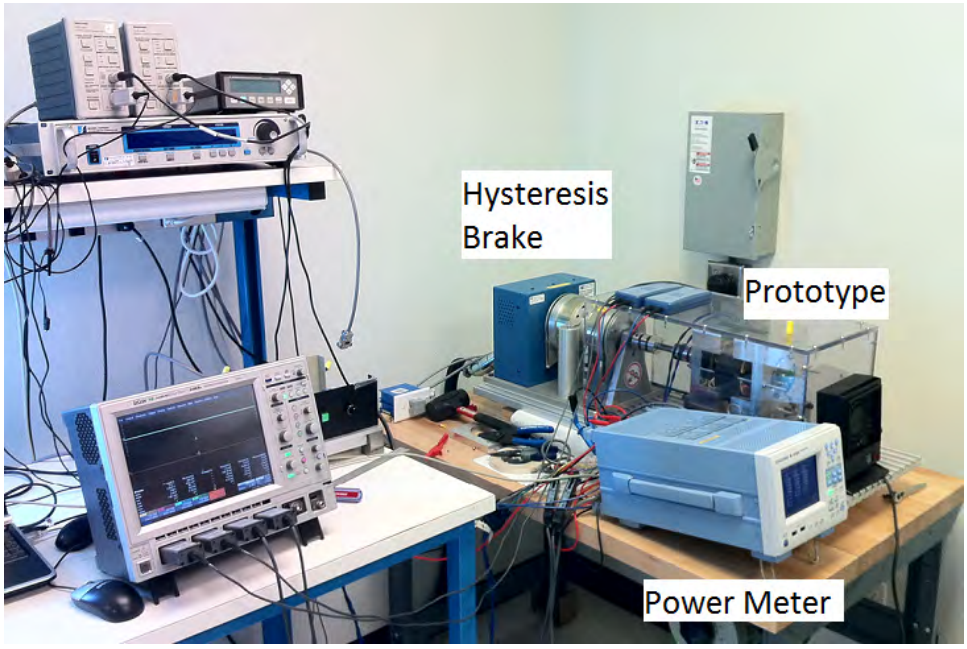

Figure 5.13: Experimental setup to measure motor efficiency.

With this drive limitation efficiency was measured with one set of turn on and turn off angles which were not optimal. Fig. 5.14 shows the motor running with current control as a torque drive. The figure shows phase current and switching phase voltage of each phase. Fig. 5.14(a) shows the drive operating at 3600rpm and 1.0N-m load. In Fig. 5.14(b) the DSPMSRM is running at 3600rpm and 3.8 N-m load (rated operating point). The drive was not able to control both phases

symmetrically nor was it able to control each phases‘ current with repeatability. Fig. 5.15(a) shows the drive operating at 3600rpm and 1.5N-m load. In Fig. 5.14(b) the DSPMSRM is running at 3600rpm and 2.0 N-m load. Efficiency was measured in the following manner. Steady state is defined to be period during which the DSPMSRM‘s speed has stabilized under open loop speed control. Using oscilloscope data and a Yokogawa power analyzer, each phase‘s power is monitored along with steady state output power from the torque transducer which is part of the hysteresis brake load. Input power is averaged over a period of one second. Average data over twenty seconds is used to calculate input power to the motor. Table 5.2 shows the data obtained from running the DSPMSRM to estimate motor efficiency. This data is plotted in Fig. 5.16. It should be noted that the RMS current and power from each phase is different as the load torque is increased. Phase B has significantly more input current than phase A due to the drive not being able to commutate phase A correctly. Hence each phase does not share the load equally. Under this unbalanced condition, the peak motor efficiency is 90.8% with a load of 3.0 N-m at 3600 rpm. This indicates that motor can deliver the maximum output power of 2.4 kW with proper control being employed. The maximum efficiency is approximately 4% points lower than the predicted efficiency.

Table 5.2: Data obtained from running the DSPMSRM as torque drive.

Load Torque, N-m	Output Power, W	Total Input Power W	Phase Power, A		RMS Current, A		AC Input Power W	Motor Efficiency
			Ph. A	Ph. B	Ph. A	Ph. B		
1.0	400	510.6	203.5	307.1	3.0	4.8	602.6	78.3%
1.5	570	693.8	274.0	419.8	3.7	3.9	805.9	82.1%
2.1	800	926.9	356.3	576.6	4.6	5.0	1072.2	86.3%
2.5	940	1065.0	399.4	665.6	5.4	5.9	1234.5	88.5%
3.0	1130	1276.6	256.0	1020.5	6.8	8.3	1530.9	90.8%
3.4	1280	1470.0	252.5	1218	6.7	10.26	1722.8	87.0%
3.8	1440	1665.4	254.9	1410.5	6.8	11.9	1912.6	86.4%

Acoustic noise radiated from the prototype running at rated load of 1.4 kW was also measured. Fig. 5.17 shows the noise spectrum with $1/3^{rd}$ octave bands with A-weighting filter applied. An

A-weighted filter is chosen because the target application of this machine is residential. Acoustic noise was measured at one point 1 meter away from the motor, normal to the stator‘s outer periphery. Noise components at 630Hz and 1.2kHz show the presence of noise at the fundamental operating frequency of 600Hz and the second harmonic of the operating frequency. The acoustic noise components at 120 Hz and 60 Hz are a result of manufacturing errors in the stator and/or rotor laminations. Minimum inductance and maximum inductance were measured for one phase with all five rotor pole pair alignments. The error in the unaligned inductance of all five poles was within expected error bounds; less than 0.4 mH. The maximum inductance varied cyclically, repeating itself every five sets of rotor poles. The maximum inductance varied between 24.5mH and 20.1mH between the five sets of the rotor poles under no-load measurements with the LCR meter. Cyclical peak inductance causes cyclical peaks in the radial force in the air gap with the same frequency. This frequency is 120 Hz or 5 sets of rotor poles at 3600 rpm and causes the 125Hz components in the radiated acoustic noise. The peak radiated noise at the rated operating point is 82dBA.

(a)

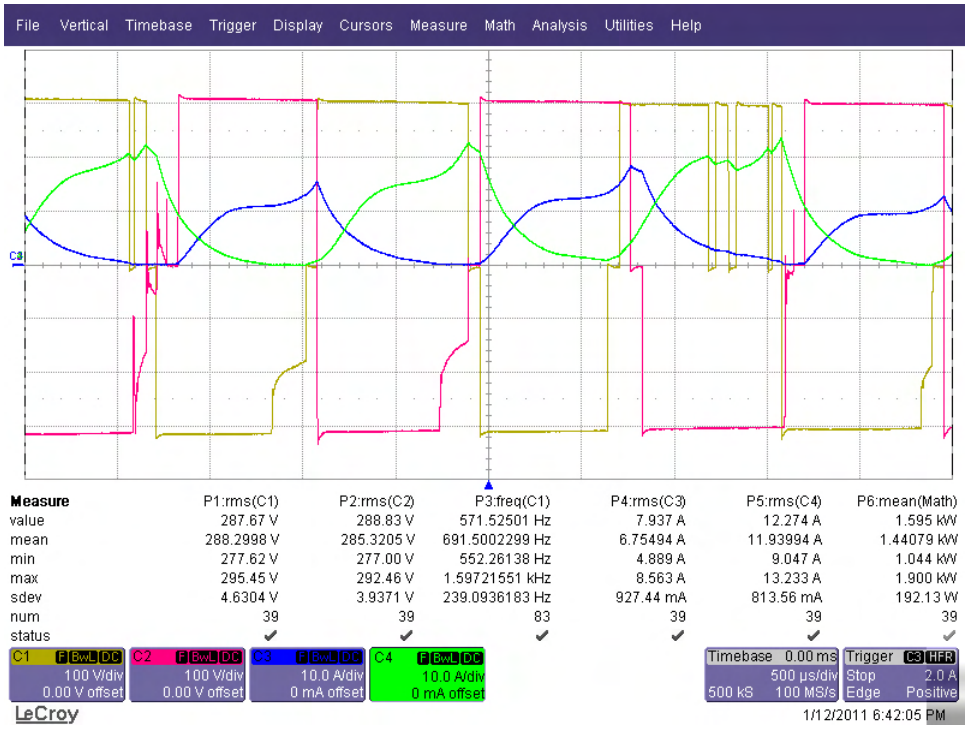

(b)

Figure 5.14: DSPMSRM operated as a torque drive at 3600 rpm. (a) 1.0 N-m load. (b) 3.8 N-m load.

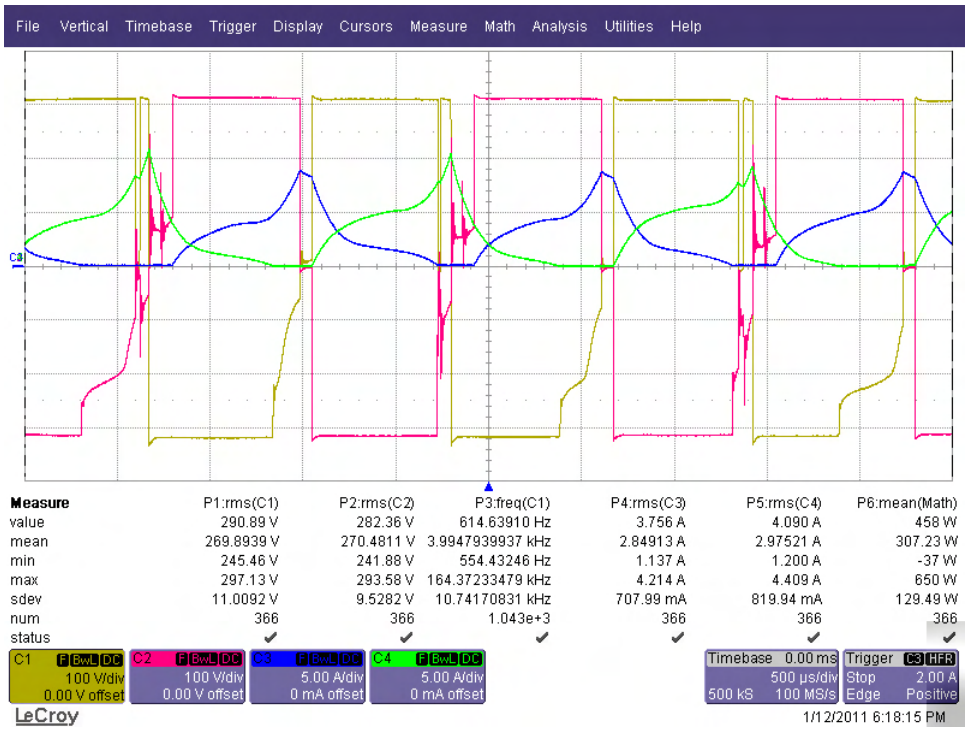

(a)

(b)

Figure 5.15: DSPMSRM operated as a torque drive at 3600 rpm. (a) 1.5 N-m load. (b) 2.0 N-m load.

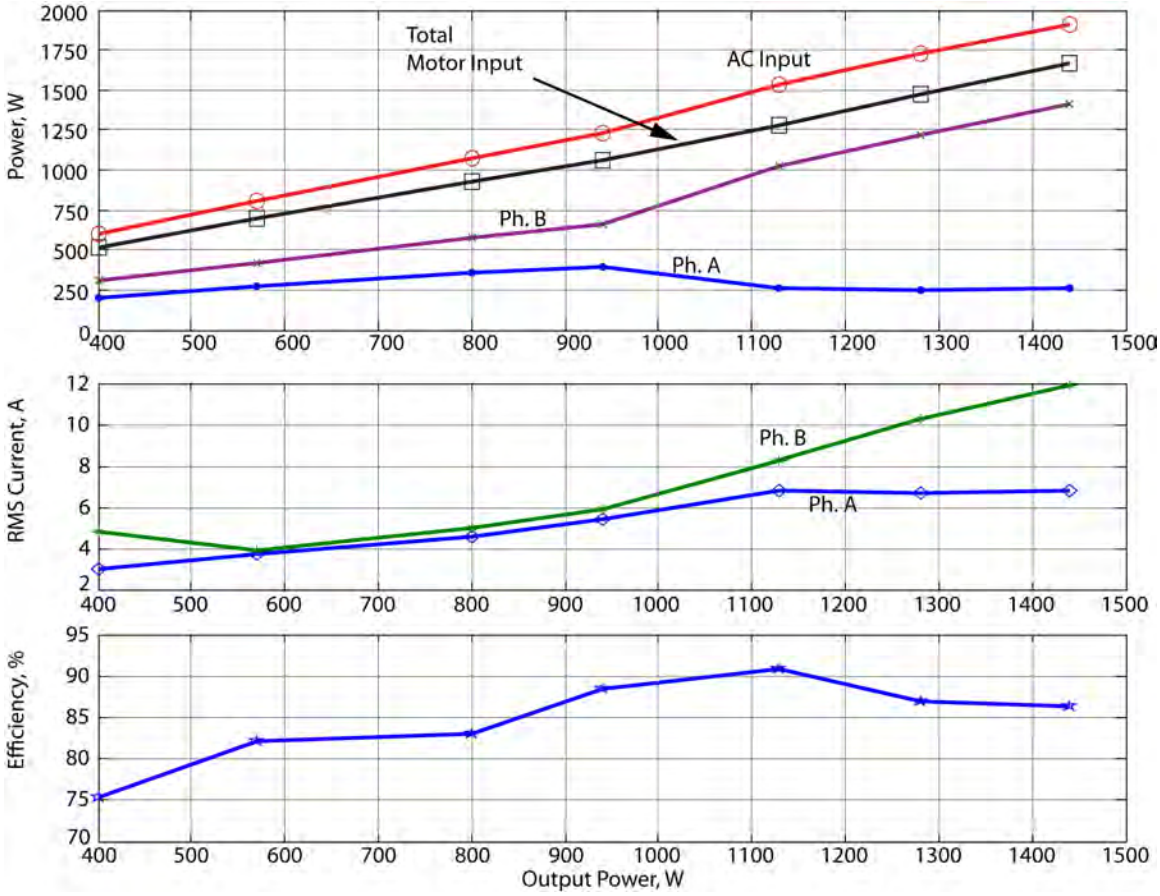

Figure 5.16: Graphical plot of the motor efficiency measured experimentally.

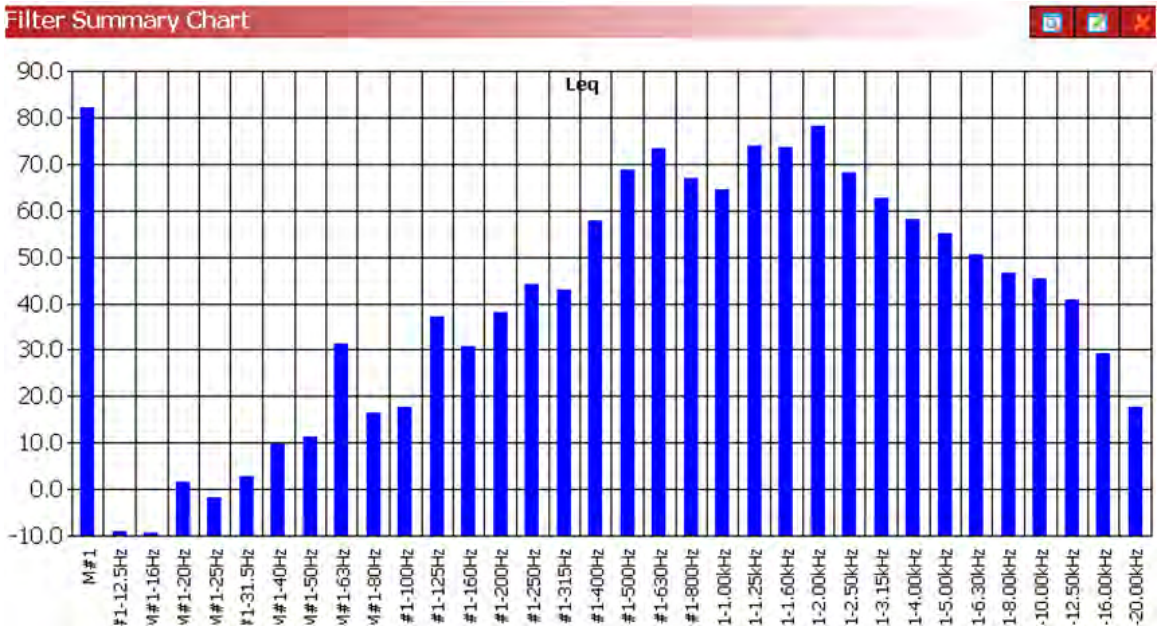

Figure 5.17: Measured acoustic noise for the prototype at 140W output at 3600 rpm.

Chapter 6

Conclusions

In this dissertation novel SRMs with stators free of flux reversals with and without magnets on select stator pole faces are presented and explored. Their design, principle of operation, and control are also presented with comprehensive non-linear simulations. The major contributions of this study are summarized as follows:

1. Two first generation flux-reversal-free-stator radial flux SRMs with six stator poles are presented in detail, highlighting their high power density and lower core-losses. These are the first two flux-reversal-free radial flux stator machines in the field of electric machines.

2. An analytical design procedure for the flux reversal stator machines is also presented. Detailed analysis with static and dynamic simulations showing the performance characteristics, discovery of unbalanced radial forces analytically and through simulations is also presented. The shorter flux path in the SRM requires lower MMF to drive the motor, reducing the phase current requirement and smaller winding coils. Core-losses were estimated analytically and through FEA and correlate well.

3. The presence of unbalanced radial forces in this class of SRMs makes it unattractive for large scale deployment due to the wear and tear that will occur on bearings, and eccentricities due to shaft deformation from unbalanced forces.

4. An experimental prototype of one 6/3 machine was constructed. The predicted and measured inductance show good correlation validating the design and analysis of the machine.

5. In Chapter 3, a novel doubly salient permanent magnet assisted SRM is presented and delineated from existing doubly salient permanent magnet machines. DSPMs are operated as ac machines and the net reluctance torque generated by the machine is zero. In the novel DSPMSRM, reluctance and magnet torque are always additive. Secondly, the motor operates as an SRM without flux-reversals in the stator making it the first homopolar radial flux PM machine.

6. Complete non-linear modeling of the SRM derived from fundamental equations is also presented from the novel DSPMSRM. The model takes into account magnetic saturation which is significant in reluctance machines. Simplification of the non-linear model for rapid simulations is also presented in detail.

7. Design equations which for initial sizing and design of the DSPMSRM are presented. The design equations allow for rapid calculation of motor dimensions for a given applications based on power requirements and desired magnet. The design equations are created for magnets with linear demagnetization characteristics like rare-earth Neodymium-Ferrite-Boron magnets.

8. An existing optimized 4-ecore SRM is modified into a DSPMSRM, and its increased power density is explored and presented. Through finite element simulations the increased operating power region of the DSPMSRM is compared to the 4-ecore SRM. Torque contributions from reluctance and magnets are presented separately to explicate the benefit of the magnets.

9. Full non-linear simulations showing the operation of the DSPMSRM with standard SRM controls are also presented. Novel PMSRM has higher efficiency, greater than 6% and its higher power density, greater than 30%, as compared to the conventional 4ecore machine at nominal power shows the advantage of this novel PMSRM electric machine. Furthermore, the increased partial load efficiency of the machine is also presented, which makes the novel SRM unique from conventional SRMs which have lower efficiency at lower power levels.

10. A prototype of the DSPMSRM was constructed for experimentation. The measured reluctance torque values correlated well with predicted values from FEA. The error is less than 7% for the reluctance component of the torque which is acceptable given the error in the supplied material characteristics. The average error in static torque results after adding the magnets is 12%. The measurement of the back-emf showed a 18% difference in the back-emf at no-load.

Phase inductance was measured for one current level there is an 18.5% error between the measured and predicted inductance.

11. The peak measured efficiency of the DSPMSRM prototype under non-ideal control conditions is 90.8%. The efficiency was measured with a 75% difference between the input power of both phases. The motor was able to reach the rated operating point with one phase delivering most of the power.

The results successfully show the benefit of having PMs in an SRM without losing all reluctance torque like the DSPM. The PMs enhanced the positive torque of the motor and increased the power density by 30% as compared to the 4ecore SRM. The flux reversal free stator has low core losses as compared to the 4ecore SRM. To exploit the machine‘s power capability, it is necessary to have proper current control with accurate commutation angles. Missing the turn on angle by one or two mechanical degrees greatly impacts the driving voltage to increase the current in the machine. Future work to improve the machine‘s performance will require a drive that is capable of commutation with an angular accuracy of 0.3 degrees or lower. The position sensor on the current drive has an analog sinusoidal position output capable of high position sensing accuracy but the DSP on the drive is limited by its firmware. Additional research will allow for new methods of position sensor free control to the applied to the motor. The PM‘s field is always present in the motor and the inactive phase can be used to estimate position reliably under the assumption the phases are magnetically separate.

In the current energy conscious market, high efficiency variable speed motors have gained tremendous traction. PM machines have been the big winners because their efficiency and power density is higher than induction machines. The price of rare earth magnets has increased by an order of magnitude in the last 18 months due to geographical and political issues. The supply of rare earth magnet materials from the world‘s largest manufacturer, China, is set to be cut by 35% in the year 2011 with demand only set to rise. Even with magnets in the DSPMSRM, the size of the magnets are a fraction of the size of magnets in equivalent PM machines. Hence, it is believed the novel class of machines machines presented in this dissertation will have a significant role to play in the variable speed market.

Bibliography

[1] *End-Use Consumption of Electricity 2001.* US Department of Energy.

[2] M.N. Anwar and I. Husain. Design perspectives of a low acoustic noise switched reluctance machine. *In. Proc of the IEEE Industry Applications Conference*, 1:99 – 106, 2000.

[3] M.N. Anwar, I. Husain, S. Mir, and T. Sebastian. Evaluation of acoustic noise and mode frequencies with design variations of switched reluctance machines. *IEEE Transactions on Industry Applications*, 39(3):695–703, May-June 2003.

[4] J Areddy. China's Rare-Earth Exports Slide, Still Bust Quota.

[5] M. Barnes and C. Pollock. Power electronic converters for switched reluctance drives. *IEEE Transactions on Power Electronics*, 13(6):1100–1111, 1998.

[6] R.E. Betz. Control of synchronous reluctance machines. *in Proc. IEEE Industry Applications Society Annual Meeting*, 1:456–462, 1991.

[7] I. Boldea. *Reluctance synchronous machines and drives.* Oxford University Press, USA, 1996.

[8] D.E. Cameron, J.H. Lang, and S.D. Umans. The origin and reduction of acoustic noise in doubly salient variable-reluctance motors. *IEEE Transactions on Industry Applications*, 28(6):1250–1255, Nov.-Dec. 1992.

[9] H. Chen and G. Xie. A Switched Reluctance Drive For the Axial-Flow Fan in Coal Mine. *in Proc. Proceedings 14th IFAC World Congress*, B:533–537, 1999.

[10] M. Cheng, Y. Fan, and KT Chau. Design and analysis of a novel stator–doubly-fed doubly salient motor for electric vehicles. *Journal of Applied Physics*, 97, 2005.

[11] R.S. Colby, Mottier F.M., Miller, and T.J.E. Vibration modes and acoustic noise in a four-phase switched reluctance motor. *IEEE Transactions on Industry Applications*, 32(6):1357–1364, Nov.-Dec. 1996.

[12] A. Cruickshank, A.F. Anderson, and R.W. Menzies. Theory and performance of reluctance motors with axially laminated anisotropic rotors. *Proc. Inst. Elect. Eng.*, 118(7):887–894, 1971.

[13] Dyson. Dyson reinvents the electric motor. *Dyson-Press*, 2003.

[14] M. Ehsani, I. Husain, and A.B. Kulkarni. Elimination of discrete position sensor and current sensor in switched reluctance motor drives. *Ind. Appl., IEEE Trans.*, 28(1):128–135, Jan/Feb 1992.

[15] CA Ferreira, SR Jones, BT Drager, and WS Heglund. Design and implementation of a five horsepower switched reluctance, fuel-lube, pump motor drive for a gas turbine engine. *in Proc. Applied Power Electronics Conference and Exposition*, pages 56–62, 1994.

[16] JO Fiedler and RW De Doncker. Designing low-cost switched reluctance drives for fan-applications. *in Proc. IEE International Conference on Power Electronics, Machines and Drives*, March 2004.

[17] E.R.T. Goodier and C. Pollock. Homopolar variable reluctance machine incorporating an axial field coil. *Industry Applications, IEEE Transactions on*, 38(6):1534–1541, Nov/Dec 2002.

[18] K. Ha, C. Lee, J. Kim, R. Krishnan, and S.G. Oh. Design and Development of Low-Cost and High-Efficiency Variable-Speed Drive System With Switched Reluctance Motor. *IEEE Transactions on Industry Applications*, 43(3):703–713, 2007.

[19] Y. Hayashi and T.J.E. Miller. A new approach to calculating core losses in the srm. *IEEE Transactions on Industry Application*, 31(5):1039–1046, Sept.-Oct. 1995.

[20] J.D. Herbst, A.L. Gattozzi, and R.E. Hebner. A Megawatt Power Module for Ship Service-Supplement. Volume 1: Program Technical Report. 2007.

[21] E. Hoang, AH Ben Ahmed, and J. Lucidarme. Switching flux permanent magnet polyphased synchronous machines. 3:3–3, 1997.

[22] J. Holtz. Sensorless control of induction motor drives. *Proc. IEEE*, 90(8):1359–1394, Aug 2002.

[23] W. Hua, Z.Q. Zhu, M. Cheng, Y. Pang, and D. Howe. Comparison of flux-switching and doubly-salient permanent magnet brushless machines. *in Proc. IEEE Int. Conf. Elec. Machines and Sys.*, 1:165–170, 2005.

[24] C. Hudson, NS Lobo, and R. Krishnan. Sensorless control of single switch based switched reluctance motor drive using neural network. *in Proc. IEEE Annual Industrial Electronics Society*, 3, 2004.

[25] CA Hudson, NS Lobo, and R. Krishnan. Sensorless Control of Single Switch-Based Switched Reluctance Motor Drive Using Neural Network. *IEEE Transactions on Industrial Electronics*, 55(1):321–329, 2008.

[26] I. Husain and M. Ehsani. Rotor position sensing in switched reluctance motor drives by measuring mutually induced voltages. *Ind. Appl., IEEE Trans.*, 30(3):665–672, May/Jun 1994.

[27] A. Ishizaki, T. Tanaka, K. Takasaki, and S. Nishikata. Theory and optimum design of pm vernier motor. *IEE Conference Publications*, (CP412):208–212, 1995.

[28] K.B. Jang, S.Y. Lim, T.B. Lim, C.S. Jin, Y.H. Cho, Y.T. Kim, and J. Lee. 2-D FE analysis of hybrid stepping motor using virtual magnetic barrier. *IEEE Transactions on Magnetics*, 39(5 Part 2):3268–3270, 2003.

[29] P.L. Jansen and R.D. Lorenz. Transducerless position and velocity estimation in induction and salient ac machines. *Ind. Appl., IEEE Trans.*, 31(2):240–247, Mar/Apr 1995.

[30] WD Jones. The rare-earth-metal bottleneck. *Spectrum, IEEE*, 47(1):80, 2010.

[31] J Kim and R. Krishnan. High efficiency single-pulse controlled switched reluctance motor drive for high speed (48k rpm) application: Analysis, design, and experimental verification. *in Proc. Industry Applications Society Annual Meeting*, pages 1–8, Oct. 2008.

[32] J. Kim and R. Krishnan. Novel two-switch-based switched reluctance motor drive for low-cost high-volume applications. *Industry Applications, IEEE Transactions on*, 45(4):1241–1248, July-aug. 2009.

[33] Jaehyuck Kim and R. Krishnan. Single-controllable-switch-based switched reluctance motor drive for low-cost variable- speed applications. *in Proc. IEEE Energy Conversion Congress and Exposition*, pages 2535–2542, Sept. 2009.

[34] JK Kostko. Polyphase reaction synchronous motors. *American Institute of Electrical Engineers*, 45:1162–1168, 1923.

[35] M. Krishnamurthy, C.S. Edrington, A. Emadi, P. Asadi, M. Ehsani, and B. Fahimi. Making the case for applications of switched reluctance motor technology in automotive products. *IEEE Transaction on Power Electronics*, 21(3):659–675, 2006.

[36] R. Krishnan. A novel converter topology for switched reluctance motor drives. *in Proc. IEEE Power Electronics Specialists Conference*, 2, 1996.

[37] R. Krishnan. *Switched reluctance motor drives: modeling, simulation, analysis, design, and applications*. CRC, 2001.

[38] R. Krishnan. Radial-axial electromagnetic flux electric motor, coaxial electromagnetic flux electric motor, and rotor for same, 2004. US Patent App. 10/995,557.

[39] R. Krishnan. *Permanent Magnet Synchronous and Brushless DC Motor Drives*. CRC, 2009.

[40] R. Krishnan, R. Arumugan, and J.F. Lindsay. Design procedure for switched-reluctance motors. *Industry Applications, IEEE Transactions on*, 24(3):456–461, May/Jun 1988.

[41] R. Krishnan, D. Blanding, A. Bhanot, AM Staley, and N.S. Lobo. High reliability SRM drive system for aerospace applications. *in Proc. Industrial Electronics Society*, 2, 2003.

[42] R. Krishnan and N.S. Lobo. Apparatus and method that prevent flux reversal in the stator back material of a two-phase srm (tpsrm). *U.S. Patent 7,015,615*, March 2006.

[43] R. Krishnan and PN Materu. Design of a single-switch-per-phase converter for switchedreluctance motor drives. *IEEE Transactions on Industrial Electronics*, 37(6):469–476, 1990.

[44] R. Krishnan and PN Materu. Analysis and design of a low-cost converter for switched reluctancemotor drives. *IEEE Transactions on Industry Applications*, 29(2):320–327, 1993.

[45] R. Krishnan, S.Y. Park, and K. Ha. Theory and operation of a four-quadrant switched reluctance motor drive with a single controllable switch-the lowest cost four-quadrant brushless motor drive. *IEEE Transactions on Industry Applications*, 41(4):1047–1055, 2005.

[46] R. Krishnan, AM Staley, and K. Sitapati. A novel single-phase switched reluctance motor drive system. *in Proc. IEEE Industrial Electronics Society Annual Conference*, 2, 2001.

[47] P.J. Lawrenson and SK Gupta. Developments in the performance and theory of segmental-rotor reluctance motors. *Proceedings of the IEE*, 114:645–653, 1967.

[48] P.J. Lawrenson, J.M. Stephenson, N.N. Fulton, P.T. Blenkinsop, and J. Corda. Variable-speed switched reluctance motors. *Electric Power Applications, IEE Proceedings B*, 127(4):253–265, July 1980.

[49] C. Lee, R. Krishnan, and NS Lobo. Novel Two-phase Switched Reluctance Machine using Common-Pole E-Core Structure: Concept, Analysis, and Experimental Verification. pages 2210–2217, 2007.

[50] C. Lee, R. Krishnan, and NS Lobo. Novel Two-Phase Switched Reluctance Machine Using Common-Pole E-Core Structure: Concept, Analysis, and Experimental Verification. *IEEE TRANSACTIONS ON INDUSTRY APPLICATIONS*, 45(2):703, 2009.

[51] C.H. Lee. Vernier motor and its design. *IEEE Transactions on Power Apparatus and Systems*, 82(66):343–349, 1963.

[52] Cheewoo Lee and R. Krishnan. New designs of a two-phase e-core switched reluctance machine by optimizing the magnetic structure for a specific application: Concept, design, and analysis. *in Proc. IEEE Industry Applications Society Annual Conference*, pages 1–8, Oct. 2008.

[53] Cheewoo Lee, R. Krishnan, and N.S. Lobo. Novel two-phase switched reluctance machine using common-pole e-core structure: Concept, analysis, and experimental verification. *in Proc. 42nd Annual IEEE Industry Applications Conference*, pages 2210–2217, Sept. 2007.

[54] Y. Li, JD Lloyd, GE Horst, A.M.D. Center, E.E. Co, and MO St Louis. Switched reluctance motor with dc assisted excitation. *in Proc. IEEE Ind. Appl. Conf.*, 2, 1996.

[55] Y. Liao, F. Liang, and T. Lipo. A novel permanent magnet motor with doubly salient structure. *IEEE Transactions on industry applications*, 31(5):1069–1078, 1995.

[56] HS Lim, R. Krishnan, and NS Lobo. Design and control of a linear propulsion system for an elevator using linear switched reluctance motor drives. *in Proc. IEEE International Conference on Electric Machines and Drives*, pages 1584–1591, 2005.

[57] H.S. Lim, R. Krishnan, and NS Lobo. Design and Control of a Linear Propulsion System for an Elevator Using Linear Switched Reluctance Motor Drives. *IEEE Transactions on Industrial Electronics*, 55(2):534–542, 2008.

[58] HS Lim, DG Roberson, NS Lobo, and R. Krishnan. Novel flux linkage control of switched reluctance motor drives using observer and neural network-based correction methods. page 6, 2005.

[59] NS Lobo, HS Lim, and R. Krishnan. Comparison of Linear Switched Reluctance Machines for Vertical Propulsion Application: Analysis, Design and Experimental Correlation. volume 1, 2006.

[60] NS Lobo, HS Lim, and R. Krishnan. Comparison of linear switched reluctance machines for vertical propulsion application: Analysis, design, and experimental correlation. *IEEE Transactions on Industry Applications*, 44(4):1134–1142, 2008.

[61] NS Lobo, S.G. Oh, and R. Krishnan. Comparison of Two Switched Reluctance Motors with No Flux-Reversal in the Stator. *in Proc. 32nd Annual IEEE Industrial Electronics Conference*, pages 1459–1464, 2006.

[62] N.S. Lobo, E. Swint, and R. Krishnan. M-phase n-segment flux-reversal-free stator switched reluctance machines. *in Proc. IEEE Industry Applications Conference*, pages 1–8, Oct. 2008.

[63] NS Lobo, E. Swint, and R. Krishnan. M-Phase N-Segment Flux-Reversal-Free Stator Switched Reluctance Machines. *in Proc. IEEE Industry Applications Society Annual Meeting*, pages 1–8, 2008.

[64] SR MacMinn and WD Jones. A very high speed switched-reluctance starter-generator forair-craft engine applications. *in Proc. Aerospace and Electronics Conference*, pages 1758–1764, 1989.

[65] A. Matveev, V. Kuzmichev, and E. Lomonova. A new comprehensive approach to estimation of end-effects in switched reluctance motors. *in Proc. IEEE International Conference on Electric Machines*, pages 26–30, 2002.

[66] J.R. Melcher. *Continuum electromechanics*. MIT press Cambridge, MA, 1981.

[67] T.J.E. Miller. *Switched reluctance motors and their control.* Magna Physics, 1993.

[68] T.J.E. Miller. Optimal design of switched reluctance motors. *Industrial Electronics, IEEE Transactions on*, 49(1):15–27, Feb 2002.

[69] T.J.E. Miller and M. McGilp. Nonlinear theory of the switched reluctance motor for rapid computer-aided design. *Electric Power Applications, IEE Proceedings B*, 137(6):337–347, Nov 1990.

[70] S. Mir, I. Husain, and M.E. Elbuluk. Energy-efficient C-dump converters for switched reluctance motors. *IEEE Trans. on Power Electron.*, 12(5):912–921, 1997.

[71] M.A. Mueller and N.J. Baker. Modelling the performance of the vernier hybrid machine. *IEE Proc. Electric Power Applications*, 150(6):647–654.

[72] SA Nasar. DC-switched reluctance motor. *in Proc. Institue of Electrical Engineers*, 116(6):1048–1049, 1969.

[73] R.H. Park. Two reaction theory of synchronous machines. pages 716–730, 1929.

[74] W.A. Pengov, J.R. Hendershot, and T.J.E.; Miller. A new low-noise two-phase switched reluctance motor. *Iin Proc. IEEE Internat. Conf. Elec. Machines and Drives*, pages 1281 – 1284, 2005.

[75] C. Pollock, H. Pollock, R. Barron, J.R. Coles, D. Moule, A. Court, and R. Sutton. Flux-switching motors for automotive applications. *Industry Applications, IEEE Transactions on*, 42(5):1177–1184, Sept.-Oct. 2006.

[76] C. Pollock and M. Wallace. The flux switching motor, a DC motor without magnets or brushes. In *in Proc. IEEE Industry Applications Society Annual Meeting*, volume 3, 1999.

[77] C. Pollock and BW Williams. A unipolar converter for a switched reluctance motor. *Industry Applications Society Annual Meeting, 1988., Conference Record of the 1988 IEEE*, pages 44–49, 1988.

[78] H. Pollock, C. Pollock, RT Walter, and BV Gorti. Low cost, high power density, flux switching machines and drives for power tools. *in Proc. IEEE Industry Applications Conference*, 3:1451–1457, Oct. 2003.

[79] J. Pyrhonen, T. Jokinen, and V. Hrabovcova. *Design of Rotating Electrical Machines*. Wiley-Blackwell, 2009.

[80] AV Radun. High power density switched reluctance motor drive for aerospaceapplications. *in Proc. IEEE Industry Applications Society Annual Meeting*, pages 568–573, 1989.

[81] A.V. Radun. Design considerations for the switched reluctance motor. *Industry Applications, IEEE Transactions on*, 31(5):1079–1087, Sep/Oct 1995.

[82] S.E. Rauch and L.J. Johnson. Design principles of flux-switch alternators. *AIEE Trans.*, 74(12):1261–1268, 1955.

[83] W.F. Ray and I.H. Al-Bahadly. A sensorless method for determining rotor position for switched reluctance motors. *in Proc. Intl. Conf. Power Electron. and Variable-Speed Drives*, pages 13–17, Oct 1994.

[84] D.J. Rhodes. Assessment of vernier motor design using generalised machine concepts. *Power Apparatus and Systems, IEEE Transactions on*, 96(4):1346–1352, July 1977.

[85] E. Richter. High temperature, lightweight, switched reluctance motors and generators for future aircraft engine applications. *1988 American Control Conference, 7 th, Atlanta, GA, Proceedings.*, 3:1846–1851, 1988.

[86] Seok-Gyu Oh and R. Krishnan. Two-phase srm with flux-reversal-free stator: Concept, analysis, design, and experimental verification. *Ind. Appl., IEEE Trans.*, 43(5):1247–1257, Sept.-oct. 2007.

[87] K. Sivasubramaniam, ET Laskaris, MR Shah, JW Bray, and NR Garrigan. High-Temperature Superconducting Homopolar Inductor Alternator for Marine Applications. *IEEE Transactions on Applied Superconductivity*, 18(1):1–6, 2008.

[88] A.E. Snowdon and E.W. Madsen. Characteristics of a synchronous inductor motor. *Trans. Amer. Inst. Elect. Engrs., Part II*, 81:1, 1962.

[89] E. Spooner and L. Haydock. Vernier hybrid machines. *Electric Power Applications, IEE Proc.*, 150(6):655–662, Nov. 2003.

[90] DA Staton, TJE Miller, and SE Wood. Maximising the saliency ratio of the synchronous reluctance motor. *IEE Proceedings Electric Power Applications*, 140(4):249–259, 1993.

[91] E. Swint and R. Krishnan. Two-phase sr drive with flux-reversal free stator and balanced normal forces. *in Proc. IEEE Industry Applications Society Annual Meeting*, pages 1–6, Oct. 2008.

[92] H. Tajima and Y. Hori. Speed sensorless field-orientation control of the induction machine. *Ind. Appl., IEEE Trans.*, 29(1):175–180, Jan/Feb 1993.

[93] W.H. Taylor. Obtaining motive power. *Patent #8255, England and Wales*, 1839.

[94] R. Vandana, N. Vattikuti, and B.G. Fernandes. A novel high power density segmented switched reluctance machine. *in Proc. IEEE Ind. Appl. Conf.*, pages 1–7, Oct. 2008.

[95] P. Vijayraghavan. *Design of Switched Reluctance Motors and Development of a Universal Controller for Switched Reluctance and Permanent Magnet Brushless DC Motor Drives*. PhD thesis, Virginia Tech, 2001.

[96] J'H' Walker. The theory of the inductor alternator. *Journal IEE*, 89:227–241, 1942.

[97] B.A. Welchko, T.A. Lipo, T.M. Jahns, and S.E. Schulz. Fault tolerant three-phase AC motor drive topologies: a comparison of features, cost, and limitations. *IEEE Transactions on Power Electronics*, 19(4):1108–1116, 2004.

[98] Chi-Yao Wu and C. Pollock. Analysis and reduction of vibration and acoustic noise in the switched reluctance drive. *IEEE Transactions on Industry Applications*, 31(1):91–98, Jan.-Feb. 1995.

[99] L. Xu, X. Xu, T. Lipo, and D.W. Novotny. Vector control of a synchronous reluctance motor including saturation and iron loss. *IEEE Transactions on Industry Applications*, 27(5):977–985, 1991.

[100] H. Yamai, M. Kaneda, K. Ohyama, Y. Takeda, and N. Matsui. Optimal switched reluctance motor drive for hydraulic pump unit. *in Proc. IEEE Industry Applications Conference*, 3, 2000.

[101] Z.Q. Zhu, Y. Pang, D. Howe, S. Iwasaki, R. Deodhar, and A. Pride. Analysis of electromagnetic performance of flux-switching permanent-magnet machines by nonlinear adaptive lumped parameter magnetic circuit model. *Magnetics, IEEE Transactions on*, 41(11):4277–4287, Nov. 2005.

Appendix A

A.1 Dimension of the machines

Table A.1: Dimensions of the designed 6/3 and 6/9 SRMs

	6/3 SRM	6/9 SRM
Air Gap Radius (mm)	43.7	43.7
Stator Outer Diameter (mm)	82	82
Main Pole Arc	37^o	21^o
Auxiliary Pole Arc	22^o	16^o
Rotor Pole Arc	72^o	21^o
Stack Length (mm)	85	60
Rotor Mass (kg)	2.74	1.91
Stator Mass (kg)	6.55	4.01
Rotational Inertia (kg-m^2)	1.44×10^{-4}	4.04×10^{-5}
Winding Turns per pole	110	110
Winding Mass (kg)	1.39	1.07

A.2 Drawing and winding pattern of the 4/10 SRM

A.3 Core-loss estimation using Matlab

```
1     position=0:1/6/1800:120/6/1800-1/6/1800;
2 %a0 part 1 =1:49
```

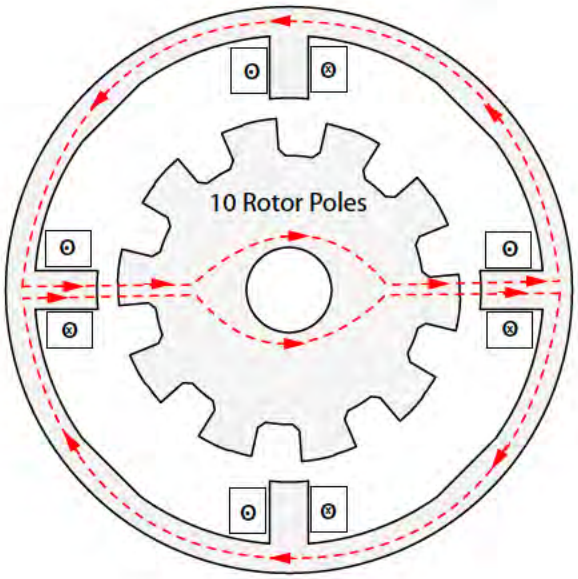

Figure A.1: 4/10 SRM

```
% syms t
%%%%%%%%%%%%%%%%%%%%%%%%%%%%%%%%
%          P O L E       A0     %
%%%%%%%%%%%%%%%%%%%%%%%%%%%%%%%%
pole.a0.max=1.716;
a0 =      -393.617916848734;        a1 =      165.130867775749e+000 ;
b1 =       677.790746907148;        a2 =       423.975313634511e+000 ;
b2 =      -220.668547127137;        a3 =      -163.429761831259 ;
b3 =      -186.628782385549;        a4 =      -53.3238084436913 ;
b4 =       75.8371090814130;        a5 =      20.9184128522616;
b5 =       8.1978082357810;         a6 =      356.963541138381e-003 ;
b6 =      -2.66299543962867;        w =       558.592742517341;
% part 1 =1:49
%t=position(1:49);
pole.a0.a =                         a0 + a1*cos(t*w) + b1*sin(t*w) + ...
    a2*cos(2*t*w) + b2*sin(2*t*w) + a3*cos(3*t*w) + b3*sin(3*t*w) + ...
    a4*cos(4*t*w) + b4*sin(4*t*w) + a5*cos(5*t*w) + b5*sin(5*t*w) + ...
    a6*cos(6*t*w) + b6*sin(6*t*w);
pole.a0.a = pole.a0.a/pole.a0.max;

a1 =        9536;          b1 =      -0.1183;
c1 =     0.03923;          a2 =       0.2258;
```

```
b2 =     0.004629;        c2 =    0.0002634;
a3 =            0;        b3 =       -9.995;
c3 =  8.115e-006;         a4 =        1.103;
b4 =     0.004014;        c4 =     0.001627;

pole.a0.b=  a1*exp(-((t-b1)/c1).^2) + a2*exp(-((t-b2)/c2).^2) + ...
    a3*exp(-((t-b3)/c3).^2) + a4*exp(-((t-b4)/c4).^2);
pole.a0.b=pole.a0.b/pole.a0.max;
% part 65:120

p1 =  4.443508254324373e+023;        p2 = -3.438205613035669e+022;
p3 = 1.175354632614461e+021;      p4 = -2.329471189432134e+019;
p5 =  2.949271537822603e+017;      p6 =  -2.473176300590490e+015;
p7 =  1.373403793993085e+013;       p8 = -4.869348661496937e+010;
p9 =      9.999929982204089e+007;         p10 =  -9.061426943109270e+004;

pole.a0.c=p1*t.^9 + p2*t.^8 + p3*t.^7 + p4*t.^6 + ...
    p5*t.^5 + p6*t.^4 + p7*t.^3 + p8*t.^2 + p9*t + p10;
pole.a0.c=pole.a0.c/pole.a0.max;

dif.pole.a0.a = (diff(pole.a0.a,t))^2;  dif.pole.a0.b = (diff(pole.a0.b,t))^2;  dif.
    pole.a0.c =  (diff(pole.a0.c,t))^2; %Taking the derivative  of the square of the
    pole flux density vs. time.

intgl.a0= double(int(dif.pole.a0.a,t,position(1),position(49)))+...
    double(int(dif.pole.a0.b,t,position(49),position(65)))+...
    double(int(dif.pole.a0.c,t,position(65),position(120)));  % Integrating the
        square of the pole flux density for loss

% Motor physical mass properties.
main_pole_mass = 60139.370/1e9 * 7866;

%The core loss per iron section
Ce1= pi^2*(.6*1e-3)^2/(6*.6*10^-6*7866)/(2*pi*pi);
coreloss.a0=  (1800/60) * 3 * main_pole_mass * Ce1 * (pole.a0.max)^2 * intgl.a0;
```

A.4 Performance characteristics of the SRM

A.4.1 Single pulse control simulation summary with 38 mm stack for the DSPM-SRM

Rotor velocity, rad/s	377
Average torque, N-m	3.89
Output power, W	1466
Input power, W	1600
Core-loss, W	81
RMS current, W	7.3
Resistive loss, W	53
Efficiency, %	91.6
Peak-to-peak torque ripple, N-m	6.5

A.4.2 Hysteresis current control simulation parameters and results

Hysteresis controller:

```
if (r - i ) < 0.2
T1, T2: ON      %Applying +dc-bus minus device voltage drops
elseif (r - i) > 0.1
T1, T2: OFF     %Applying -dc-bus  plus device voltage drops
else
T1: ON, T2: OFF %Apply zero control input for circulation
end
```

Turn on and turn off angles used for current control. 0 deg. corresponds to the rotor position where the rotor is unaligned with respect to the stator poles with no current excitation.

Current, A	Turn-on angle, deg.	Turn-off angle, deg.
4 - 6	-1.7	16.7
7 - 8	-2.0	16.7
9 - 13	-2.3	16.2

Appendix B

List of Publications and Patents

Bibliography

[1] C. Hudson, NS Lobo, and R. Krishnan. Sensorless control of single switch based switched reluctance motor drive using neural network. *in Proc. IEEE Annual Industrial Electronics Society Annual Meeting*, vol. 3, 2004.

[2] C Hudson, NS Lobo, and R. Krishnan. Sensorless Control of Single Switch-Based Switched Reluctance Motor Drive Using Neural Network. *IEEE Transactions on Industrial Electronics*, vol. 55(1):321–329, 2008.

[3] PCT Application WO 2006/050344: C Hudson, NS Lobo, and R Krishnan. Motor control system for establishing characteristic parameters. 2006.

[4] US Patent Application 20080315811: C Hudson, NS Lobo, and R Krishnan. System and method for collecting characteristic information of a motor, neural network and method for estimating regions of motor operation from information characterizing the motor, and system and method for controlling motor. 2008.

[5] PCT Application WO 2004/084375: R Krishnan and NS Lobo. Apparatus and method that prevent flux reversal in the stator back material of a two-phase srm (tpsrm). 2004.

[6] US Patent 7,015,615: R Krishnan and NS Lobo. Apparatus and method that prevent flux reversal in the stator back material of a two-phase srm (tpsrm). 2006.

[7] US Patent 7,579,734: R Krishnan and NS Lobo. Apparatus and method that prevent flux reversal in the stator back material of a two-phase srm (tpsrm). 2009.

[8] C. Lee, R. Krishnan, and NS Lobo. Novel Two-phase Switched Reluctance Machine using Common-Pole E-Core Structure: Concept, Analysis, and Experimental Verification. *in Proc. 42st IEEE Industry Applications Conference*, pages 2210–2217, 2007.

[9] C. Lee, R. Krishnan, and NS Lobo. Novel Two-Phase Switched Reluctance Machine Using Common-Pole E-Core Structure: Concept, Analysis, and Experimental Verification. *IEEE Transactions on Industry Applications*, vol. 45(2):703, 2009.

[10] PCT Application WO 2008/153832: CW Lee, R Krishnan, and NS Lobo. Switched reluctance machines with minimum stator core. 2008.

[11] US Patent Application 20100141061: CW Lee, R Krishnan, and NS Lobo. Switched reluctance machines with minimum stator core. 2007.

[12] HS Lim, R. Krishnan, and NS Lobo. Design and control of a linear propulsion system for an elevator using linear switched reluctance motor drives. *in Proc. IEEE International Conference on Electric Machines and Drives*, pages 1584–1591, 2005.

[13] H.S. Lim, R. Krishnan, and NS Lobo. Design and Control of a Linear Propulsion System for an Elevator Using Linear Switched Reluctance Motor Drives. *IEEE Transactions on Industrial Electronics*, vol. 55(2):534–542, 2008.

[14] HS Lim, DG Roberson, NS Lobo, and R. Krishnan. Novel flux linkage control of switched reluctance motor drives using observer and neural network-based correction methods. *in Proc. 31st Annual IEEE Industrial Electronics Conference*, page 6, 2005.

[15] NS Lobo, HS Lim, and R. Krishnan. Comparison of Linear Switched Reluctance Machines for Vertical Propulsion Application: Analysis, Design and Experimental Correlation. *in Proc. 41st IEEE Industry Applications Conference*, vol. 1, 2006.

[16] NS Lobo, HS Lim, and R. Krishnan. Comparison of linear switched reluctance machines for vertical propulsion application: Analysis, design, and experimental correlation. *IEEE Transactions on Industry Applications*, vol. 44(4):1134–1142, 2008.

[17] NS Lobo, S.G. Oh, and R. Krishnan. Comparison of Two Switched Reluctance Motors with No Flux-Reversal in the Stator. *in Proc. 32nd Annual IEEE Industrial Electronics Conference*, pages 1459–1464, 2006.

[18] NS Lobo, E. Swint, and R. Krishnan. M-Phase N-Segment Flux-Reversal-Free Stator Switched Reluctance Machines. *in Proc. IEEE Industry Applications Society Annual Meeting*, pages 1–8, 2008.

Vita

Nimal Savio Lobo

Nimal Lobo received the B.S. and M.S. degrees in electrical engineering from the Virginia Polytechnic Institute and State University in 2002 and 2005. He has over five years of experience in the research of AC and SRM machines, power electronics and control systems. He is currently a senior motor design engineer at Ramu, Inc. in Blacksburg, VA. His research interests include design and control of electric machines, position sensorless control and control of power electronics.